Atom interferometer with Bose-Einstein Condensate : toward a determination of fine-structure constant α

Zhibin Yao

To cite this version:

Zhibin Yao. Atom interferometer with Bose-Einstein Condensate : toward a determination of fine-structure constant α. Atomic Physics [physics.atom-ph]. Sorbonne Université, 2022. English. NNT : 2022SORUS356 . tel-03935748

HAL Id: tel-03935748
https://theses.hal.science/tel-03935748v1

Submitted on 12 Jan 2023

Sorbonne Université
Laboratoire Kastler Brossel (UMR 8552)

Atom interferometry with a Bose Einstein Condensate: Toward a determination of fine structure constant α

Presented by ZHIBIN YAO

PhD thesis in PHYSICS

05 September 2022

M.	Carsten Klempt	Reporter
M.	Yannick Bidel	Reporter
M^{me}	Mathilde Hugbart	Examinator
M^{me}	Emily Lamour	Examinator
M^{me}	Saïda Guellati-Khelifa	Supervisor
M.	Pierre Cladé	Invited

Contents

Chapter 1

General introduction

1.1 A short story of the fine-structure constant

The fine-structure constant α is a fundamental constant of physics given by

$$\alpha = \frac{e^2}{4\pi\epsilon_0\hbar c} \tag{1.1}$$

where e is the elementary electric charge, $\hbar$ is the reduced Planck constant, ϵ_0 is vacuum permittivity and c the speed of the light.

The constant α has been first introduced by Arnold Sommerfeld [68] in 1916 to explain the splitting of the Balmer line observed in the hydrogen spectrum. A. Sommerfeld extended the Bohr model by considering the relativistic mass and elliptical orbits to describe the electron's trajectory. He quantified both the angular and the radial momenta of the electron, which allowed him to introduce a second quantum number.

Of course, the Sommerfeld model was not correct because the spin of the electron was not discovered yet, and the spin-orbit coupling was thus not considered. However, what is remarkable is that the formula for the energy levels derived by Sommerfeld was exactly the same as the one deduced from the Dirac equation. Moreover, the analysis of the hydrogen spectrum allowed Sommerfeld to determine the structure-fine constant α to within a few 10^{-3}.

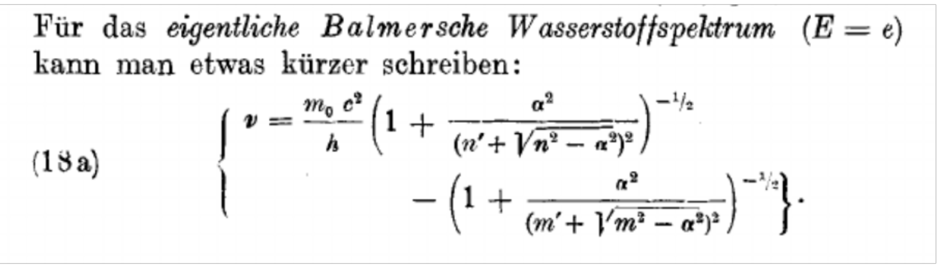

Für das *eigentliche Balmersche Wasserstoffspektrum* $(E = e)$ kann man etwas kürzer schreiben:

$$\nu = \frac{m_0 c^2}{h}\left\{\left(1 + \frac{\alpha^2}{(n' + \sqrt{n^2 - \alpha^2})^2}\right)^{-1/2} - \left(1 + \frac{\alpha^2}{(m' + \sqrt{m^2 - \alpha^2})^2}\right)^{-1/2}\right\}. \tag{18a}$$

Figure 1.1: Formula of hydrogen energy levels derived by A. Sommerfeld (extracted from the reference [68].

The formula for the energy levels of the hydrogen atom derived from Dirac equation is:

$$E(n,j) = m_\mathrm{e}c^2 \left[1 + \frac{\alpha^2}{\left(n - j - \frac{1}{2} + \sqrt{\left(j+\frac{1}{2}\right)^2 - \alpha^2} \right)^2} \right]^{-1/2}$$

This equation can be expressed as a power series expansion of α

$$E(n,j) \simeq m_\mathrm{e}c^2 \left[1 - \frac{\alpha^2}{2n^2} - \frac{\alpha^4}{2n^4} \left(\frac{n}{j+\frac{1}{2}} - \frac{3}{4} \right) + ... \right]$$

From this equation, we get the relation between the Rydberg constant R_∞ and the fine-constant α, that we use in our experiment to determine the constant α

$$hcR_\infty = \frac{1}{2} m_\mathrm{e} \alpha^2 c^2 \tag{1.2}$$

Dirac also predicted the magnetic moment of the electron with a Landé factor equal to 2,

$$\vec{\mu}_\mathrm{e} = -g_\mathrm{e} \frac{e}{2m_\mathrm{e}} \vec{S}, \quad g_\mathrm{e} = 2$$

In 1947, two experiments undermined Dirac's predictions, the first was the measurement of a shift between the $^2S_{1/2}$ and $^2P_{1/2}$ energy levels of the hydrogen atom, namely the Lamb shift [51]. The second is the experiment of Kush and Foley [50], which showed from measurements of the Landé factors of Ga (galium), In (indium) and Na (sodium) that the g_e factor of the electron is slightly different from 2. These experimental observations were explained by the interaction between the vacuum energy fluctuations and the electron.

The deviation of g-factor of the electron to Dirac prediction is called the electron magnetic moment anomaly a_e. The first order of a_e has been calculated by Schwinger [65]

$$\frac{g_e}{2} = 1 + a_\mathrm{e} \simeq 1 + \frac{1}{2}\frac{\alpha}{\pi}$$

This correction depends only on the fine-structure constant α. These two experiments and the Schwinger's work mark the birth of quantum electrodynamics (QED). As we will see in the next paragraph, higher order corrections including all the processes involved in the interaction with virtual particles and photons of the quantum vacuum are accounted for in a power law in α. This constant is the only parameter of quantum electrodynamics that quantifies the strength of the electromagnetic interaction between elementary charged particles.

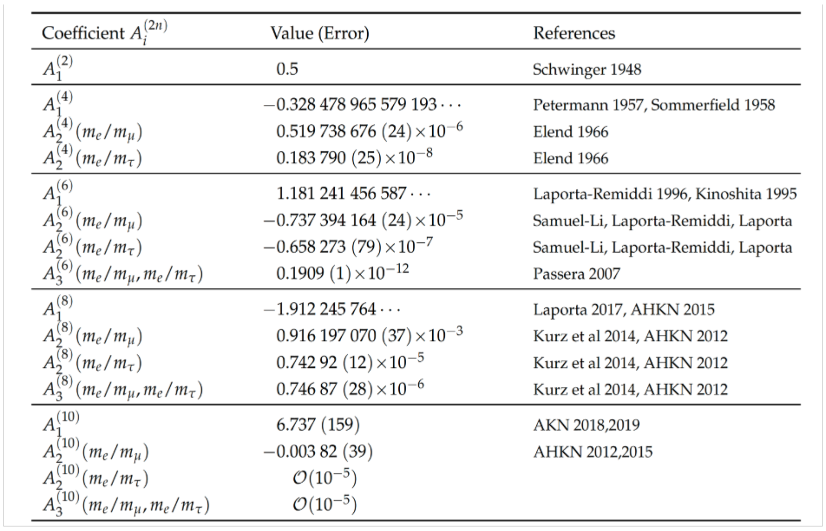

Coefficient $A_i^{(2n)}$	Value (Error)	References
$A_1^{(2)}$	0.5	Schwinger 1948
$A_1^{(4)}$	$-0.328\,478\,965\,579\,193\cdots$	Petermann 1957, Sommerfield 1958
$A_2^{(4)}(m_e/m_\mu)$	$0.519\,738\,676\,(24)\times10^{-6}$	Elend 1966
$A_2^{(4)}(m_e/m_\tau)$	$0.183\,790\,(25)\times10^{-8}$	Elend 1966
$A_1^{(6)}$	$1.181\,241\,456\,587\cdots$	Laporta-Remiddi 1996, Kinoshita 1995
$A_2^{(6)}(m_e/m_\mu)$	$-0.737\,394\,164\,(24)\times10^{-5}$	Samuel-Li, Laporta-Remiddi, Laporta
$A_2^{(6)}(m_e/m_\tau)$	$-0.658\,273\,(79)\times10^{-7}$	Samuel-Li, Laporta-Remiddi, Laporta
$A_3^{(6)}(m_e/m_\mu, m_e/m_\tau)$	$0.1909\,(1)\times10^{-12}$	Passera 2007
$A_1^{(8)}$	$-1.912\,245\,764\cdots$	Laporta 2017, AHKN 2015
$A_2^{(8)}(m_e/m_\mu)$	$0.916\,197\,070\,(37)\times10^{-3}$	Kurz et al 2014, AHKN 2012
$A_2^{(8)}(m_e/m_\tau)$	$0.742\,92\,(12)\times10^{-5}$	Kurz et al 2014, AHKN 2012
$A_3^{(8)}(m_e/m_\mu, m_e/m_\tau)$	$0.746\,87\,(28)\times10^{-6}$	Kurz et al 2014, AHKN 2012
$A_1^{(10)}$	$6.737\,(159)$	AKN 2018,2019
$A_2^{(10)}(m_e/m_\mu)$	$-0.003\,82\,(39)$	AHKN 2012,2015
$A_2^{(10)}(m_e/m_\tau)$	$\mathcal{O}(10^{-5})$	
$A_3^{(10)}(m_e/m_\mu, m_e/m_\tau)$	$\mathcal{O}(10^{-5})$	

Figure 1.2: Value and uncertainty of the coefficients A_i^{2n} of (α/π), here n denotes the 2nth-order of the perturbation theory of QED. This table is extracted form the reference[8]

1.2 Electron magnetic moment anomaly

1.2.1 Theoretical value of a_e

The theoretical value of the electron magnetic moment anomaly has three contributions: the electroweak, hadronic and QED contributions.

$$a_\mathrm{e}(\mathrm{theo}) = a_\mathrm{e}(\mathrm{QED}) + a_e(\mathrm{Hadron}) + a_e(\mathrm{Weak})$$

The term $a_e(\mathrm{Weak})$ involves the weak bosons and the term $a_e(\mathrm{Hadron})$ account for the interaction with quarks or hadrons without a weak boson. Since the electron is much lighter than the weak bosons and hadrons, the major contribution comes from the QED term. Indeed, $a_e(\mathrm{Weak})$ and $a_e(\mathrm{Hadron})$ accounts for only 0.026 ppb [35, 29, 30] and 1.47 ppb [58, 49], respectively, of the whole contribution.

The high-order QED corrections are formulated as a power series in α.

$$a_\mathrm{e}(\mathrm{QED}) = \sum_{\mathrm{n=1}}^{\infty} A_\mathrm{e}^{(2n)} \left(\frac{\alpha}{\pi}\right)^n + \sum_{\mathrm{n=1}}^{\infty} A_{\mu,\tau}^{(2n)} \left(\frac{m_\mathrm{e}}{m_\tau}, \frac{m_\mathrm{e}}{m_\mu}\right) \left(\frac{\alpha}{\pi}\right)^n$$

In this formula, we distinguish the coefficients $A_\mathrm{e}^{(2n)}$ independent of the mass which involves only the electron and those depending on the mass of the two other leptons which involves the creation and anihilation of those particles in antiparticle. These coefficients are calculated to the fifth order using the technique of Feynmann diagrams. The table 1.2 summarises the most recent values of these coefficients.

Using the values of the fine structure constant published by the group of Holger Müller in 2018 [59] and our group in 2011[18], one can calculate the theoretical value of the electron

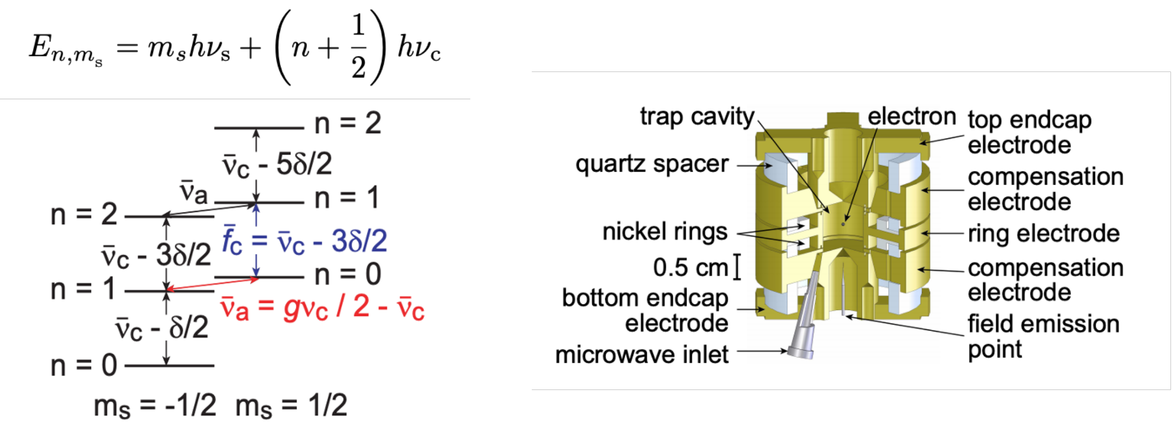

Figure 1.3: measurement principle of the electron magnetic moment anomaly . Left) the energy level of single electron submitted to the magnetic field. Right) experimental setup used by Gabrielse group to measure cyclotron and spin frequencies. These two figures are extracted from the reference [43]

magnetic moment anomaly. We obtain

$$a_{\mathrm{e}}\left(\mathrm{theo}, \alpha(\mathrm{Rb2011})\right) = 1159652182.037\,(720)(11)(12) \times 10^{-12}$$

$$a_{\mathrm{e}}\left(\mathrm{theo}, \alpha(\mathrm{Cs2018})\right) = 1159652181.606\,(229)(11)(12) \times 10^{-12}$$

where the uncertainties quoted are due respectively to α, numerical evaluation of the tenth-order QED, and the hadronic contribution. Thus the uncertainty on the theoretical value of the electron magnetic moment anomaly is dominated by the uncertainty on the fine structure constant α.

1.2.2 Measurement of the electron magnetic moment anomaly

The g_{e} factor of the electron is measured by only one group in the word, the group of G. Gabrielse at Harvard university. The experiment measures directly the cyclotron and abnormal frequencies using quantum-jump spectroscopy of a single electron trapped in penning trap and submitted to a magnetic field (see figure 1.3).

$$\frac{g_{\mathrm{e}}}{2} = \left|\frac{\mu_{\mathrm{e}}}{\mu_{\mathrm{B}}}\right| = \frac{\nu_{\mathrm{s}}}{\nu_{\mathrm{c}}} = 1 + \frac{\nu_{\mathrm{s}} - \nu_{\mathrm{c}}}{\nu_{\mathrm{c}}} = 1 + \frac{\nu_{\mathrm{a}}}{\nu_{\mathrm{c}}}$$

This method proposed by G. Dehmelt et al.[76, 77] has two main advantages, the magnetic field dependence drops out of the ratio and as the cyclotron and the spin frequencies differ by 10^{-3}, measuring the frequencies with an accuracy of 10^{-10} allows to reach an accuracy of 10^{-13} on g_{e}. In 2008, Gabrielse's group obtained a measurement of a_{e} with a relative uncertainty of 0.28 part-per-trillion [43]

$$a_e(\exp) = \frac{g_e - 2}{2} = 0.00115965218073\;(28)\;[0.28\ \mathrm{ppt}]$$

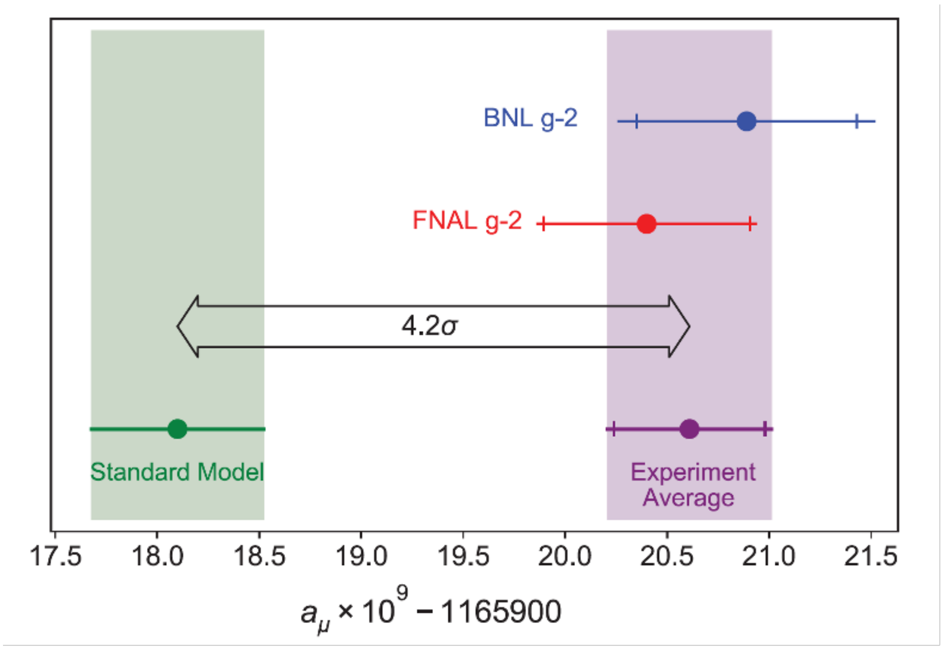

Figure 1.4: Theoretical and experimental values of the muon magnetic moment anomaly.

Dominant systematic effects come from the residual motion of the electron and the magnetic field gradient. Currently the group is building a new experimental setup to mitigate these effects. In particular they will measured the spin and cyclotron transition frequencies nearly simultaneously. They expect an improvement in uncertainty by a 10-fold factor [33]

1.3 The muon magnetic moment puzzle

Improving the uncertainties on the theoretical and experimental values of a_e is partly motivated by the muon puzzle: the persistent discrepancy between the theory and the experiment. Measurement of a_μ is much trickier than for electron. Because it is short-lived, the muon is less suitable for experiments using Penning traps, in which stable charged particles are confined by static magnetic and electric fields. Measurement of spin and cyclotron frequencies are performed in a storage ring. Theoretical calculations are also more difficult, especially the hadronic contributions which are more significant than for the electron because the muon is more massive. Recent measurement of a_μ performed in 2021 at Fermi-lab [1] confirmed the previous measurement in E821 Experiment at the Brookhaven [45] The Figure 1.4 shows a persistent discrepancy of 4.2σ between experiment and theory that has recently been thoroughly investigated [7],

$$\delta a_\mu = a_\mu(\mathrm{Exp}) - a_\mu(\mathrm{SM}) = (251 \pm 59) \times 10^{-11} \tag{1.3}$$

If this discrepancy is the signature of new physics beyond the standard model, it should be observed on the electron. Using a naive scaling [37, 72], one can evaluate the corresponding effect on the electron,

$$|\delta a_\mathrm{e}| = |\delta a_\mu| \left(\frac{m_\mathrm{e}}{m_\mu}\right)^2 \simeq 5.8 \times 10^{-14} \tag{1.4}$$

Thus to observe equivalent effect on the electron one must have a relative uncertainty on $a_\mathrm{e}(\mathrm{theo})$ and $a_\mathrm{e}(\mathrm{exp})$ less than a few 10^{-14}, which is not the case yet. This would require an improvement by a factor of 10 in the a_e experimental value and more importantly a determination of the fine-structure constant with an accuracy of the order of 10^{-11}.

1.4 Determination of the fine structure constant from the recoil measurement

From equation 1.2, we can express the fine structure constant as a function of the ratio h/m_e.

$$\alpha^2 = \frac{2R_\infty}{c}\frac{h}{m_\mathrm{e}} = \frac{2R_\infty}{c}\frac{A_\mathrm{r}(\mathrm{at})}{A_\mathrm{r}(\mathrm{e})}\frac{h}{m_\mathrm{at}}$$

As it is difficult to measure the absolute mass of the electron, we introduce the relative masses of an atom $A_\mathrm{r}(\mathrm{at})$ and the electron $A_\mathrm{r}(\mathrm{e})$ which are measured respectively with a relative uncertainty of 7×10^{-11} for rubidium 87 [12] and 2.9×10^{-11} for the electron [70]. Since the Rydberg constant is measured by hydrogen spectroscopy with an accuracy of 1.9×10^{-12} [73], the uncertainty on α is currently limited by the uncertainty of the ratio h/m_at. In our group we deduce this ratio from the measurement by atom interferometry of the recoil velocity of an atom of mass m_at that absorbs a photon of momentum $\hbar k$, where k is the wave vector.

$$v_\mathrm{r} = \frac{\hbar k}{m_\mathrm{at}} \tag{1.5}$$

The recoil velocity is 5.6 mm/s for rubidium 87 and 3.5 mm/s for caesium.

Currently, only two groups in the world measure atomic recoil to determine the fine-structure constant. Holger Müller's group at Berkeley measures the recoil of the caesium 133 atom. Our team started this project in 1998 using rubidium. We combine two techniques to improve the precision of this recoil measurement.

- Coherent acceleration using Bloch oscillation in accelerated optical lattice. This method allows us to transfer about $N = 1000$ photon momenta to the atoms in 6 ms. The transfer efficiency is 99.93% per Bloch oscillation. So we send a large amount $N = 1000$ of recoil velocities to the atom in a very short time. This way strongly reduce our statistical uncertainty.
- Atom interferometry: we use a Ramsey Bordé interferometer to measure the Doppler shift induced by N recoil velocity. It consists of 2 pairs of $\pi/2$ light pulses. Each one induces a stimulated Raman transitions. The spacing time between the two pairs of $\pi/2$ pulses is $\mathrm{T_R} = 20\mathrm{ms}$ which corresponds to a theoretical sensitivity

$$\frac{1}{N_B T_R} = 0.05Hz \tag{1.6}$$

The results presented in this manuscript have been obtained with the third version of the experimental set-up.

1.5 Plan of the manuscript

This manuscript is organised in two parts with five chapters. The part I is devoted to the **determination of the fine-structure constant with 81 ppt**. It contains three chapters.

In chapter 2 , we will present the fundamental concepts of the experiment. We will briefly present the principle of Raman transition and Bloch oscillations phenomena in an accelerated optical lattice that are at the heart of the measurement. The different configurations of atom interferometer will also be briefly introduced.

chapter 3 shows our experimental setup and how we implement the concepts mentioned in chapter 1 on the experiment.

In chapter 4 , the experiment protocol is discussed and we present our last determination of α [55]. The statistical performance of our experiment is shown: currently we are not limited by the statistical uncertainty but by the systematic effects. Subsequently, we will discuss the three biggest systematic effects in our experiment, which is related with the beam profile and cloud expansion.

We expect that the use of Bose-Einstein Condensates (BEC) will mitigate some systematic effects we mentioned in chapter 4. The following part is about the atom interferometer with BEC and is made of two chapters.

In chapter 5, we will give some general information about Bose-Einstein Condensates and show the expansion of the cloud calculated from Castin&Dum's model in the Thomas-Fermi regime. At the end we will show how we generate the BEC in our experiment.

In chapter 6, the effect of atomic interactions in BEC is studied by using a so-called Mach-Zehnder atom interferometer. We proposed two different theoretical models to study it: model A consists in solving the time dependant Gross-Pitaevskii Equation by using the Castin&Dum's model and model B consists in using the Feynman path integral approach to study this effect. The two gives the same result but model B can also be used to study the inhomogeneous spatial phase profile. The experiments are implemented and the theory models reproduces well the experimental results.

Part I

Determination of the fine-structure constant with 81 ppt

Chapter 2

The atom interferometry and atom accelerator

In the introduction, I have explained the purpose of this experiment and what we do in our experiment. If we want to use the determination of the α to test the Standard Model what we can do is improving the accuracy of the recoil velocity measurement.

This idea used in our experiment to ameliorate the accuracy is very similar with measuring the thickness of paper with a ruler. There are two things we can do to know better the thickness of the paper.

I. We should choose the most precise ruler to measure it. And in our experiment, this best quantum ruler or other words velocity sensor is atom interferometer with an accuracy σ.

II. In order to decrease the statistical uncertainty, we would like to measure thousands of papers together instead of just one paper. Our method is using Bloch oscillation to transfer N recoil velocities to the atoms. We combine these 2 techniques working well in our experiment and finally get a measure accuracy per sequence is

$$\sigma_{v_r} = \frac{\sigma}{N} \tag{2.1}$$

This chapter will first explain the counter propagating stimulated Raman transition acting as a beam splitter and some fundamental concepts of atom interferometry. At the end we will briefly talk about the Bloch oscillations.

2.1 Quantum ruler: Atom interferometer

2.1.1 Stimulated Raman transitions

The Rubidium $^{87}\mathrm{Rb}$ has two ground states $|F = 1\rangle$ and $|F = 2\rangle$ due to the hyperfine structure with a energy frequency difference ω_{HFS}. We consider only the excited state is

$5^2P_{3/2}\ |F=2\rangle$ (D_2 line). In the following discussion, these states will be called $|1\rangle$, $|2\rangle$ and $|e\rangle$. In order to connect the two ground state, we use the two-photon transition in a Λ scheme with two different laser fields $[\vec{k}_1, \omega_1]$ and $[\vec{k}_2, \omega_2]$.

$$\vec{E}_i(\vec{r}, t) = \vec{E}_{i,0} \exp\left(i\left(\vec{k}_i \cdot \vec{r} - \omega_i t + \phi_0\right)\right) \tag{2.2}$$

where ϕ_0 is the initial phase of the laser field, because these two lasers in our experiment are well phase controlled so in the following we will conisder $\phi_{\mathrm{i},0} = 0$. Two photon transition is a very useful tool in spectroscopy because it can be used to either enhance or suppress the Doppler effect. The energy level is shown in Figure 2.1 .

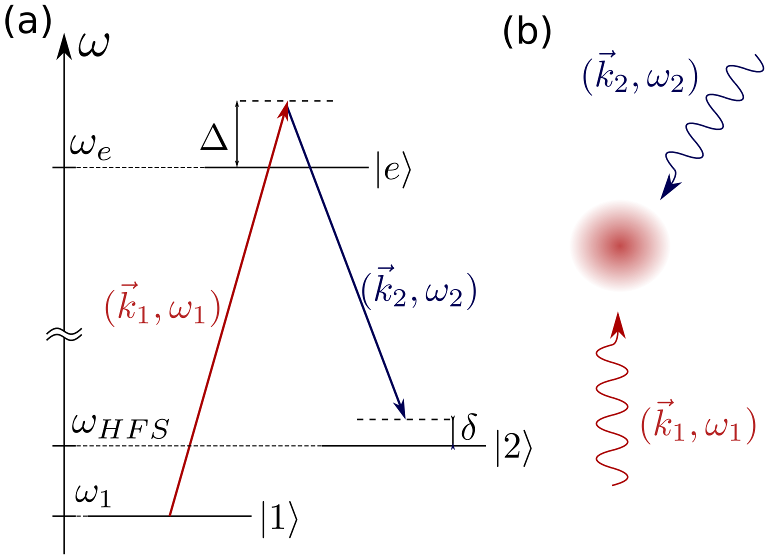

Figure 2.1: (a): Three level system for the description of Raman transitions. The excited state is coupled to the two ground states through two beams that are detuned by Δ, which in our experiment is $\sim$ 65 GHz. And the two different ground states is separated by $\nu_{\mathrm{HFS}} \sim 6.8$ GHz. The two photon detuning δ is set to select atoms with given velocity. (b):Example of a geometric configuration where an atom is subjected to two beams. Extractedd from [54]

Resonant Condition

The two photon transition gives us a way to couple two hyperfine states, with laser source in optical domain instead of microwave: when the atom transfers from $|F=1\rangle$ to $|F=2\rangle$ the atom will absorb a photon with $[\vec{k}_1, \omega_1]$ and stimulated emit a photon with $[\vec{k}_2, \omega_2]$.

Based on the momentum and energy conservation we can find out the resonant condition is :

$$\delta = \omega_1 - \omega_2 - \omega_{\mathrm{HFS}} = \frac{\vec{p_i} \cdot \vec{k}_{\mathrm{eff}}}{m} + \frac{\hbar ||\vec{k}_{\mathrm{eff}}||^2}{2m} \tag{2.3}$$

where $\vec{k}_{\mathrm{eff}} = \vec{k}_1 - \vec{k}_2$. The second part of this equation is the Doppler shift induced by the recoil velocity of the atoms. The effective wave vector $\vec{k}_{\mathrm{eff}}$ can be different in two configurations:

Co-propagating: $\vec{k}_1$ and $\vec{k}_2$ have the same direction, then k_{eff} has a magnitude very small compared to $|\vec{k}_1|$ or $|\vec{k}_2|$, then Doppler effect is negligible.

Counter-propagating: $\vec{k}_1$ and $\vec{k}_2$ the magnitude of $k_{\text{eff}} \approx k_1 + k_2$, thus counter-propagating Raman transition are more sensitive to the Doppler effect.

As what we want to measure is the recoil velocity, in our experiment we always use the counter-propagating configuration. In this chapter we only focus on the counter-propagating configuration where we can easily address the Raman transition to atoms with a given velocity by scanning the two photon detuning δ.

Quantum dynamic description of Raman transition

Now we only consider the field $[\vec{k}_1, \omega_1]$ couples the state $|1\rangle$ to $|e\rangle$, the field $[\vec{k}_2, \omega_2]$ couples the state $|2\rangle$ to $|e\rangle$. Of course a more realistic model should take into account the action of field $[k_1, \omega_1]$ on $|2\rangle$ and vice versa.([24, 17]). But in order to understand what happens during the pulse, this simple model is enough.

Now we consider the atoms initial state $|1, \vec{p}, n_1, n_2\rangle$, where we include the momentum $\vec{p}$ of atoms and amplitude of the laser field $[\vec{k}_1, \omega_1]$ and $[\vec{k}_2, \omega_2]$. Due to the Raman lasers, three different state are coupled between each others:

$$\begin{aligned}
|1\rangle &= |1, \vec{p}, n_1, n_2\rangle \\
|2\rangle &= |2, \vec{p} + \hbar\vec{k}_{\text{eff}}, n_1 - 1, n_2 + 1\rangle \\
|e\rangle &= |e, \vec{p} + \hbar\vec{k}_1 n_1 - 1, n_2\rangle
\end{aligned}$$

where $\vec{k}_{\text{eff}} = \vec{k}_1 - \vec{k}_2$ is the effective wave vector. When there is no extra field, the free Hamiltonian of the subset $\{|1\rangle, |2\rangle, |\text{e}\rangle\}$ is

$$H_0 = \hbar \begin{bmatrix} \delta + \frac{\vec{p}^2}{2m} & 0 & 0 \\ 0 & \frac{\left(\vec{p} + \hbar\vec{k}_{\text{eff}}\right)^2}{2m} & 0 \\ 0 & 0 & \Delta + \frac{\left(\vec{p} + \hbar\vec{k}_1\right)^2}{2m} \end{bmatrix} \tag{2.4}$$

And now we add the two additional field $[k_1, \omega_1]$ and $[k_2, \omega_2]$, the coupling between the ground states and excited state induced by the laser fields are:

$$\hat{V}_i = -\hat{\vec{d}} \cdot \hat{\vec{E}}_i \tag{2.5}$$

where $\hat{\vec{d}}$ is the dipole operator of the atom and $\hat{\vec{E}}_i$ is the electric field operator associated to the field.

$$\hat{\vec{E}}_i = \sum_{i=1,2} \vec{\xi}_i \left(e^{ik_i\hat{x}} a_i - e^{-ik_i\hat{x}} a_i^\dagger\right) \tag{2.6}$$

where a_i are the annihilition operator of laser mode i.

We define the Rabi frequencies which describe the coupling strength between the states.

$$\begin{aligned}\frac{\Omega_1}{2} &= \tfrac{1}{\hbar}\langle e|\hat{V}|1\rangle \\ \frac{\Omega_2}{2} &= \tfrac{1}{\hbar}\langle e|\hat{V}|2\rangle\end{aligned}$$

which leads to a total Hamiltonian:

$$H = \hbar \begin{bmatrix} \delta + \frac{\vec{p}^2}{2m} & 0 & \frac{\Omega_1}{2} \\ 0 & \frac{\left(\vec{p}+\hbar\vec{k}_{\text{eff}}\right)^2}{2m} & \frac{\Omega_2}{2} \\ \frac{\Omega_1^*}{2} & \frac{\Omega_1^*}{2} & \Delta + \frac{\left(\vec{p}+\hbar\vec{k_1}\right)^2}{2m} \end{bmatrix} \tag{2.7}$$

Because the $\Omega_i \sim 2\pi 10\,\mathrm{MHz}$ is much smaller than the one photon detuning $\Delta \sim 2\pi 65\,\mathrm{GHz}$, the population of the excited state should be very small : nearly all the atoms stay in the two ground states $|F=1\rangle$ and $|F=2\rangle$. This allows us to simplify the three level Hamiltonian into a two level Hamiltonian.

$$H_e = \hbar \begin{bmatrix} \delta + \Omega_1^{\text{LS}} & \frac{\Omega_{12}}{2} \\ \frac{\Omega_{12}^*}{2} & \Omega_2^{\text{LS}} \end{bmatrix} \tag{2.8}$$

where the Ω_i^{LS} is the energy shift introduced by the defined field which is called light shift in the later discussion. They are proportional to the corresponding Rabi frequency

$$\Omega_i^{\text{LS}} = -\frac{|\Omega_i|^2}{4\Delta} \tag{2.9}$$

And the effective Rabi frequency coupling the state $|F=1\rangle$ and $|F=2\rangle$ is shown in below:

$$\Omega_{12} = \Omega e^{-i\phi} = -\frac{\Omega_1\Omega_2^*}{2\Delta} \tag{2.10}$$

where $\phi = \phi_2 - \phi_1$ is the difference phase of the two lasers.

Transition probabilities

Our three system can be simplified into an equivalent two level system. And we redefine the a total detuning δ_{tot} that accounts for the Doppler effect δ shown in (2.3) and light shifts

$$\delta_{\text{tot}} = \delta + \Omega_1^{\text{LS}} - \Omega_2^{\text{LS}} \tag{2.11}$$

Finally, we have the total effective Hamiltonian simplified as below (up to a constant energy):

$$H_e \; = \hbar \; \begin{bmatrix} \frac{\delta_{tot}}{2} & \frac{\Omega e^{-i\phi}}{2} \\ \frac{\Omega e^{i\phi}}{2} & \frac{-\delta_{tot}}{2} \end{bmatrix} \tag{2.12}$$

From the time dependant Schrödinger equation:

$$i\frac{\partial\psi}{\partial t}=\frac{H_e}{\hbar}\psi \tag{2.13}$$

we find out the the evolution operator of the system is :

$$U(\tau)=\begin{bmatrix}\cos\left(\frac{\Omega_{\text{eff}}\tau}{2}\right)-i\sin\left(\frac{\Omega_{\text{eff}}\tau}{2}\right)\frac{\delta_{\text{tot}}}{\Omega_{\text{eff}}} & -i\sin\left(\frac{\Omega_{\text{eff}}\tau}{2}\right)\frac{\Omega \mathrm{e}^{-\mathrm{i}\phi}}{\Omega_{\text{eff}}} \\ -i\sin\left(\frac{\Omega_{\text{eff}}\tau}{2}\right)\frac{\Omega \mathrm{e}^{\mathrm{i}\phi}}{\Omega_{\text{eff}}} & \cos\left(\frac{\Omega_{\text{eff}}\tau}{2}\right)+i\sin\left(\frac{\Omega_{\text{eff}}\tau}{2}\right)\frac{\delta_{\text{tot}}}{\Omega_{\text{eff}}}\end{bmatrix} \tag{2.14}$$

where the $\Omega_{\text{eff}}=\sqrt{\Omega^2+\delta_{tot}^2}$ is the effective Rabi frequency.

If all atoms are in the state $|1\rangle$ at the beginning, then after a pulse with duration τ, the probability to find atom in state $|2\rangle$:

$$\begin{aligned}P_{1\to 2} &= |\langle 2|U(\tau)|1\rangle|^2 \\ &= \frac{\Omega^2}{\Omega_{\text{eff}}^2}\sin^2\left(\Omega_{\text{eff}}\frac{\tau}{2}\right)\end{aligned} \tag{2.15}$$

When $\Omega_{\text{eff}}\tau=\pi$ (π pulse) then all atoms are transferred to $|F=2\rangle$ and the trajectopry of the cloud could be changed. While when $\Omega\tau=\frac{\pi}{2}$ ($\frac{\pi}{2}$ pulse) the output will be a half and half superposition $(|F=1\rangle+|F=2\rangle)/\sqrt{2}$ which can act as **quantum splitter**. So with the combination of π and $\frac{\pi}{2}$ pulses we can make a atom interferometry with cold atoms which will be discussed just later.

This Rabi spectra is plotted in Figure 2.2. From this we can see that the coupling width is proportional to the Rabi frequency. And also we notice that the width of the spectra scales inversely with the pulse duration. This can be interpreted as an illustration of the Heisenberg principle: as the pulse duration increases, its resonance frequency gets defined with a better precision. But even if we fix the pulse $\Omega_{\text{eff}}\tau=\pi$ then we find that the width selected is proportional to the Rabi frequency.:

$$\Delta v\approx\frac{\Omega}{k_{\text{eff}}} \tag{2.16}$$

This gives us an idea how to do a velocity sleclection before our atom interferometer. In our experiment the rabi frequency Ω can variate from several $5\,\text{kHz}$ to $20\,\text{kHz}$. If we continue discuss two situation co or counter propagating with a given Rabi frequency around $5\,\text{kHz}$ then we have

- **Co Propagating:** $\Delta v_{\text{Co}}\approx 220\,\text{m/s}$
- **Counter Propagating:** $\Delta v_{\text{Counter}}\approx 2\times10^{-3}\,\text{m/s}$

In our experiment, between the end of generation of molasses with temperature $4\,\mu\text{K}$ and the beginning of the atom interferometer we use two counter propagating pulses with Rabi frequency $5\,\text{kHz}$ to do a velocity preselection, which we will explain in chapter 4.

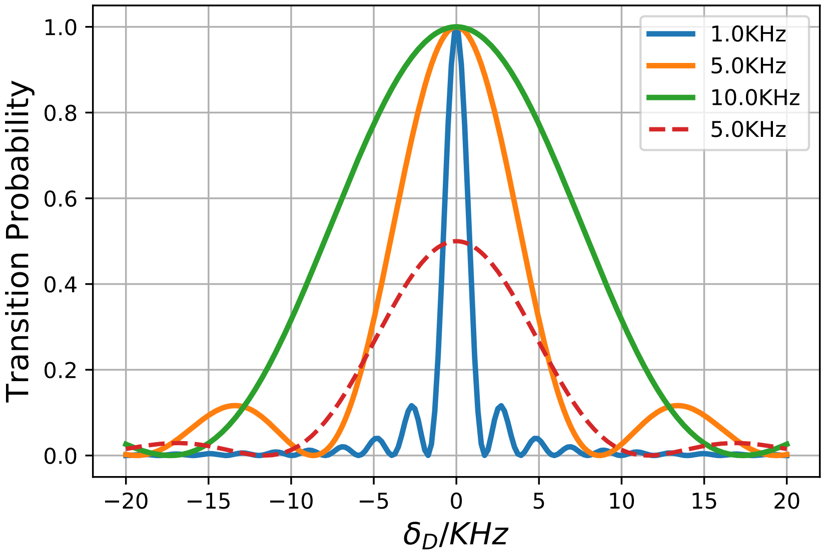

Figure 2.2: Transition probability after a single Raman pulse. The solid lines are π pulse where $\Omega_{eff}\tau = \pi$ and the dashed line is $\pi/2$ pulse where $\Omega_{eff}\tau = \pi/2$. The solid lines with different colors correspond different Rabi frequency

2.1.2 Atom interferometer

With the development of laser cooling, the first generation of the atomic interferometers [48] made a milestone of the precision measurement. Compared with the optical interferometry, the advantage of atom interferometry is that the matter wave, or equivalent the ultra cold atoms, is sensitive to forces. So this is a very good way to detect some tiny force, for example van der Waals force, the gravity or even the gravity gradient and the gravitational waves and so on. The principle is still the same, the interferometry signal depends on the phase difference between the two different trajectory.

In the following, I will give some general information about atom interferometry. The two arms of the atom interferometer is plotted in Figure 2.3. The total phase difference between two trajectories **A** and **B** can be divided into two parts: the phase due to the free propagation of the the atoms during between the pulses and the phase induced by the laser.

- **Free propagation:** This phase difference can be written as

  $$\Delta\phi_{\mathrm{L}} = (\mathrm{S}_{\mathrm{L}}^{\mathrm{A}} - \mathrm{S}_{\mathrm{L}}^{\mathrm{B}})$$

  where S_{L} is the Lagrange integral along the each path

  $$\mathrm{S}_{\mathrm{L}} = \int_{\mathrm{t_i}}^{\mathrm{t_f}} \mathcal{L}(z(t), \dot{z}(t))$$

  with the Lagrangien given by

  $$\mathcal{L}(z(t), \dot{z}(t)) = \frac{m\dot{z}^2}{2} - V(z)$$

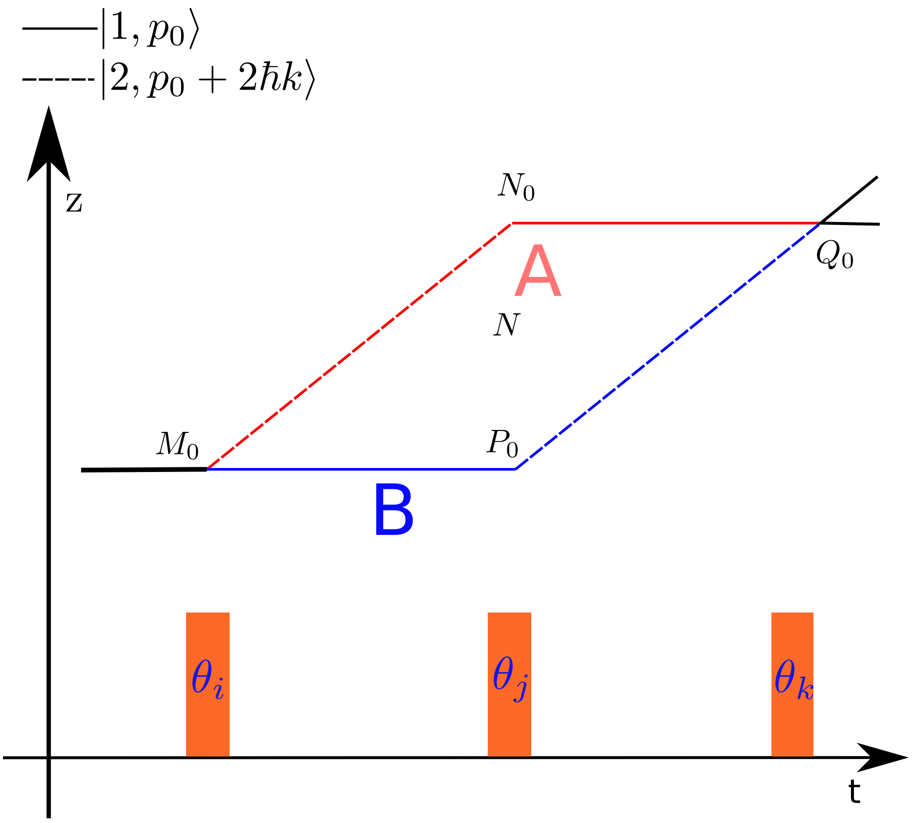

Figure 2.3: Schema of the different path of atom interferometer. The first pulse separates the atoms cloud and the last pulse make the two clouds recombine and close the atom interferometer

where the $V(z)$ is the potential the atoms felt at position z, which can also written in a formula with acceleration $V(z) = -maz$. If we have a uniform acceleration in the area of the interferometer, it can be shown that this part $\Delta\phi_{\mathrm{L}}$ vanishes.

- **Laser phase:** This part comes from the interaction between the atoms and fields. From (2.14) when at resonance we have the laser phase transfer to the atoms

$$\phi_l(t_i) = \begin{cases} \phi_{\text{laser}}(t_i) \quad \text{if} \quad |1\rangle \to |2\rangle \\ -\phi_{\text{laser}}(t_i) \quad \text{if} \quad |1\rangle \to |2\rangle \\ 0 \quad \text{if} \quad |\mathrm{i}\rangle \to |\mathrm{i}\rangle \end{cases} \tag{2.17}$$

where the laser is $\phi_{\text{laser}}(t) = \vec{k_{\text{eff}}}(t) \cdot \vec{r}(t) - (\omega_1 - \omega_2)\, t$.

AT the output of the interferometer the total phase shift on each path due to laser is

$$\phi_{\text{laser}} = \sum_{\mathrm{i}} \phi_l(t_i) \tag{2.18}$$

Then the phase difference at the output of the interferometry is :

$$\Delta\phi = \Delta\phi_{\mathrm{L}} + \Delta\phi_{\text{laser}} \tag{2.19}$$

Usually, the atom interferometer is closed and symmetric. Therefore, the propagation is zero $\Delta\phi_{\mathrm{L}} = 0$. More detail is explained in [46].

- **2 pulses configuration - Ramsey sequence**
- **3 pulses configuration - Mach-Zehnder interferometry**
- **4 pulses configuration - Ramsey Bordé interferometry**

2.1.3 Ramsey Sequence

Let's start with the 2 pulses configuration: Ramsey sequence

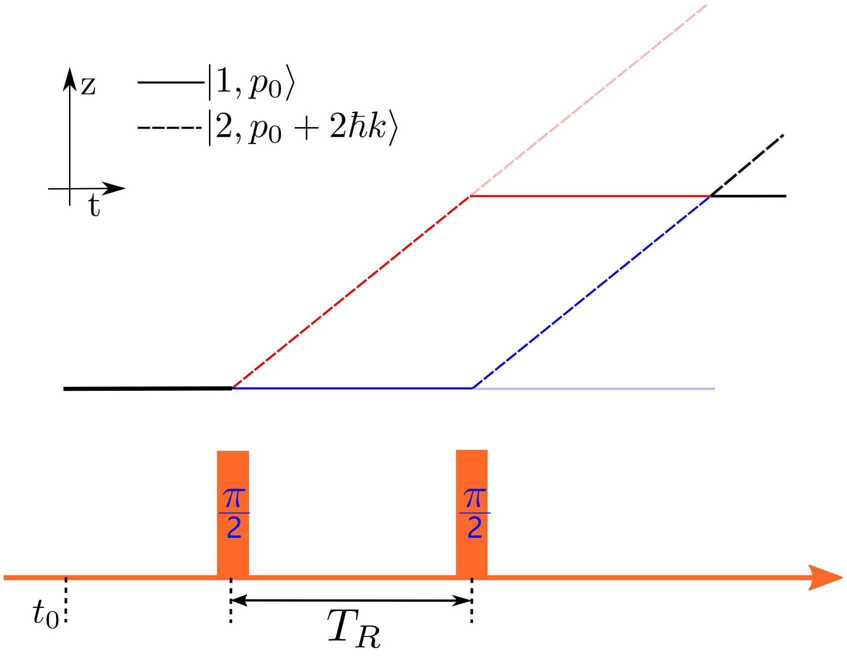

Figure 2.4: Pulse sequence of the Ramsey sequence $\frac{\pi}{2} - \frac{\pi}{2}$. The time delay between the two pulses is T_{R}

If we assume that the initial state is $|F = 1\rangle$ and after these two $\frac{\pi}{2}$ pulses the transfer probability will be (more calculation details in [54]):

$$P_{1\to2} = \frac{1 + \cos(\delta \times T_R + \Delta\phi)}{2} \tag{2.20}$$

where $\Delta\phi = \phi_1 - \phi_2$ is the phase difference between the two lasers. Because these two lasers are phase locked between each others, this phase is well controlled. To simplify the calculation in the later discuss, we assume $\Delta\phi = 0$. δ is the detuning seen by the atoms has already shown in (2.3). If in this measurement the resonant condition is satisfied, we should find out the central fringe and know the center velocity of the atoms. This should be discussed in two different situations:

- **Co Propagating:** The width in velocity space of the transition allows to address all the atoms and the inhomogeneous phase induce by the Doppler width is $\Delta v k_{\text{eff}} T_R \approx 40\,\text{mrad}$ with a $4\,\mu\text{K}$ molasses and $T_R = 10\,\text{ms}$. These phase shifts may result in a loss of contrast but at this order of magnitude, they do not damage the fringes signal. So this way can also be used to detect other systematic effects on the atoms, For example, the 2nd order zeeman effect.
- **Counter Propagating:** We suppose before the Ramsey sequence, we have already finished the velocity preselection, the Doppler width is $\sim \Omega_{12}$ and then the inhomogeneous phase induce by the Doppler width is $\Omega_{12} T_R \approx 50\,\text{rad}$ which is extremely big and totally destroy the signal. So Ramsey sequence in counter propagating configuration is not possible. But we can use two Ramsey Sequence to close this atom interferomter called Ramsey Bordé configuration, in this configuration the output is no longer sensitive with the entry velocity of cloud but the velocity change between these two Ramsey Sequences.

2.1.4 Mach-Zehnder Configuration

Now let's assume the atom feels some force so it will have an acceleration $\vec{a}$, and the laser propagation direction superposes with this acceleration. Mach-Zehnder interferometry is popular in the measurement of acceleration, for example the gravity. The pulse sequence is shown in the Figure 2.5.

In the Mach-Zehnder configuration, the last pulse closes the interferometer and it's symmetric. So the phase due t the propagation is zero $\phi_{\text{L}} = 0$. The phase difference at the end is $\Delta\phi = \Delta\phi_{\text{laser}}$. If during the interferometer we don't modulate the frequency of the laser, we can calculate the phase difference :

$$\Delta\phi = k_{\text{eff}} a T^2 \tag{2.21}$$

where k_{eff} is the effective wave vector. From this equation we can see that the sensitivity of acceleration a is $\propto 1/(k_{\text{eff}} T^2)$ and depends on time delay between each pulse. So we can increase the sensitivity by increasing the time delay T_R.

Now we sweep linearly the frequency of the laser $\omega = \omega_0 + \beta t$ with a sweep rate β. The final phase difference will be

$$\Delta\phi = (k_{\text{eff}} a - \beta) T^2 \tag{2.22}$$

So by scanning the rate β and measure the value for which $\Delta\phi = 0$, we can at the end get the value of acceleration $\mathbf{a} = \beta / k_{\text{eff}}$. This is an efficient way to measure acceleration precisely, for example the gravity $\vec{g}$.

2.1.5 Ramsey Bordé Configuration

What we used in our experiment is a Ramsey Bordé configuration, the pulse sequence is shown in Figure 2.6. Instead of a π pulse in the middle of the interferometer, we use two

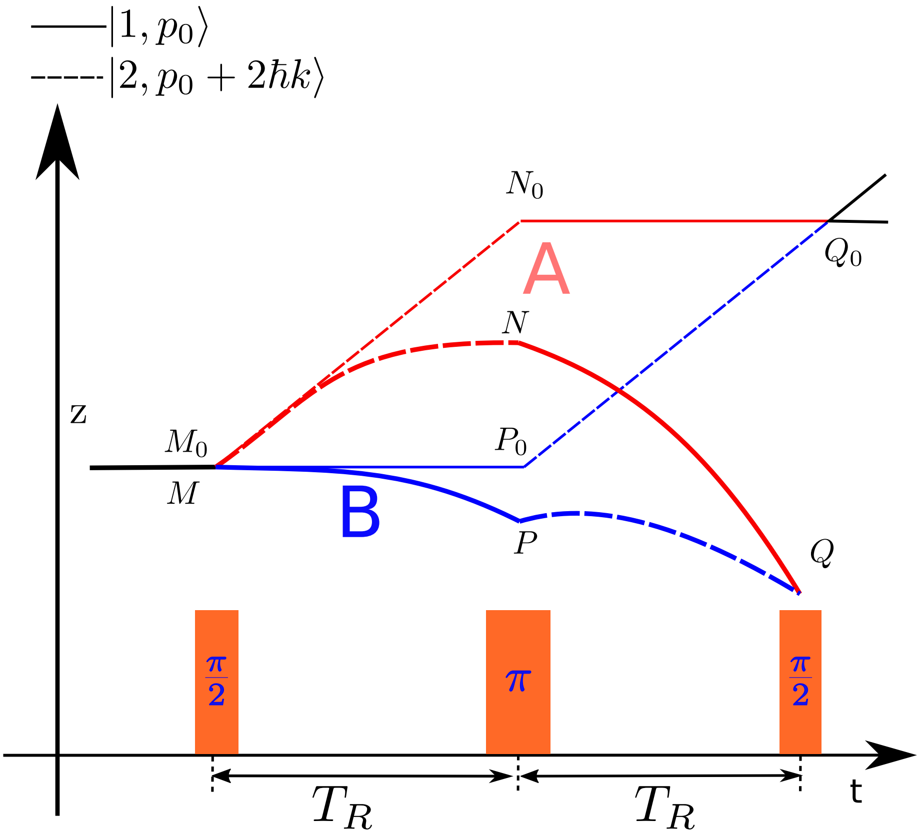

Figure 2.5: Pulse sequence of the Mach-Zehnder sequence$\frac{\pi}{2} - \pi - \frac{\pi}{2}$. The time delay between each pulse is T_{R}

$\pi/2$ pulses. A very big advantage of Ramsey Bordé configuration is that the internal state of the atoms between the two Ramsey sequence are the same and a lot of experimental manipulation can be applied in between, for example a velocity kick given by Bloch Oscillations.

At the output the phase difference between the two arms A,B will only depend on the laser phases which can be written as:

$$\Delta\phi = T_R(k_{\mathrm{eff}}\Delta v - \delta\omega) \tag{2.23}$$

where Δv is the velocity change between the first and third pulses and $\delta\omega$ is the frequency difference between the two Ramsey sequences. Different from single Ramsey sequence, Ramsey Bordé sequence can determine the center fringe by scanning the frequency difference $\delta\omega$ between the first and second pair of laser pulses. This gives us a good way to measure the recoil velocity.

h/m measurement

As we said in the introduction, we are doing the h/m measurement by measuring the atom recoil velocity v_r. In our experiment Δv contains the velocity change due to the gravity

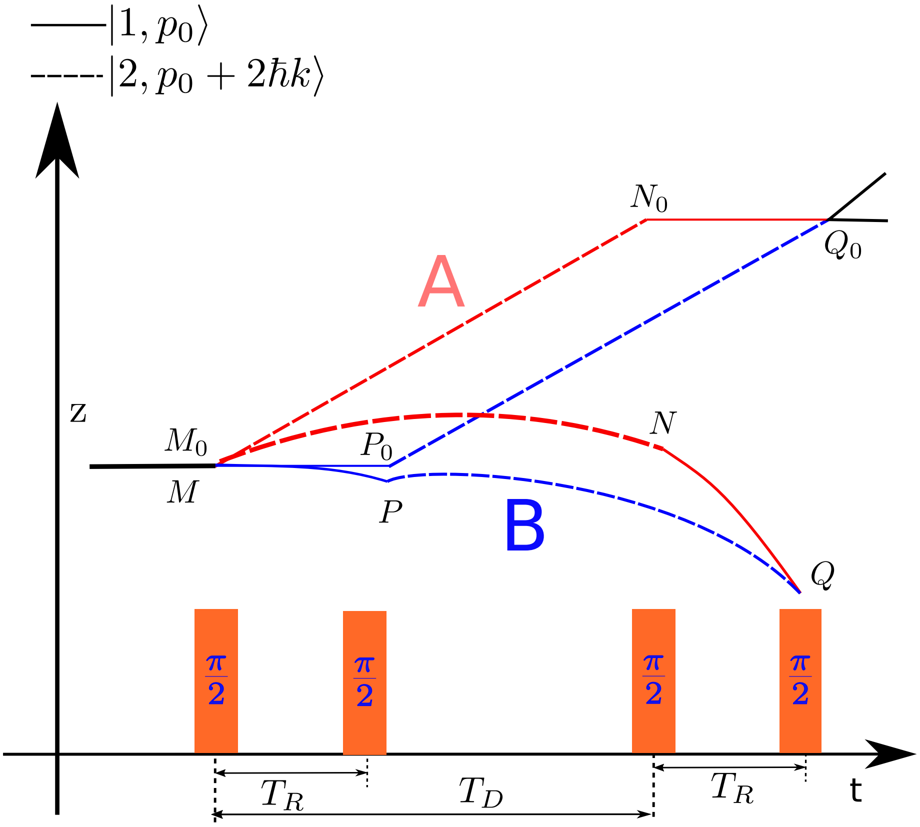

Figure 2.6: Pulse sequence of the Ramsey Bordé sequence$\frac{\pi}{2} - \frac{\pi}{2} - \frac{\pi}{2} - \frac{\pi}{2}$. The time delay in each Ramsey sequence is T_R and the time delay between two Ramsey sequence is T_D

and the acceleration of Bloch oscillations that transfer to atoms $2N_B v_r$. So at the output of the atom interferometer, the phase difference can be written more precisely (more detail will be presente in chapter 4):

$$\Delta\phi = T_R(k_{\text{eff}}(gT_D + 2N_B v_r) - \delta\omega) \tag{2.24}$$

2.2 Atom accelerator: Bloch oscillations

We have the precise 'quantum ruler': **atom interferometry**, now we should think about how we sum up thousand recoil velocities together to reduce the statistical uncertainty. The technique we use in the experiment is the **Bloch Oscillations**.

Here, a simple image can be used to understand the Bloch oscillations quickly: it is like a succession of counter propagating Λ transitions but with the atoms remaining in the same internal state. We display the energy-momentum diagram of such a process in Figure 2.7 (More details are shown in [20]).

Our experiment uses two vertical counter propagating Bloch lasers to generate a vertical optical lattice. From the Figure 2.7, we know that if we want to continuously apply the Bloch

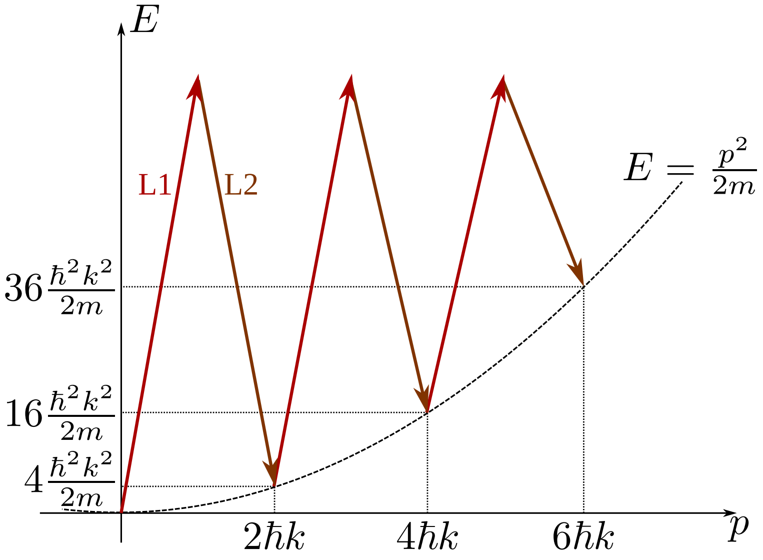

Figure 2.7: Energy momentum diagram of repeated Bloch oscillations. L_1 and L_2 are the corresponding Bloch lasers. Once the atoms are resonant with the lasers then it will do one Bloch oscillation and get two additional photon momentum $2\hbar k$.

oscillations to the atoms, we should sweep the frequency of Bloch lasers with $\delta\omega(t)$. Those two laser frequency is swept in opposite direction, which will shown in subsection 3.3.3. Then we can write the expression of the lasers' amplitude:

$$E^{\pm} = E_0 \mathrm{exp}\left(i\left(\pm\left(k \pm \int \frac{\delta\omega(t)}{c}\right)z - \left(\omega t \pm \int \delta\omega(t)dt\right) + \phi^{\pm}\right)\right) \tag{2.25}$$

where the sign ± shows the propagating direction of the beams: upward (+) or downward (-) and because these two lasers share the same laser source (seen in subsection 3.3.3) so the $\phi^+ = \phi^-$. They will generate a moving optical lattice with the potential [40].

$$V = V_0 \cos^2\left(kz - \int \delta\omega(t)dt\right) \quad \text{with} \quad V_0 = \frac{3\pi c^2}{2\omega_{\text{atom}}^3}\frac{\Gamma}{\Delta}4I_0 \tag{2.26}$$

where the ω_{atom} is atom resonance and $\Delta = \omega_{\text{laser}} - \omega_{\text{atom}}$ is the detuning of laser. In our experiment, it is blue detuned $\Delta > 0$, which means the atoms will be trapped at a minimum intensity to reduce the spontaneous emission caused by the Bloch lasers. In order to minimize the spontaneous emission, we far tune the Bloch from the atom resonance $\Delta \sim 40\text{GHz}$.

Here we define the recoil energy $E_r = (\hbar k)^2/2m$. Then we discuss the potential depth in two different situations:

- **Weak binding limit** $V_0 \ll 4E_r$**:** Lattice potential can be treated as a perturbation to the free case.
- **Tight binding limit** $V_0 \gg 4E_r$**:** The atoms are trapped in the potential wells. The higher the potential is, the harder for the atoms to escape from the potential.

In our experiment for each beam we have around $300\,\mathrm{mW}$ power that can generate a very deep potential $V_0 \sim 80E_r$. In this situation, the atoms are tightly trapped in the lattice. We image that now the atoms are closed in a box made by the optical lattice, so atoms will follow the motion of the optical lattice.

Now let us look back at the Equation 2.26. When we chirp the Bloch laser frequencies, we create a moving optical lattice at an acceleration:

$$a = \frac{\lambda}{2\pi}\frac{d\delta\omega}{dt} \tag{2.27}$$

where λ is the wavelength of the Bloch laser. Using this chirping principle, one can compensate for the motion of the free-falling atoms by setting $a = -g$ and taking gravity into account during the acceleration of the lattice. This compensation is used in the experiment when performing BO. Once we know the acceleration, we can deduce the Bloch oscillation period $\tau_B = (2\hbar k_B)/2ma$.

Typically in our experiment, the $\tau_B \sim 12\,\mu\mathrm{s}$ and $N_B = 500$, which means that now we can transfer 1000 recoil velocities to the atom is around $6\,\mathrm{ms}$. And each Bloch oscillation has a very high-efficiency 99.93%. This atom accelerator gives us an easy way to control the atoms precisely.

Chapter 3

The Experiment Set up

This research project, 'Measurement of h/m', started in 1998 in our group. During these 20 years, three versions of the experimental setup have been used to measure the ratio h/m. The previous version setup issued the determination of α with a relative uncertainty of $6.6\ \mathrm{times}10^{-10}$ in 2011. In order to improve the accuracy of this determination, a new design setup was started in 2013 and has been detailed in the previous PhD thesis of **Courvoisier** and **Jannin**([27],[46]).

During my PHD study, this last version of the experiment was already well implemented and ready to do the measurement. This chapter will give a description of our experiment setup.

In this chapter, we start by presenting the part about atom interferometer with laser cooled atoms using a molasses (the BEC setup will be described later).

- The vacuum cell and the setup to produce the atomic cloud
- The detection part: Time of flight detection.
- The interferometer laser system in our experiment.

3.1 Atomic sample generation

This experiment can prepare two different types of atomic sample: a molasses and a Bose-Einstein condensate (BEC).

- **Molasses:** within 1 second, we have 10^8 atoms in the atom cloud with temperature $4\mu K$ and a size $r \approx 600\mu m$
- **BEC:** within 3.2 seconds, we have 220 000 atoms in the atom cloud with temperature $80\,\mathrm{nK}$. This will be explained in the next part.

Figure 3.1: Left: Wood panel box protecting the experiment from the environment perturbation. Right: $\mu-\mathrm{metal}$ magnetic shield for the interferometer tube

3.1.1 Vacuum cell and outlook of set up

The schematic presentation of the vacuum cell is shown in Figure 3.2: Our vacuum cell is L-shape: the horizontal part is a 2D MOT which precools the atoms before they enter the main chamber. The center of the 'L' is the main chamber where the atom sample is prepared. The vertical part is the interferometry area where we implement the atom interferometry measurement.

The requirement of the vacuum cell is a pressure below 10^{-9} mbar to allow the trapped atom lifetime over 10s. We use NEXTorr pumps and an ion pump to meet this requirement. This way, we obtained a vacuum cell with 2×10^{-10} mbar continuously running for 4 years.

Finally, the vertical part is a tube surrounded by a solenoid to create a bias field along the vertical axis. Because we do the atom interferometer in the vertical part, we need to have a very controlled magnetic field that is well isolated from the surrounding environment. A two-layer cylindrical $\mu-\mathrm{metal}$ magnetic shield is used. The residual magnetic field is estimated below $100\,\mu\mathrm{G}$. Between the atom interferometer tube and the main chamber, a square chamber is used to detect the atoms.

Finally, the vacuum cell is surrounded by an aluminum profile system. We use wood panels to protect it from environmental noise (mainly air flow).

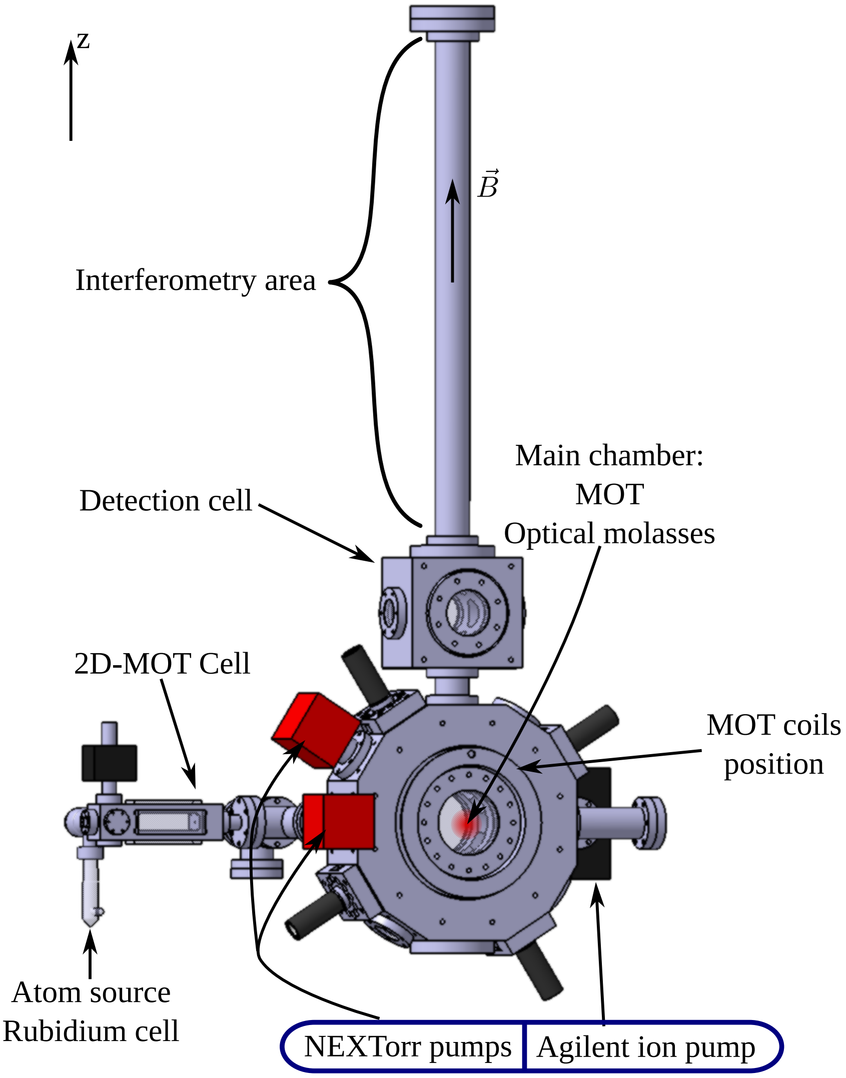

Figure 3.2: Schematic of the vacuum cell and main experiment part of our atom interferometer. The vertical bias field is generated by a solenoid wrapped around the tube of the interferometry area. It is isolated from the surrounding magnetic field by a magnetic shield not shown in this picture. Extracted from [54]

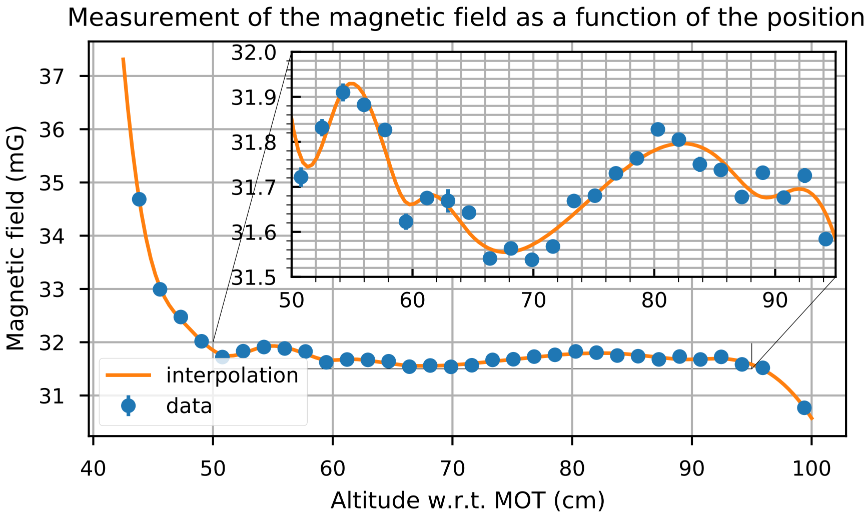

Figure 3.3: Measurement (blue dots) of the magnetic field as a function of the position. The orange line corresponds to an interpolation of the data by an unified spline.

Magnetic field measurement

The stability of magnetic field in the interferometer tube is important for our final accuracy of the determination of h/m. After the installation of the magnetic shield, we use the transition $|F = 1, m_{\mathrm{F}} = \pm 1\rangle \rightarrow |F = 2, m_{\mathrm{F}} = \pm 1\rangle$, which is sensitive to the magnetic field with sensitivity of $1.4\,\mathrm{MHz} \cdot \mathrm{G}^{-1}$ [69]. The details of measurement is seen in [54].

On the edges of the interferometer area, as such of the solenoid and the magnetic shield, the magnetic field exhibits significant variations. However, in the center of this area, in a $45\,\mathrm{cm}$ long distance, we have a well controlled magnetic field with local gradients less than $4\,\mathrm{mG/m}$ where we can run our atom interferometer.

3.1.2 Atom trapping lasers

In the magneto-optical trap, two lasers are used. One is the cooling laser which makes a σ^+ transition from $|F = 2\rangle \rightarrow |F^{'} = 3\rangle$ such that the atoms cannot fall back to $|F = 1\rangle$ and remain trapped. Another one is the repump laser, because $|F = 2\rangle \rightarrow |F^{'} = 2\rangle$ transition is not strictly forbidden and from $|F^{'} = 2\rangle$ the atoms may fall back into $|F = 1\rangle$. In order to put all atoms back to $|F = 2\rangle$, this repump laser is set resonant with transition $|F = 1\rangle \rightarrow |F^{'} = 2\rangle$. The frequency of laser used in the experiment is shown in Figure 3.4.

The property of our atom sample is highly related to the frequency of the cooling laser. Then the important thing is to well control the frequency of the two lasers.

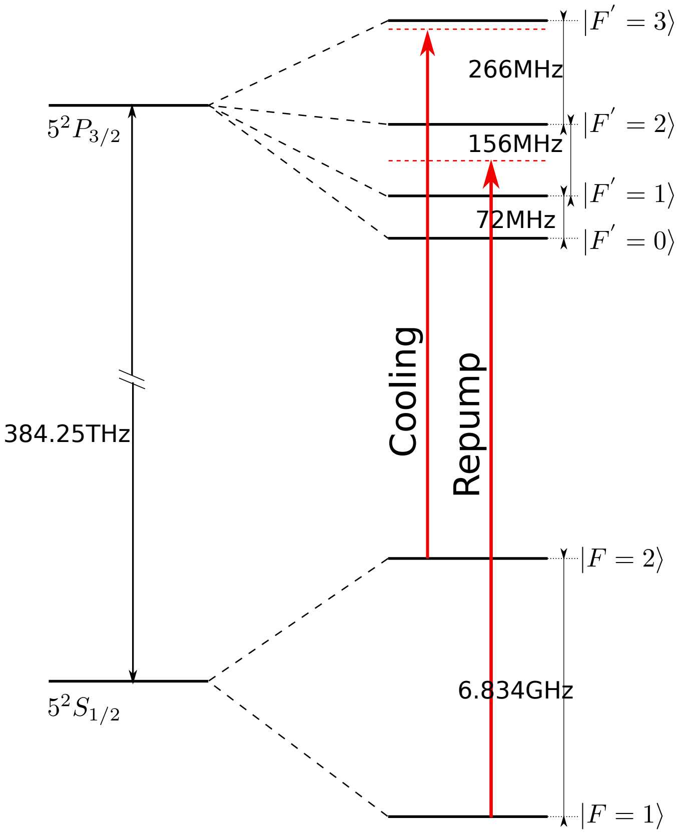

Figure 3.4: The frequency of Repump and Cooling lasers are presented with $^{87}Rb\ D_2$ transition hyperfine structure, with frequency splittings between the hyperfine energy levels.

Repump and Cooling laser system

The two lasers are generated through laser diodes (Thorlabs L785P090) in Extended Cavity Diode Laser (ECDL) configuration [14]: the laser diode is placed in a Fabry-Pérot cavity. One end of the cavity is a mirror, and the other is the diode itself. Inside the cavity, an interference filter is used to filter a lasing mode at 780 nm. This system's output is around 20 mW per diode. The output passes through a Faraday isolator to protect the diode from feedback light and then split into different parts for frequency manipulation on the lasers.

- First, a small part of the repump is split and sent to the saturated absorption box to lock the repump laser frequency on the crossover of the $|F^{'}=1\rangle$ and $|F^{'}=2\rangle$[52]. Because the frequency difference between the $|F^{'}=1\rangle$ and $|F^{'}=2\rangle$ is around $160\ \mathrm{MHz}$, the $80\ \mathrm{MHz}$ difference between the crossover could be compensated through the acoustic optical modulator (AOM) later in our experiment.
- Part of the cooling and repump lasers are superposed and sent to a photodiode to produce a beat note. This beat note is then frequency locked with a variable reference

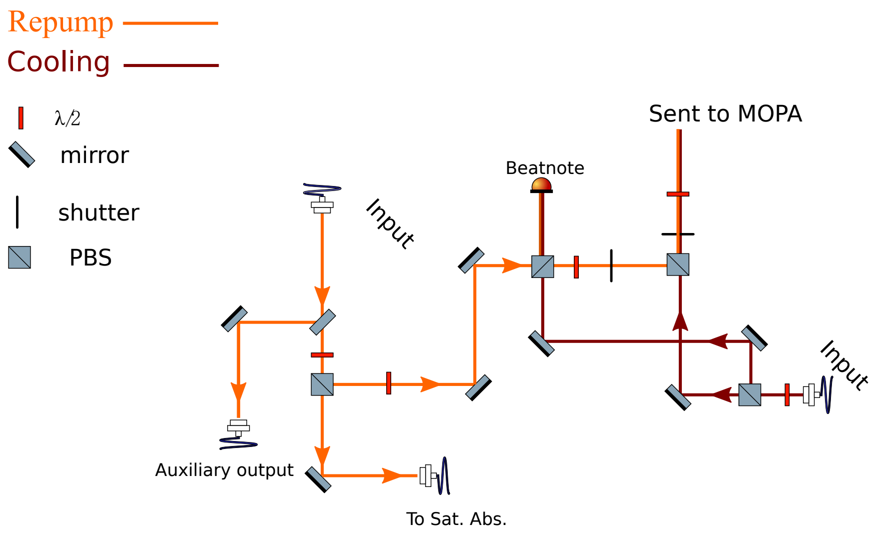

Figure 3.5: The module of trapping laser frequency control.

microwave signal such that we have a dynamic control on the cooling laser frequency.

- Most of the repump and cooling power is sent directly to the Master oscillator power amplifier (MOPA) after passing through a Faraday isolator. During my phd, we had tp remove the fiber coupler because we changed to a new MOPA which needs more input power. Moreover, this configuration reduces the power fluctuation after the Faraday isolator before the input of MOPA.

For now, we have a very stable laser frequency lock system which can continuously run for many hours without jumping out of the lock.

Magnetic optical trap

Optical cooling is an efficient way to cool down the atoms and get an ultra cold atom cloud. With 6 laser beams we can cool down the atom cloud in three dimensions and obtain an optical molasses in the experiment. By this way we can cool down the atoms to get a cloud at temperature $\sim 4\mu K$ [75, 31]. However, with only an optical trap, the atoms will be placed everywhere with a very low density. In order to circumvent this problem, we add a magnetic field to form a magneto-optical trap (MOT)[32, 62] and have a 3D MOT after a 2D MOT[63]. This configuration allows for higher density and loading rate.

This magnetic field is generated from a pair of coils in an anti-Helmholtz configuration. The current through the coils is controlled by an analog signal which allows us to tune it up to $\sim 15\mathrm{G/cm}$ maximum. Moreover, we need to make the center of the magnetic quadrupole overlap with the center of molasses to have efficient molasses. We used three pairs of coils, each corresponding to a spatial direction, to compensate for the residual magnetic field.

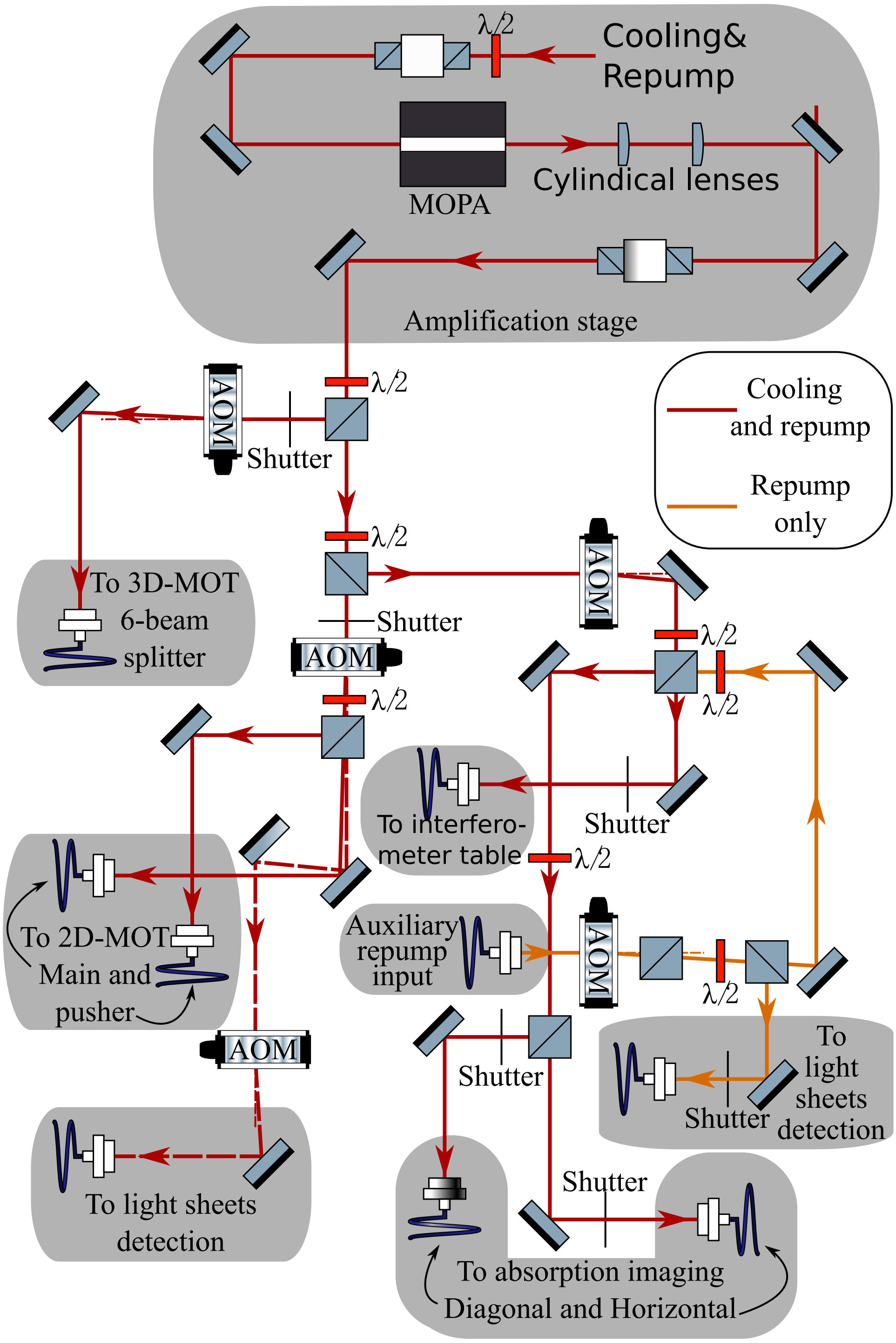

Figure 3.6: Schematic representation of the MOT tables.The input of the MOPA is directly from Figure 3.5. This table contains not only the lasers used in the MOT but also the lasers for the detection.

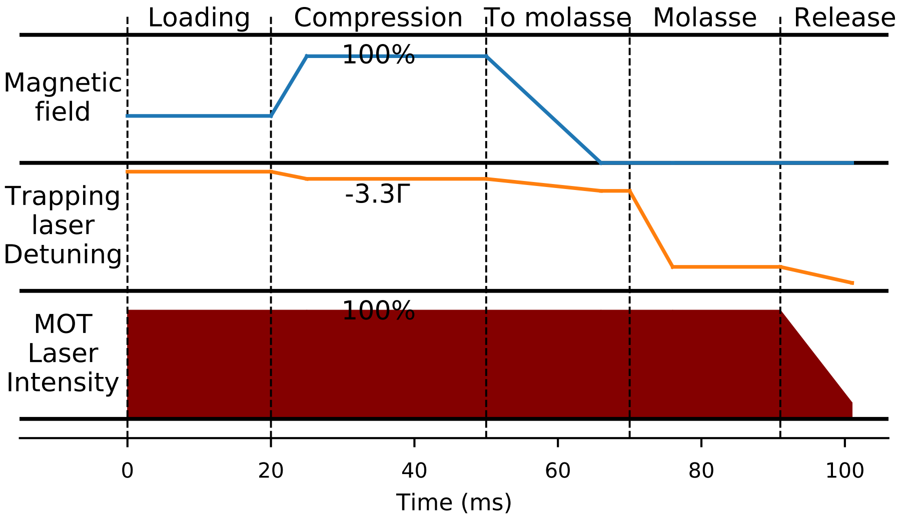

Figure 3.7: Steps sequence for the optical molasses

Generation of molasses

All the lasers used in the generation of molasses are presented in Figure 3.6, including the lasers used for detection.

To get efficient optical molasses, we follow a few steps shown in Figure 3.7. First, we have around $600\,\mathrm{ms}$ MOT loading time, which is limited by the duration of the sequence. During the loading process, the detuning of the cooling laser is set to $\sim -1.9\Gamma$ and the magnetic gradient is around $9\,\mathrm{G}\cdot\mathrm{cm}^{-1}$. Then we quickly increase the magnetic gradient to maximum $15\,\mathrm{G}\cdot\mathrm{cm}^{-1}$ while the cooling frequency is swept to $\sim -3.3\Gamma$. We call this process 'Compress MOT', which can slightly compress the cloud to get a higher density. This process lasts for 25ms and maximizes the density of the atom cloud.

Then the magnetic field is switched to zero in $20\,\mathrm{ms}$, and simultaneously the cooling is detuned from -3.3Γ to -6Γ. Now we reach the molasses phase, and then we detune the cooling laser frequency to be -22Γ and wait for $15\,\mathrm{ms}$. Finally, we shut down the power of the laser and release the cloud by ramping down the laser's intensity 15% of its maximum value in 10 ms before an abrupt shutoff. The total duration of this stage is approximately $80\,\mathrm{ms}$, so the total time to get the final optical molasses with $4\,\mu\mathrm{K}$ is around $700\,\mathrm{ms}$.

3.2 Detection

In our experiment we have two different ways to detect atoms: Absorption imaging and light sheets detect.

- **Absorption imaging:** Detect the atom sample in the main chamber. We will talk about it in the next part dedicated to the BEC.

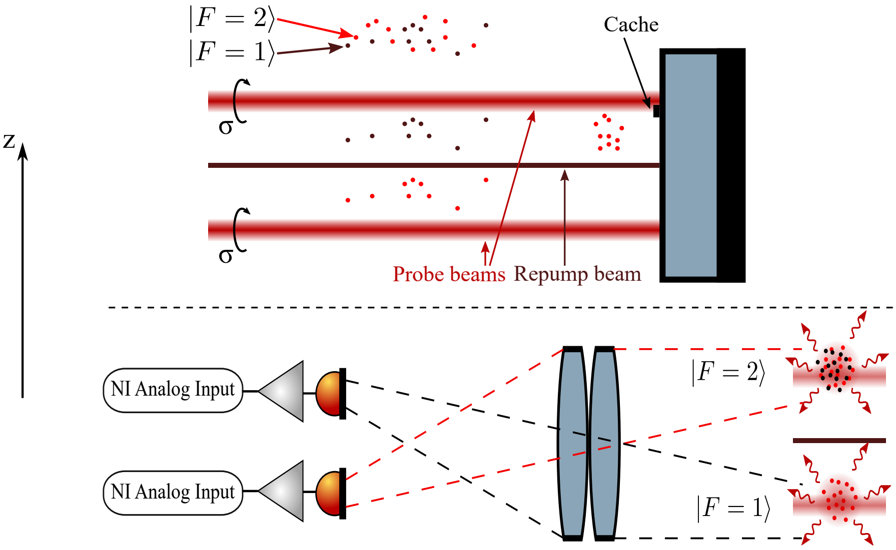

Figure 3.8: Schematic of the detection setup from a view from the side. On top the picture shows the counterpropagating circularly polarized light sheets. As the atom falls, the figure reads from top to bottom. The atoms in$|F=2\rangle$ are detected in the first light sheet and blown away thanks to the mask on the retro reflecting mirror. The remaining atoms, in $|F=1\rangle$, are then repumped and detected. On the bottom, a view of the imaging system : the atom cloud is imaged on photodiodes, whose signals are then amplified and recorded.

- **Light sheets detection:** Detect the atom sample falling down after the atom interferometer.

3.2.1 Light sheets detection

As we discussed before, when we do the measurement of h/m, the atom interferometer sequence happens in the vertical tube where the magnetic field $\vec{B}$ is well controlled. When it falls back, the minimum velocity of the cloud is around $3\,\mathrm{m/s}$, and it is no longer possible and suitable to detect them by using absorption imaging. In this situation, we use the collection of fluorescence photons emitted by the atoms in a probe light sheet. The schematic presentation is shown in Figure 3.8:

To present this detection process, let us imagine that the atom cloud finished the atom interferometer, and now it has two components of atoms in $|F=1\rangle$ and $|F=2\rangle$. When the atoms pass through the first probe light sheet, the atoms in $|F=2\rangle$ will get excited and blown away, but it will not affect the atoms in $|F=1\rangle$. So the remaining atoms in $|F=1\rangle$ will be repumped to $|F=2\rangle$ in the repump light sheet and detected in the second probe light sheet.

The probe laser is σ^+ polarization which can avoid the atoms falling back into $|F=1\rangle$. And a tiny bottom part of the probe light sheet is blocked by black paper, which can blow away the atoms in $|F = 2\rangle$ from the detection area. A lens system, which is made up of two *Thorlabs AC508-080-b* achromatic lenses, collects all the spontaneous emissions from the probe light sheets and sends them to two different photodiodes. An example of a signal is plotted in Figure 3.9

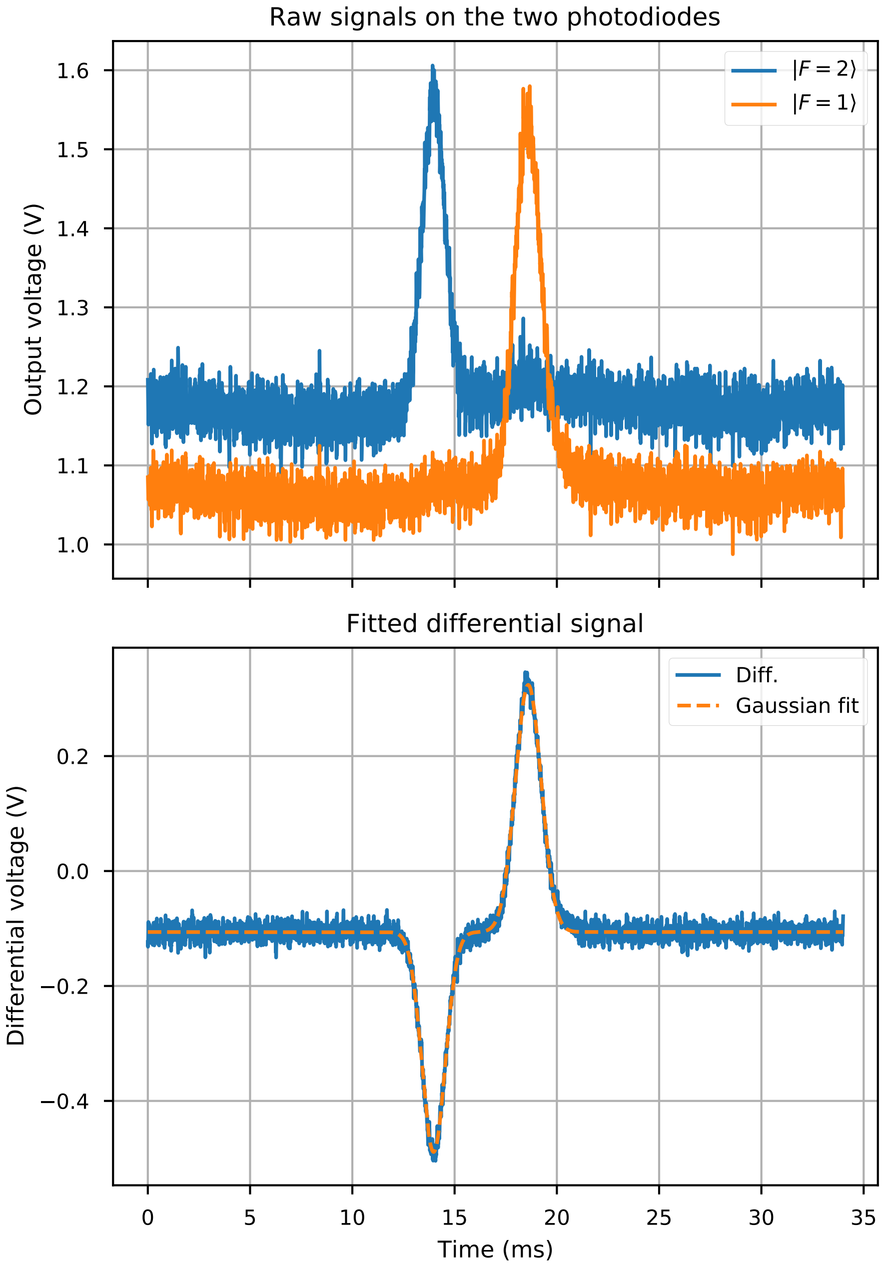

Figure 3.9: Signals obtained with the light sheets detection. Top: raw signals of each photo diodes. Bottom: differential signal for processing and its fit with two gaussians.

We analyze the difference between the two signals to cancel the common noise on these two photodiodes. Then this difference can be fitted with two different gaussian functions:

$$f(t) = -a_2\text{exp}\left(-\left(\frac{t-t_2}{w_2}\right)^2\right) + a_1\text{exp}\left(-\left(\frac{t-t_1}{w_1}\right)^2\right) + \text{offset} \qquad (3.1)$$

In this equation the subscript 1,2 correspond to the internal state of atoms $|F=1\rangle$ and $|F=2\rangle$. In particular, the widths of the two signal are very close $w_1 \approx w_2$ so that we take the amplitudes a_1 and a_2 as the atom numbers.

3.3 Interferometry laser system

In the previous sections, we discussed the experimental part of generating the atom sample and detection. We will talk about another essential part of our experiment: the interferometry laser system. This part includes 4 different lasers used during the interferometry. They are:

- Raman lasers used to do the Raman transition
- Bloch lasers used to do the bloch oscillations
- The vertical blow away laser derived from the MOT cooling laser
- The vertical repump laser derived from the MOT repump laser

All the lasers are prepared on the interferometry table (shown in Figure 3.10) and propagate vertically along the vertical tube where we do the atom interferometry (shown in Figure 3.11).

Because the third and fourth lasers are a fraction of the cooling and repump lasers discussed before so in this section, we only talk about the Raman and Bloch lasers.

3.3.1 Laser preparation

Amplifier and double frequency

In order to obtain a high-power laser at 780nm for Raman and Bloch lasers, we use a Muquans laser, an amplifier doubling module seeded with a narrow bandwidth laser at 1560nm.

First, the seed laser is sent to the Erbium-Doped Fiber Amplifier (EDFA)[57]. The target is highly amplified due to stimulated emissions in EDFA. Then this amplified laser is sent to Periodically Poled Lithium Niobate (PPLN) to make Second Harmonic Generation, which gives a laser at 780nm. The whole process is presented in Figure 3.12

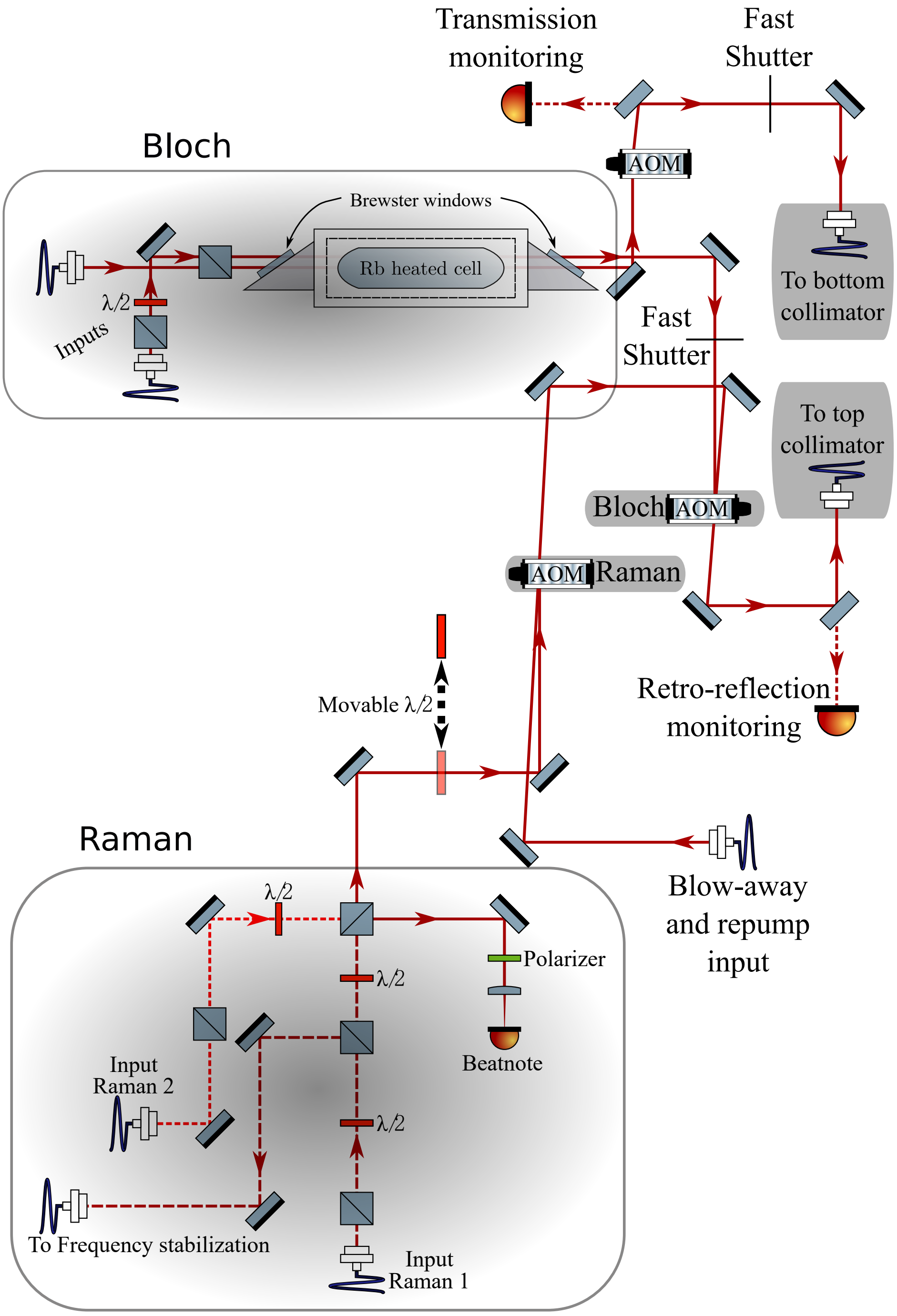

Figure 3.10: Schematic representation of the interferometry table

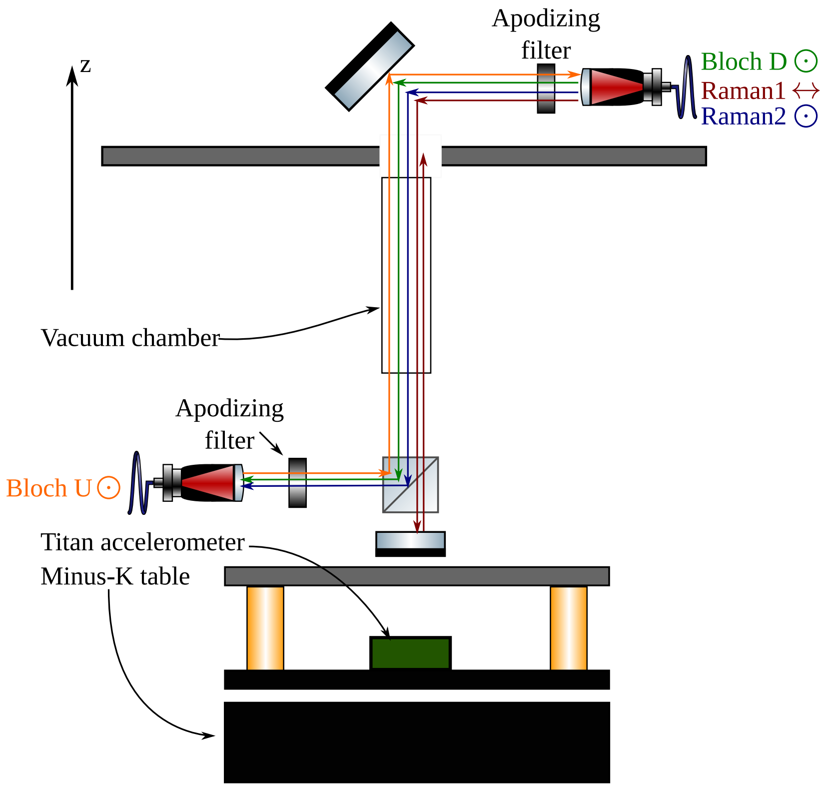

Figure 3.11: Schematic of the interferometry laser path. The two Bloch beams are distinguished by their direction of propagation (Downwards (D) or Upwards (U)). Each Raman beam is indicated next to its input fiber with its corresponding linear polarization axis. One of the Raman is reflected by the reflecting mirror on the vibration table (Minus-K table) to do the counter-propagating Raman transition. This table can reduce the ground vibration noise. It is well explained by the previous PhD student in our group [6].

However, under such a high pump, the ions also have nonnegligible spontaneous emissions during the amplification. Although this process is supposed to be random, there are also a lot of random photons coupled into the fiber and amplified subsequently. This process will produce a significant background shown in Figure 3.12, which we call amplified spontaneous emission (ASE) background.

At the end we can get for each Bloch and Raman laser around 800 mW output power at 780 nm, this power allow us to use a larger beam size to reduce the systematic effects in our experiment. Our next step is using an even more powerful laser for our Bloch and Raman laser, with an expected 2W output power.

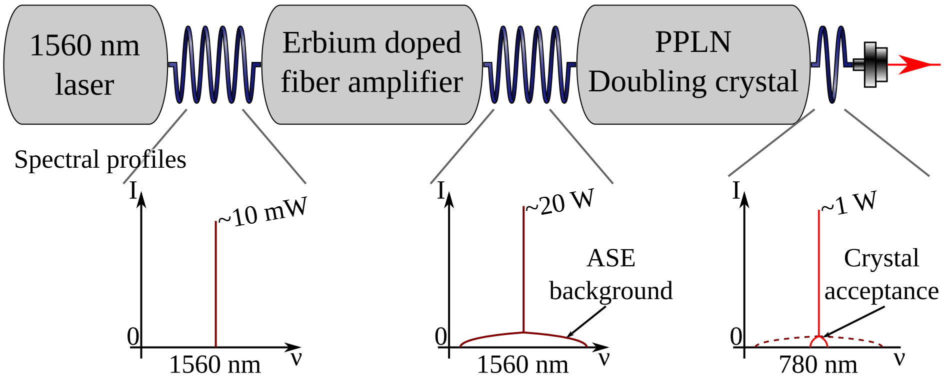

Figure 3.12: The amplifier double frequency module based on a seed laser at 1560nm. The row above presents the amplifier and double frequency part and the row below shows the spectrum and power after each process.

Frequency stabilisation

The h/m measurement is based on the measurement of the recoil velocity of an atom v_{r}, so the stabilization of the Raman and Bloch lasers is essential in our group.

$$v_{\mathrm{r}} = \frac{\hbar k}{m} \tag{3.2}$$

For the last measurement of h/m the Raman and Bloch lasers are locked onto a cavity stabilized on an atomic transition [6] and their frequencies are periodically measured using a frequency comb because the frequecy comb of our team was not enough to lock the laser continuously. By this way we observed a long term variation of the lasers' frequencies by $\sim 10\,\mathrm{kHz}$.

Recently this frequency stabilisation setup is changed and the Raman and Bloch lasers are frequency-locked on reference 1560nm ultra-stable frequency comb with only 2 Hz line width coming from the group of **L. Hilico**.

The seed lasers at 1560nm of Raman and Bloch are separated into two parts at the beginning. Most part is sent to do the EDFA, and the rest 10% power is sent to phase lock with 1560nm frequency comb. The whole system is presented in Figure 3.13.

The 1560 nm ultra-stable laser is split half and half and mixed with the Bloch and Raman laser to get a Beat note signal $\Delta f \sim 15MHz$. The repetition rate of this frequency comb is 200 MHz, so 15 MHz is a good choice, allowing us to know which tooth we are locking on. The Beat note passes through a low pass filter to remove the high-frequency component, and then this signal is sent to the redpitaya where the frequency is measured to create an error signal for each laser. Each signal is completed with a PID controller to individually feedback on the NKT lasers of Raman and Bloch.

This way, we can know precisely the frequency of our Bloch and Raman lasers. And the frequency lock is very stable which can keep locked without jumping for more than two days.

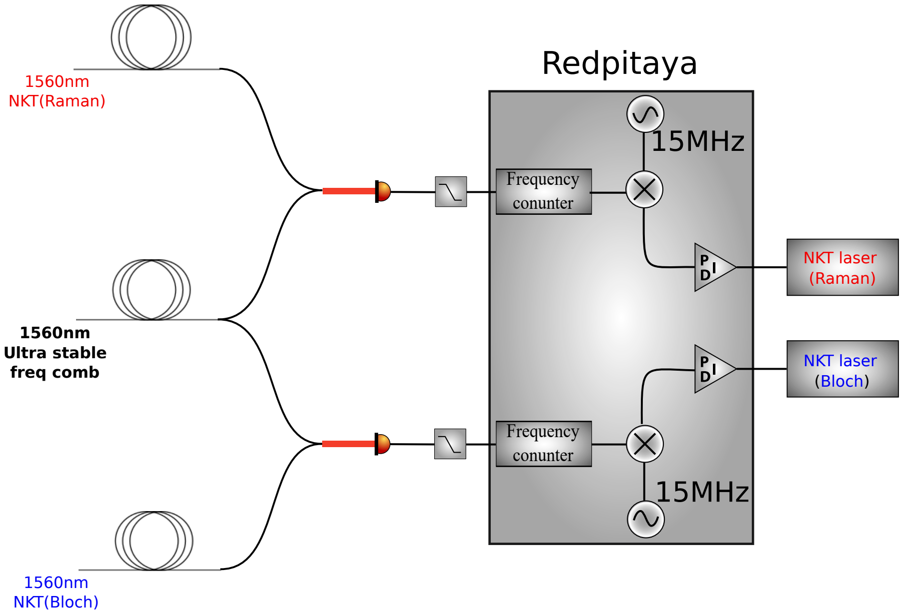

Figure 3.13: The frequency stabilisation system

3.3.2 Raman phase lock

In our experiment, we use two lasers whose frequency difference should be the hyperfine splitting of the two ground states $|1\rangle$ and $|2\rangle$ to perform the two photon Raman transition. Because we want to know precisely the velocity of the atom cloud and follow the atom's motion, we need to have good control of the frequency difference between these two lasers' frequencies. One good way is to phase lock one laser on another.

For our Raman laser system, we have two different sources. One is an NKT laser with a narrow width whose absolute frequency is locked with the previous ultra-stable laser. This laser we call Raman 1. Then we have a second RIO diode laser with a broader width but fast response time that can allow us to do quick frequency modulation on the laser frequency, called Raman 2. We phase lock the RIO laser frequency on the NKT laser. The whole schematic is shown in Figure 3.14

We superpose the beams of Raman 1 and Raman 2 and send a small part of their superposition to a fast photodiode in order to generate a beat note signal with a frequency around 6.834 GHz. After amplification by 35 dB, a small part is used for observation, and most of the signal is directly mixed with a signal $\sim$ 6.514GHz and passes through a low pass filter. We then have only the signal at $\sim$ 320MHz. This signal is divided by 4 and sent to the Phase Comparator device. The synchronization input of the phase comparator is fed with a RedPitaya output set in a direct digital synthesizer. This device outputs a 40 MHz signal which is frequency-doubled. We obtain two 80 MHz signals to implement phase locking. The PLL is then completed with a PID controller to feedback on the RIO diode laser and lock its phase to the first Raman laser. The frequency and phase of the Raman laser is precisely controlled by the DDS in the RedPitaya.

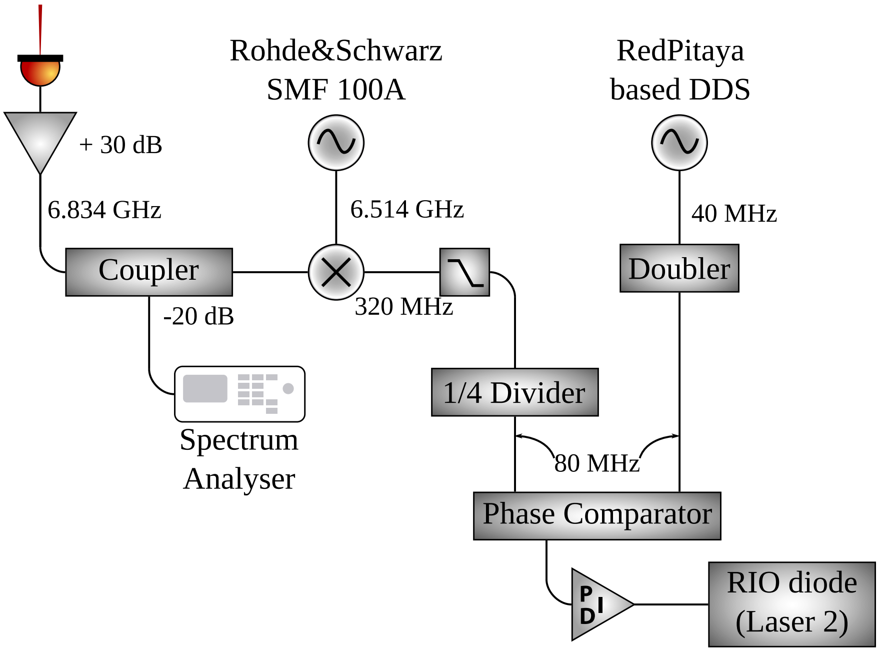

Figure 3.14: Raman Phase Lock Loop (PLL) frequency chain. Extracted from [54]

3.3.3 Bloch lasers preparation

Bloch laser uses the same technology as the Raman to get a high-power at 780 nm. The different is that, in order to generate a stable and moving lattice and implement the Bloch oscillations, it is better to use the same laser source: another narrow width NKT laser. We want an extensive frequency scanning range that can allow us to implement more Bloch oscillations in our experiment. Instead of using double-pass AOM of $780\,\mathrm{nm}$ where power will be lost, we do the frequency tuning before the laser is amplified and double in frequency. The schema is shown on Figure 3.15. In this way, we can have more power.

The frequency of the Bloch frequency is given by:

$$f^{\pm} = 2(f_{\mathrm{NKT}} + f^{0}_{\mathrm{AOM}} \pm \delta f) \tag{3.3}$$

Different from the Raman pulses, whose duration is the order of µs, each Bloch pulse has a duration around several ms. So if there is a part in the ASE background resonant with the atoms, it will induce a spontaneous emission which cause decoherence of our atom cloud. Consequently, it decreases the contrast of the final interferometry signal. To solve this problem, we let the Bloch lasers pass through a heated Rubidium cell before it touches the atom cloud. The preparation schema is presented in Figure 3.16.

Since our Bloch lasers are far blue detuning from the resonant by $\Delta \sim 40GHz$, this heated Rubidium cell will not attenuate this target signal. The reason to heat it is to increase the pressure in the cell so that resonant part in the ASE part will be more absorbed by the atoms.

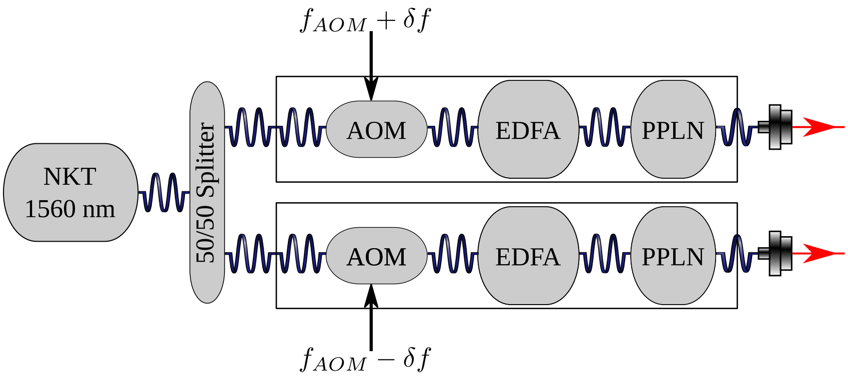

Figure 3.15: The Laser system for the implementation of the Bloch Oscillation process.A single source split into two amplification-doubling modules. The control of frequency of the lasers at 780 nm is achieved by the frequency command of AOMs placed before the amplifiers. We tune the two lasers same absolute value but with opposite sign in order to make sure the sum of these two Bloch frequency is always the same.

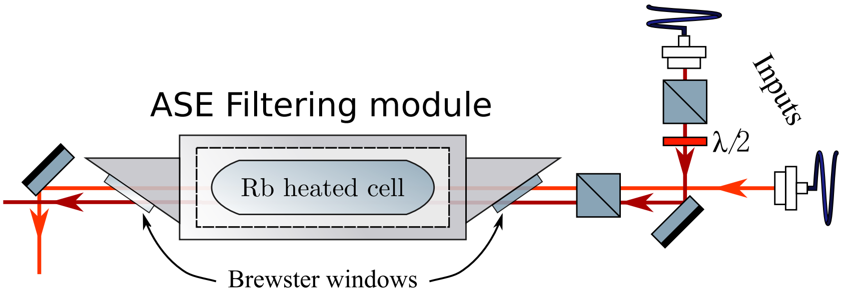

Figure 3.16: Both beam pass through a Rubidium cell for ASE background filtering

Now by those techniques, we can send 1000 photon momenta to the atoms in just $6\,\mathrm{ms}$ with high efficiency of 99.93% per Bloch oscillation.What's more, this atom accelerator gives us an easy way to control the atoms precisely.

Chapter 4

h/m measurement and systematic effects

Matter-wave interferometry has been used to measure with extreme precision and accuracy several physical quantities e.g., gravity, inertial forces and fundamental constants [64, 59, 55] enabling advanced tests of general relativity [11] and quantum electrodynamics [55, 59]. This technology, which has not yet reached its full potential, is also at the heart of large scale or space instruments, that are being built, with the target of significantly improved performance for testing fundamental physics with unprecedented accuracy, detecting gravitational waves [3, 21, 78], exploring exotic forces [39, 38, 9, 10, 44] and mapping the Earth's gravity field from satellites [34, 4, 15]. Furthermore, large momentum atomic beamsplliters by using ultra-cold source [25, 56, 23, 36] is a pontential way to increase the accuracy of atom interferometry.

In the previous chapters, we have shown the main principle of the measurement of the recoil velocity: the combination of the Ramsey Bordé interferometer with the Bloch oscillations technique. This provide us a good way to measure the ratio h/m to determine the fine structure constant α.

In this chapter, we will discuss the experiment process in more detail and show three main systematic effects of our experiment.

4.1 The h/m measurement

4.1.1 Experiment protocol

From the Equation 2.23, we know that the phase difference at the output of the interferometer depends on the velocity change between the two Ramsey sequence. Bloch Oscillations allows us to transfer thousand of recoil velocity v_r to the atoms, but in the experiment, the atoms is also affected by gravity. The more precise expression of the phase difference is :

$$\Delta\phi = T_{\mathrm{R}}\left(\epsilon_{\mathrm{R}}k_{\mathrm{R}}\left(\epsilon_{\mathrm{B}}2N_{\mathrm{B}}\frac{\hbar}{m}k_{\mathrm{B}} - gT_{\mathrm{D}}\right) - \delta\omega\right) \tag{4.1}$$

where $\delta\omega$ is the frequency detuning shift between the two Ramsey sequences and $\epsilon_{\mathrm{R}} = \pm 1$ describe the direction of the Raman beam and $\epsilon_{\mathrm{B}} = \pm 1$ the direction of the acceleration. The exchange of direction of the laser beam and Bloch acceleration are: **Gravity cancellation** and **Systematic effect reduction**. The trajectory of each different laser beam is shown in Figure 4.1.

Gravity cancellation

A simple way to understand it is that the Doppler shift causes the phase shift due to the velocity changes between two Ramsey sequences. From Equation 4.1, we can see that this velocity difference has two contributions: the shift controlled by the Bloch oscillations and the gravity. By combining the two Bloch acceleration directions, we can eliminate the impact of gravity and obtains the h/m ratio:

$$\frac{h}{m} = \frac{\delta\omega(\epsilon_B = 1) - \delta\omega(\epsilon_B = -1)}{2N_B k_R k_B} \tag{4.2}$$

In this way, we can remove the effect of gravity. But if we do the sum of the two Bloch acceleration directions, we can also extract the gravity precisely.

Systematic effect reduction

If everything in our experiment is ideal, then we only need to remove the gravity to measure the h/m ratio. But we explained in chapter 2 that the phase shift also depends on the atomic internal energy difference. Of course, this phase is zero if this energy difference is constant over the entire interferometer. The Bloch acceleration makes an immediate velocity kick in $6\,\mathrm{ms}$ reaches $\sim\ 6m/s$. This abrupt and big velocity change leads to a quite different trajectory for different Bloch directions. Consequently, the magnetic field inhomogeneity and light shift can induce an additional phase shift.

- $\vec{B}$ **inhomogeneity:** Even with the so-called magnetic insensitive state $m_F = 0$, there is still 2nd order Zeeman that should be taken into account.

  $$\delta\omega_{2nd} = \pm\frac{KB(z)^2}{2} \tag{4.3}$$

  where $K = 575.15\,\mathrm{Hz/G}$, and $\delta\omega_{2nd}$ is positive if atom is in $|F = 1, m_F = 0\rangle$ or negative if atom is in $|F = 2, m_F = 0\rangle$. So if the spatial distribution of the magnetic field is not inhomogeneous, this will introduce a big shift. But as we showed in Figure 3.3, the magnetic field in the tube is very stable. And by using a precise computation of the atomic trajectories for each interferometer and the measured magnetic field along the interferometer area, we obtain a relative correction on h/m that is below 10^{-12} (shown in Figure 4.6).

- **Light shift:** A big velocity shift between the two Ramsey sequence will cause a two photon light shift difference (More details is shown in [54]). At the end, a more explicit expression of the phase shift is

$$\Delta\phi = T_{\mathrm{R}}\left(\epsilon_{\mathrm{R}}k_{\mathrm{R}}\left(\epsilon_{\mathrm{B}}2N_{\mathrm{B}}\frac{\hbar}{m}k_{\mathrm{B}} - gT_{\mathrm{D}}\right) - \delta\omega\right) + \delta\phi(\epsilon_{\mathrm{B}}) \tag{4.4}$$

Where $\delta\phi(\epsilon_{\mathrm{B}})$ is the phase shift depending on the direction of Bloch oscillations. The technique to reduce the phase shift is to invert the Raman direction and combine the two results.

$$\frac{h}{m} = \frac{\delta\omega(\epsilon_R = 1) - \delta\omega(\epsilon_R = -1)}{2N_B k_R k_B} \tag{4.5}$$

So in our experiment, for a determination of the ratio h/m we have four different configurations of ϵ_R, ϵ_B. Combining these four results, we find out:

$$\frac{h}{m} = \frac{1}{4N_B k_B k_R}\sum |\delta\omega_{\epsilon_{\mathrm{R}},\epsilon_{\mathrm{B}}}| \tag{4.6}$$

4.1.2 Experiment sequence

Our experiment begins with Molasses with a temperature $4\,\mu\mathrm{K}$. To transfer atoms in the interferometer area, we use an atomic elevator that consists of two Bloch oscillations pulses. One is to accelerate the atoms, and the other is to decelerate the atoms. By adjusting the parameters of the elevator (number of Bloch oscillations and delay), we can precisely control the initial position z_0 and velocity v_0 of the cloud when it enters the interferometer. Between the two Bloch oscillations pulses of the elevator, we apply a pair of Raman π pulses with a blow-away pulse. With this sequence, atoms are prepared in the magnetically insensitive state $\mathrm{m_F} = 0$, and by controlling the intensity and duration of the first Raman π pulse, we set the width of the vertical velocity distribution of the atomic cloud. These steps are the preparation sequence before our atom interferometer. After the preparation sequence, $500\,000$ atoms remain in the cloud.

The interferometer consists of four $\pi/2$ Raman pulses of the same duration arranged in two identical Ramsey sequences with time delay $\mathrm{T_R}$ separated by a duration T. The Bloch oscillation pulse is applied between the two Ramsey sequences. The pulse sequence is shown in the Figure 4.1**c**. All the interferometer sequence happens in the interferometer area where the magnetic field is well controlled. This is shown in chapter 3. After the interferometer finishes, we let the atom free fall into the time of flight detection part so that we can measure the ratio $\mathrm{N_2}/(\mathrm{N_1}+\mathrm{N_2})$. Then we repeat this sequence time by time. Each time we randomly change the $\delta\omega$ between the two Ramsey sequences to get the spectra.

As we discussed before, we have to measure four different spectra by inverting the direction of Raman lasers and Bloch acceleration to do gravity cancellation and systematic effect reduction. These points are sampled randomly to avoid systematic effects due to potential drifts during the data collection. We use a sinusoidal function to fit the fringes and extract the estimations of the $\delta\omega$. All the results are shown in Figure 4.2.

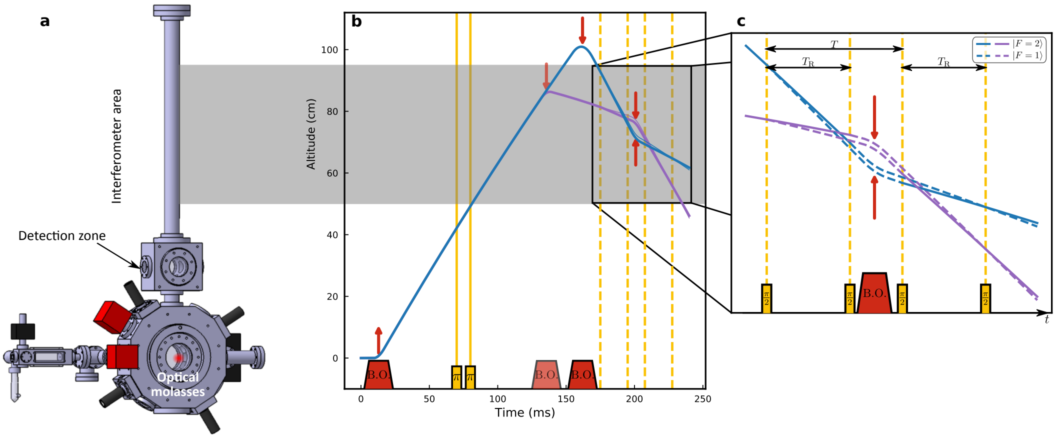

Figure 4.1: **a.** Design of the vacuum chamber, the detection zone and atom interferometer area - a 70 cm long magnetically shielded tube. **b.**The pulse sequence of the experiment and atom trajectory changes with the time. **c.** The trajectory of atoms with different Bloch acceleration direction.

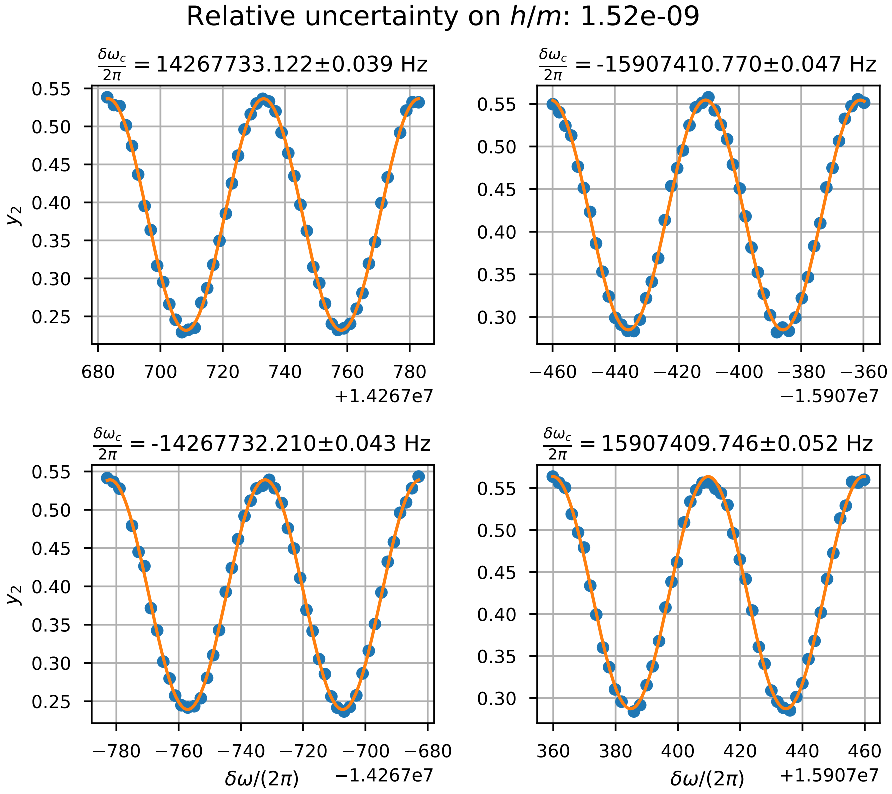

Figure 4.2: Typical spectra set for h/m determination. The direction of Raman ϵ_R and Bloch ϵ_B are shown in each figure. The blue points are the experimental data. The uncertainty on the central fringe is deduced from the fitting procedure, each of them is around 0.05 Hz. From the combination of the four spectra, we deduce a value of h/m with an estimated relative uncertainty of 1.5×10^{-9}.

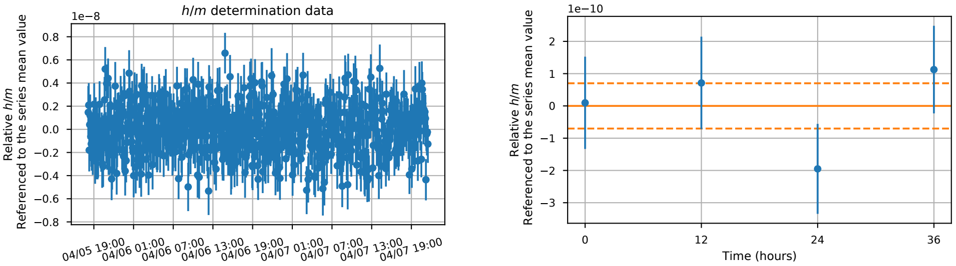

Figure 4.3: Left : Set of h/m determinations (678 points) taken over 48 hours. Each point correspond to ~ 5 minutes of integration. Right : Four integrated h/m values. Each points corresponds to 12h of integration.

4.1.3 The result of the measurement

For each sequence, we can get a typical relative uncertainty around 1.5×10^{-9} on h/m in around 5 minutes. In order to know the statistical uncertainty, we keep the experiment running for a weekend. The raw data is shown in Figure 4.3. This data set is taken at $\mathrm{T_R} = 20\mathrm{ms}$ and 500 Bloch oscillations. Here we can see our experiment is very stable for 48 hours.

We also plot the Allan deviation of the data set to study the stability of this experiment (Figure 4.4). We can fit this deviation with a $\sigma = \frac{\beta}{\sqrt{T}}$ function, β is the slope of the linear fitting curve in the log-log scale. Our slope is $6 \times 10^{-10}\ \sqrt{\mathrm{h}}$. This way, we can estimate that the relative statistical uncertainty over 48h is 8.5×10^{-11}.

Thank to our experiment sensitivity on h/m, we have run 8 different configurations whose details are shown in the **Table**4.1 and their final experimental results are presented in Figure 4.5. At the end we extract the final statistical uncertainty of the h/m ratio, which is around 4.8×10^{-11}. It has therefore a contribution to the determination of α relative uncertainty of 2.4×10^{-11}

Then we studied the systematic effects in our experiment, all the relative uncertainty contributions are shown in our error budget Figure 4.6.

Subsequently, we are going to discuss the three biggest systematic effects in our experiment: **Phase shifts in Raman phase lock loop**, **wavefront distortion**, **Residual Raman Phase shift**.

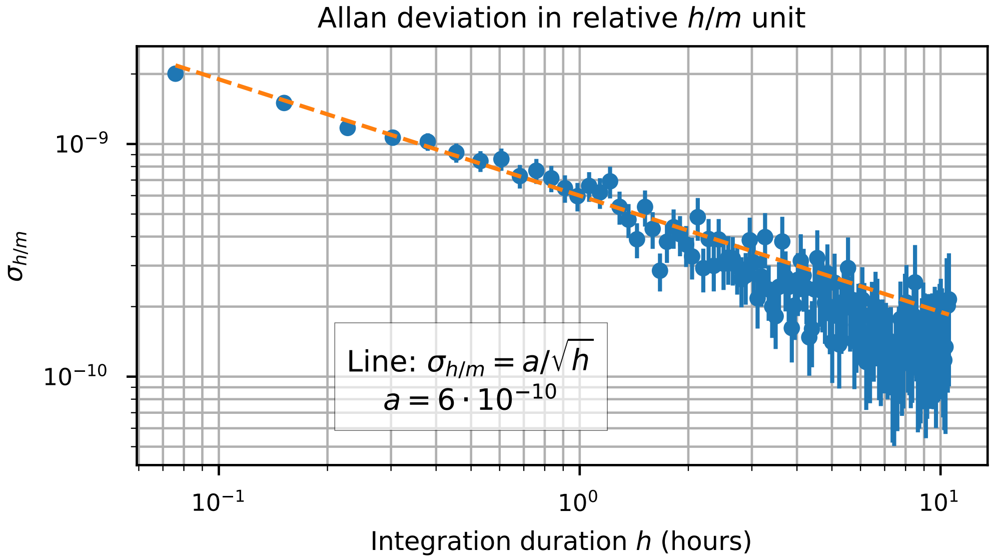

Figure 4.4: Comparison between the data Allan deviation and the expected behavior in the case of a white noise induced data distribution.

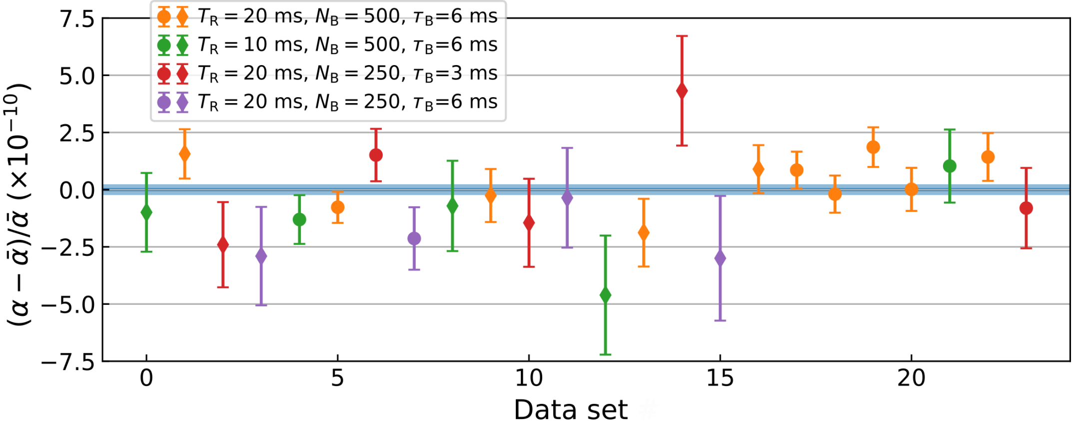

Figure 4.5: Collection of h/m determinations with 8 different configurations mentioned in **Table**4.1. The circles and diamonds correspond to two different laser intensities

Configuration		Ⓐ	Ⓑ	Ⓒ	Ⓓ	
T_R		20	10	20	20	ms
N_B		500	500	250	250	BOs
τ_{digital}		12	12	24	24	μs
t_{delay}		32.9				ms
$t_{\text{elev,1}}$		9				ms
$N_{\text{elev,1}}$		+650				BOs
$t_{\text{prep,1}}$		110				ms
$\tau_{\text{prep,1}}$		189				μs
$t_{\text{prep,2}}$		120				ms
$\tau_{\text{prep,2}}$		63				μs
$t_{\text{elev,2}}$	Spectra 1, 2	154.910				ms
	Spectra 3, 4	131.528	131.946	137.492	136.984	
$N_{\text{elev,2}}$	Spectra 1, 2	-1185	-1010	-1185	-1185	BOs
	Spectra 3, 4	-635	-515	-735	-735	
$t_{\text{interf.}}$		175				ms
$\tau_{\text{interf.}}$	Raman power: Low	80				μs
	Raman power: High	35				
$t_{\text{acc.}}$		197.9				ms

Table 4.1: Parameters used for the data collection for the different configurations and spectra. The times are indicated with respect to the release of the atomic cloud from the optical molasses.

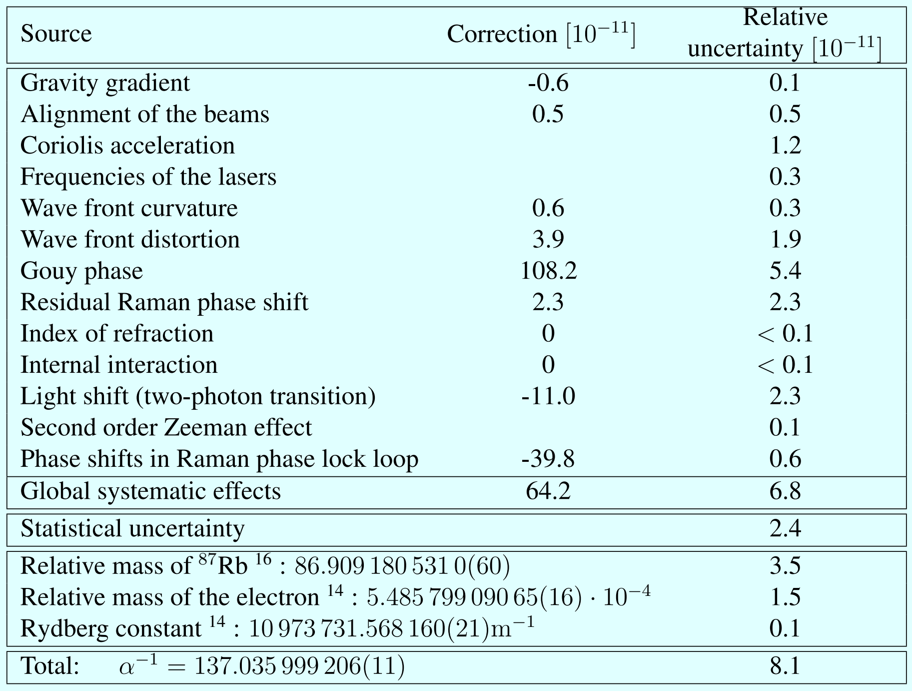

Source	Correction $[10^{-11}]$	Relative uncertainty $[10^{-11}]$
Gravity gradient	-0.6	0.1
Alignment of the beams	0.5	0.5
Coriolis acceleration		1.2
Frequencies of the lasers		0.3
Wave front curvature	0.6	0.3
Wave front distortion	3.9	1.9
Gouy phase	108.2	5.4
Residual Raman phase shift	2.3	2.3
Index of refraction	0	< 0.1
Internal interaction	0	< 0.1
Light shift (two-photon transition)	-11.0	2.3
Second order Zeeman effect		0.1
Phase shifts in Raman phase lock loop	-39.8	0.6
Global systematic effects	64.2	6.8
Statistical uncertainty		2.4
Relative mass of ^{87}Rb [16] : $86.909\,180\,531\,0(60)$		3.5
Relative mass of the electron [14] : $5.485\,799\,090\,65(16) \cdot 10^{-4}$		1.5
Rydberg constant [14] : $10\,973\,731.568\,160(21)\text{m}^{-1}$		0.1
Total: $\alpha^{-1} = 137.035\,999\,206(11)$		8.1

Figure 4.6: The error budget of our final determination of α

4.2 Systematic effects

4.2.1 Phase shifts in Raman phase lock loop

Theoretical principle

As we have discussed before (see in subsection 3.3.2), the Raman phase lock loop (PLL) relies on the beat note between the frequency difference of the Raman lasers measured on a photodiode and a microwave generator. We use a phase comparator seed with the RF signal $\omega_{\mathrm{RF}}(t)$ synthesized in a Redpitaya module. This beat note frequency is

$$\begin{aligned}\omega_{\mathrm{BN}} &= \omega_{\mathrm{MW}} + 8\omega_{\mathrm{RF}} \\ &= \omega_{\mathrm{HFS}} + \epsilon_{\mathrm{R}} k_{\mathrm{R}} v(t) + \frac{\hbar k_{\mathrm{R}}^2}{2m} \end{aligned} \tag{4.7}$$

The second part $\epsilon_{\mathrm{R}} k_{\mathrm{R}} v(t)$ is the dynamical frequency change in order to compensate for gravity and frequency jump caused by the Bloch oscillations. The frequency ramp is shown in Figure 4.7. This frequency always changes with time, and because the beat note signals pass through filters and it is the source of this systematic effect. Let us models this with a simple low pass filter whose transfer function is

$$H(\omega) = \frac{1}{1 + i\,(\omega/\omega_{\mathrm{c}})} \tag{4.8}$$

From the Equation 4.8, we can calculate that passing through this low pass filter will introduce a phase shift.

$$\delta\phi(\omega) = -\arctan(\frac{\omega}{\omega_c}) \tag{4.9}$$

Combining the four Raman pulses, at the end this will result in a total phase shift.

$$\delta\phi_{\mathrm{tot}} = \delta\phi(\omega_1) - \delta\phi(\omega_2) - \delta\phi(\omega_3) + \delta\phi(\omega_4) \tag{4.10}$$

The two Ramsey sequences have the same time delay $T_{\mathrm{R}} = 20\,\mathrm{ms}$ in our normal experiment. The frequency sweep rate for the gravity is $25\,\mathrm{kHz/ms}$. At the end the frequency difference $\delta f \sim 500\,\mathrm{kHz}$ which is much smaller than the Raman frequency $f_i \sim 20MHz$. So we can simplify this formula:

$$\begin{aligned}\delta\phi_{\mathrm{tot}} &= \left(\left.\frac{d\delta\phi}{d\omega}\right|_{\omega_3} - \left.\frac{d\delta\phi}{d\omega}\right|_{\omega_1} \right)\delta\omega \\ &= \left(\frac{1}{1 + (\omega_1/\omega_c)^2} - \frac{1}{1 + (\omega_3/\omega_c)^2} \right)\frac{\delta\omega}{\omega_c} \end{aligned} \tag{4.11}$$

So one way to reduce this effect is to make the absolute value of ω_1 and ω_3 the same or close as possible. So we change the Raman frequency sweep configuration from an

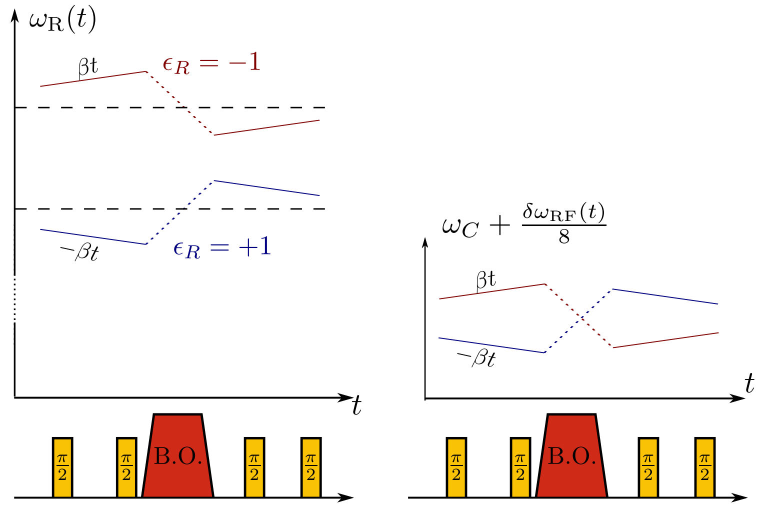

Figure 4.7: Frequency ramps performed by the RedPitaya generator for $\epsilon_B = 1$. Left: ω_{MW} is constant and the ω_{RF} frequency ramp is not symmetric. Right: ω_{MW} is changed when inverting the Raman direction ϵ_R and the ω_{RF} frequency ramp is symmetric.

unsymmetric configuration to a symmetric configuration where we can reduce this phase shift.

$$\omega_1(\epsilon_R) = \omega_4(-\epsilon_R) \tag{4.12}$$
$$\omega_2(\epsilon_R) = \omega_3(-\epsilon_R) \tag{4.13}$$

This condition is achieved by changing the frequency of the microwave ω_{MW} with the Raman direction ϵ_R. Experimentally, we ensure that the offset value of ω_{RF} is always the same. Due to the Bloch oscillations, the atom velocity will significantly change in a short time so that there is a frequency jump for the reference frequency ramp. This modification of ω_{RF} , or the frequency jump, is placed $\sim 250\,\mu s$ before we put the third pulse. We checked that no modification of the measured phase shift occurred by reducing this duration by $100\,\mu s$.

Experimental measurement

In our experiment, we make an independent measurement of the phase of the beat note signal and study how this effect will affect our final result. The set up is shown in Figure 4.8. The beat note signal is lowered in frequency by mixing it with another microwave synthesizer. We then record this signal by a 100-MHz-bandwidth oscilloscope (Tektronix DPO 3014) and demodulate each pulse by computing its two quadratures with a numerically computed signal. The time base of the oscilloscope was calibrated by analyzing the signal of 10-MHz reference coming from **SYRTE**.

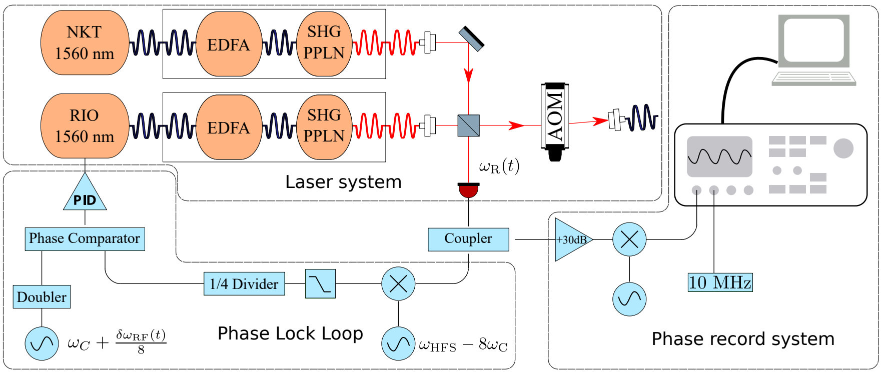

Figure 4.8: Top left: laser arrangement used to extract a beat note between the two lasers. Bottom left: radio-frequency chain for the phase lock. Right: setup used for the measurement of the phase between the two lasers. Figure extracted from [54]

The steps of this phase analysis consists of two parts: **Time scale calibration** and **Phase measurement**

Time scale calibration:

- The 10-MHz reference signal is sent to one channel of the oscilloscope, $s_{\text{ref}} = \text{A}\cos(\omega_{\text{ref}} t_{\text{osc}} + \phi_0)$ where the t_{osc} is the real time scale on the oscilloscope that we need to figure out.
- We record this oscilloscope signal and mix it with digital signals in quadratures at same frequency with time step t_{digital}, we have the two signals

$$s1 = \frac{1}{2}\left(\cos\left(\omega_{\text{ref}}\left(t_{\text{osc}} - t_{\text{digital}} + \phi_0\right)\right) + \cos\left(\omega_{\text{ref}}\left(t_{\text{osc}} + t_{\text{digital}} + \phi_0\right)\right)\right) \quad (4.14)$$

$$s2 = \frac{1}{2}\left(\sin\left(\omega_{\text{ref}}\left(-t_{\text{osc}} + t_{\text{digital}} + \phi_0\right)\right) + \sin\left(\omega_{\text{ref}}\left(t_{\text{osc}} + t_{\text{digital}} + \phi_0\right)\right)\right) \quad (4.15)$$

- We then remove the high frequency part by averaging the signal:$q_i(t) = \langle s_i \rangle$. We get[1]

$$\omega_{ref}(\mathrm{t}_{\text{osc}} - \mathrm{t}_{\text{digital}} + \phi_0) = \arctan(-q_2(t), q_1(t)) \quad (4.16)$$

- Since the signals are digitalized, we write $t_{\text{osc}} = j dt_{\text{osc}}$ (resp. digital), where j is the index of the data. Then we get the true time scale dt_{osc}:

$$\arctan(-q_2, q_1)(j) = \omega_{\text{ref}}(dt_{\text{osc}} - dt_{\text{digital}})j + \phi_0 \quad (4.17)$$

Phase measurement

---

[1] We use $\arctan(y, x)$ for the notation of the arc tangent of y/x choosing the quadrant correctly

- The beat note signal is sent to the oscilloscope. We only record the signal during the pulse duration s_i^{BN}, where the subscripts refer to the pulse order.

- The record signal is digitally mixed with two digital signals in quadratures with the same frequency ramp and the time scale by the time scale calibration. The β is the sweep rate to compensate the gravity.

$$\begin{aligned} s1 &= s_i^{\text{BN}} \cdot \left(\cos\left(\omega_{\text{i}}(t-t_{\text{i}}) + \beta \cdot (t-t_{\text{i}})^2/2\right)\right) && (4.18) \\ s2 &= s_i^{\text{BN}} \cdot \left(\sin\left(\omega_{\text{i}}(t-t_{\text{i}}) + \beta \cdot (t-t_{\text{i}})^2/2\right)\right) && (4.19) \end{aligned}$$

- We remove the high frequency part by averaging the signal: $q_i(t) = \left\langle s_{\text{ref}}(t) \cdot s_{\text{dig,i}}(t) \right\rangle$ and use the $\arctan(-q_2, q_1)$ to get the phase ϕ_i of this pulse.

- After we extracted the phase of each pulse, we use the formula $\phi_{\text{pll}} = \phi_1 - \phi_2 - \phi_3 + \phi_4$ to deduce the effect on h/m by

$$\frac{h}{m} = \frac{\phi_{\text{pll}}}{4N_B k_B k_R} \tag{4.20}$$

Result

We confirmed that the oscilloscope did not induce a bias by reducing its bandwidth to 20 MHz, and we did not detect shifts on h/m at the level of 0.01 ppb.

We studied the relationship between the phase of the beat note and the interferometric measurement in the following way: using 600 determinations of h/m performed continuously over about 60 h, we divided the set into six quantiles sorted by the beat note phase. For each quantile, we averaged this phase and the interferometric phase(see in Figure 4.9).

At the end we found a correction on h/m with $(-82.1 \pm 1.2) \times 10^{-11}$ with number of Bloch oscillation $N_B = 500$. In Figure 4.9 it shows the relationship between these two quantities, and their fluctuations are identical (slope of 1). In the end, we calculate that the effect creates a shift on α

$$\frac{\Delta\alpha}{\alpha} = (-39.8 \pm 0.6) \times 10^{-11} \tag{4.21}$$

4.2.2 Beam Profile

Gouy Phase

Another significant systematic effect comes from the beam profile. We do not have a perfect plan wave, but we have in the lab a beam that is approximately Gaussian:

$$\vec{E}(r,z) = E_0 \frac{w_0}{w(z)} \exp\left(\frac{-r^2}{w(z)^2}\right) \exp\left(-i\left(kz + k\frac{r^2}{2R(z)} - \phi(z)\right)\right) \tag{4.22}$$

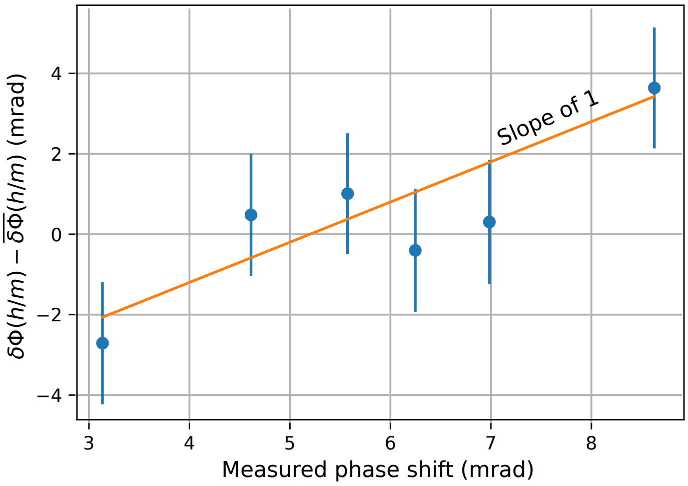

Figure 4.9: Average interferometric phase with respect to the average correction deduced from the phase of the beat note.

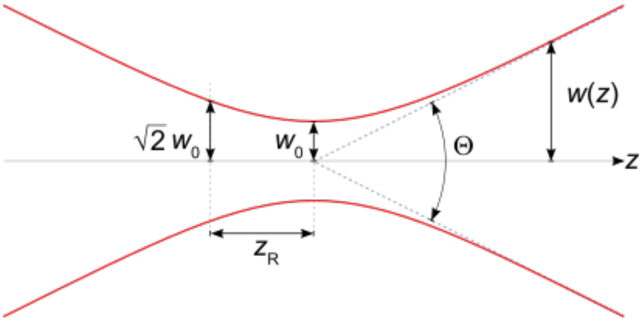

Figure 4.10: Schematic of a Gaussian beam. Extracted from Wikipedia

where r is the radial distance from the center axis of the beam, $w(z)$ is the $1/\mathrm{e}$ radius at position z, $z_R = \pi w_0^2/\lambda$ is called the Rayleigh length, $R(z) = z(1 + (z_R/z)^2)$ is the radius of curvature of the beam's wavefront at position z, $\phi(z) = \arctan(z/z_R)$ is the Gouy phase.

The effective wave vector is the derivative of the spatial phase $\mathrm{k_{eff}} = -\mathrm{i}\frac{\partial\phi}{\partial \mathrm{z}}$[24]. Then there is a shift :

$$\delta k = k_{\text{eff}} - k = -\frac{2}{kw(z)^2}\left(1 - \frac{r^2}{R(z)^2}\left(1 - \left(\frac{z}{z_R}\right)^2\right)\right) \tag{4.23}$$

The first part is the effect of the Gouy phase. The second part is due to the variation of the transverse spatial phase. In our experiment, the waist w_0 is around $5\,\mathrm{mm}$ which gives us $z_R \sim 40\,\mathrm{km}$ and $R \sim 1\,\mathrm{km}$ so that the second part in Equation 4.23 is negligible compare to the first part. So the main effect comes from the Gouy phase. We put the beam profile measured in our lab into our Monte Carlo simulation, and we get an estimation of the correction on α is

$$\frac{\Delta\alpha}{\alpha} = (108.2 \pm 5.4) \times 10^{-11}$$

Wavefront distortion

In 2018 the group found a very interesting phenomena: if we reduce the efficiency of the Bloch oscillation by decreasing the Bloch laser power, we get a smaller value of h/m. This effect causes an order of 2×10^{-8} relative shift on h/m, for a 25% reduction of the Bloch oscillation efficiency.

This effect was then interpreted as the wave-front distortion[13]. We already knew that the wave vector we measured in the experiment had a shift due to the beam profile. In fact, this effective wave vector can be rewritten in a formula as the sum of the deviation of the transverse intensity and phase:

$$\delta \mathrm{k} = -\frac{1}{2\mathrm{k}}|\tilde{\nabla}_{\perp}\phi|^2 + \frac{1}{2\mathrm{k}}\frac{\Delta_{\perp}\mathrm{A}}{\mathrm{A}} \tag{4.24}$$

where ϕ is the spatial phase of a gaussian beam shown in Equation 4.22 and A is the local amplitude of the field. This equation makes this phenomenon more interesting: we always think that if we can have a plan wave used in the experiment instead of a gaussian beam, the correction due to the beam profile will be canceled. But Equation 4.24 tells us a different but interesting thing: even if we can have a Gaussian beam with an infinitely large waist that is infinitely close to a plan wave. But as the phase noise or amplitude noise will still exist, so Equation 4.24 is non zero.

We should first note that the spatial phase and amplitude fluctuations are mixed during propagation. Even a wave-front distortion caused by optics will appear as amplitude fluctuations after propagation. Furthermore, the relative fluctuations of the amplitude and phase fluctuation are in the same order. As in the Equation 4.24 the first part is square of relative phase fluctuation, so the term due to the phase noise is negligible compared to the term due to the local amplitude noise. This is very interesting because when we consider the effect due to the beam profile, we always think the dominant part is due to the diffraction of the wave vector, which comes from the spatial phase fluctuation. However, in fact the dominant part is the amplitude fluctuation of the field. This will be proved in the next part.

The amplitude fluctuation depends on the amplitude variations, which induce negative corrections to the wave vector at local intensity maxima and positive corrections at local intensity minima. In contrast, the first term, which is due to the spatial phase fluctuation can only cause a negative correction.

At the output of the interferometer, we are sensitive to the average $\langle\delta k\rangle$ over the whole atom cloud that survives the Bloch pulses and the efficiency of Bloch Oscillations depends on the local laser intensity. We can get this effective wave vector correction:

$$\langle\delta k\rangle = \frac{\langle\delta k(\vec{r})P(I(\vec{r}))\rangle}{\langle P(I(\vec{r}))\rangle} \tag{4.25}$$

The systematic effect is due to the correlation between $\delta k(\vec{r})$ and the survival probability $P(I(\vec{r}))$ after all Bloch oscillations.

Assuming that we are not limited by spontaneous emission, the efficiency increases with the Bloch laser power. This allows us to select where the surviving atoms are and test this systematic effect.

The experiment check:

Here I will briefly describe the experimental results that was obtained and validate this approach.

The recoil measurements are repeated by scanning the intensity of the Bloch beams each time to extract the efficiency of Bloch oscillation by measuring the fraction of atoms at the output of the atom interferometer. The Ramsey-Bordé interferometer consists of four Raman $\pi/2$ pulses. Between the first and second pair of pulses, BOs are used to accelerate atoms. Here we have two experiments to test this extra recoil velocity in the high and low local intensity regions.

Because the Bloch oscillations efficiency depends sharply on the intensity of the laser, if we do the typical experiment (sequence shown in Figure 4.11(a)) then atoms that survive at the end are the atoms in the higher intensity regions. We expect a negative recoil velocity correction. Because the phase noise can also create a negative correction, in order to confirm that this effect is coming from the amplitude fluctuation, we add an aperture of diameter 3 mm on the path of one of the Bloch beams to amplify the intensity fluctuations. The experiment results are shown with the theoretical calculation based on the Equation 4.25 in Figure 4.11.

We can see that the experimental results agree with the theoretical calculation values. And it can prove that this effect comes from the amplitude fluctuation but not the phase fluctuation. But what is more interesting is that Equation 4.24 predicts that a positive correction is possible if the surviving atoms are in the weaker intensity area.

So subsequently, another experiment was done. Unlike the standard experiment, this time a small Bloch oscillation pulse with low power was used to remove the atoms in the high-intensity area so that the remaining atoms are all in the low-intensity region, see Figure 4.12.

In ths experiment, a positive correction on the recoil velocity was observed, which again proves that this effect comes from the amplitude fluctuation of the field.

Effect on the final determination of α

The previous work on the observation of extra recoil velocity shows a new systematic effect in our experiment: the wavefront distortion. From the previous study, we know that this effect is highly related to the beam amplitude noise and the efficiency of Bloch oscillation, or the power of Bloch beams.

We need to know the beam profile to estimate and mitigate this effect in our h/m experiment. We use a CCD camera (*IDS UI-5340CP-NIR-GL*) to study the beam profile. And we found that if we let the beam propagate for a long distance, the wavefront will be smoother

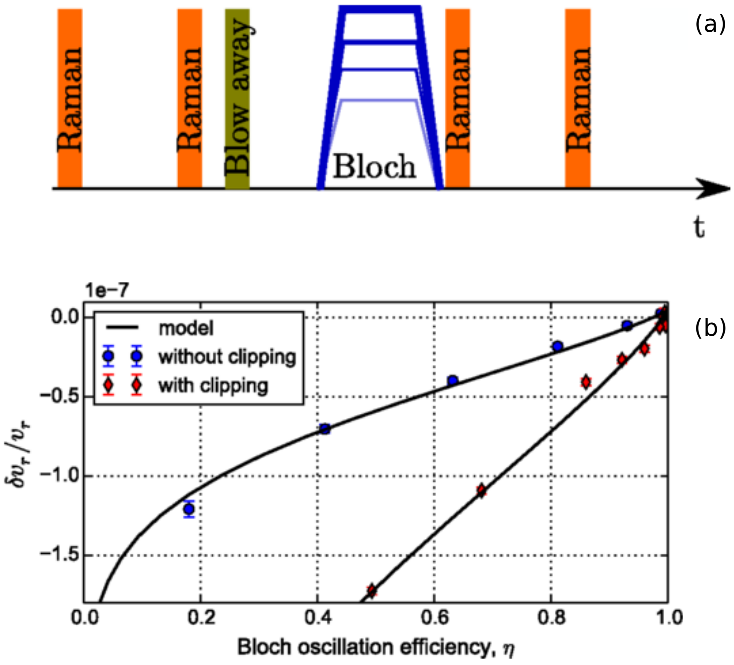

Figure 4.11: **a**: Temporal sequence for the measurement of the recoil velocity. The intensity of the Bloch beams is reduced in order to select atoms in the high intensity region. **b**:The relative recoil velocity variation $\delta\nu_r/v_r$ as a function of efficiency η. Dots correspond to experimental data which are obtained in two cases: with and without clipping one of the Bloch beams. The deviation in the momentum from the usual wave front is larger when the beam is clipped due to amplified fluctuations. Line: calculated correction due to the change in momentum $\hbar\delta k/m$ as a function of the efficiency of Bloch Oscillations. Extracted from [13].

(see in Figure 4.13). So in order to reduce the intensity, we let the laser freely propagate for $3\,\mathrm{m}$ before it touches the atoms.

Our team has developed a Monte-Carlo simulation to study this effect with the beam profile acquired by the CCD camera at the given position where the atoms meet the Bloch beam. The results are shown in Figure 4.14. From this picture, we conclude that the lower the Bloch laser power, the bigger the shift. So in the experiment, we put the maximum power on the Bloch lasers to reduce this effect. At the end, by using the Monte-Carlo simulation, we have a calculated correction due to the wave distortion is

$$\frac{\Delta\alpha}{\alpha} = (3.9 \pm 1.9) \times 10^{-11}$$

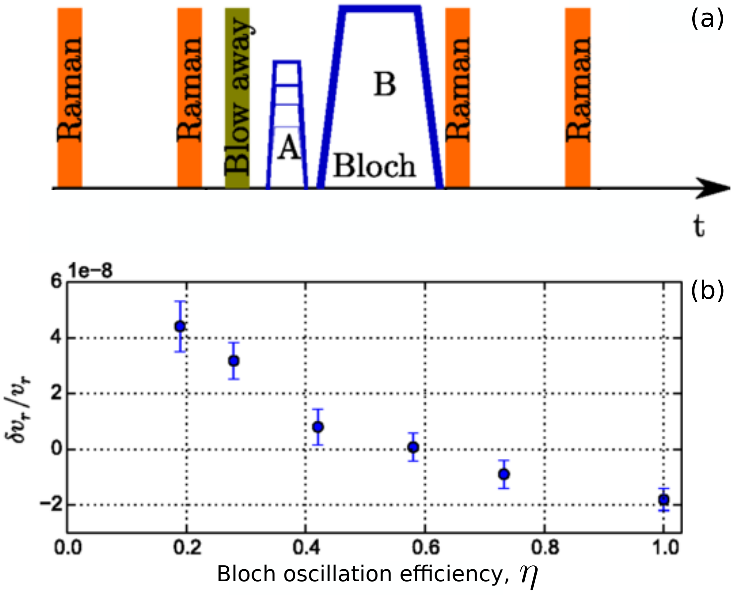

Figure 4.12: **a**: Temporal sequence for the measurement of the recoil velocity. the BO pulse A is used to remove atoms in the high intensity region and the pulse B at fixed intensity is used to the measurement of the recoil velocity. **b**:Measurement of the relative recoil in a distorted field obtained by removing atoms in the high intensity regions of the Bloch beams.

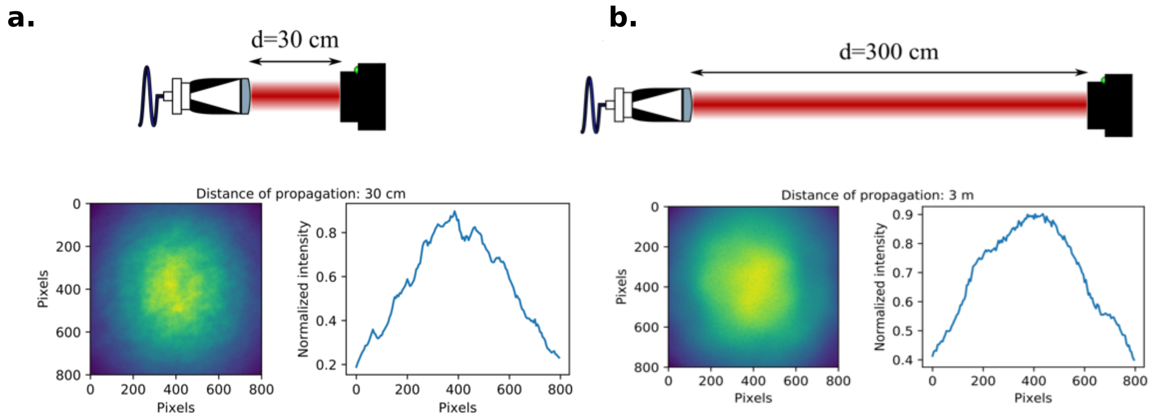

Figure 4.13: Beam profile acquired from CCD camera and cross section of the center of the beam. (a): Free propagation 30 cm. (b): Free propagation 3 m

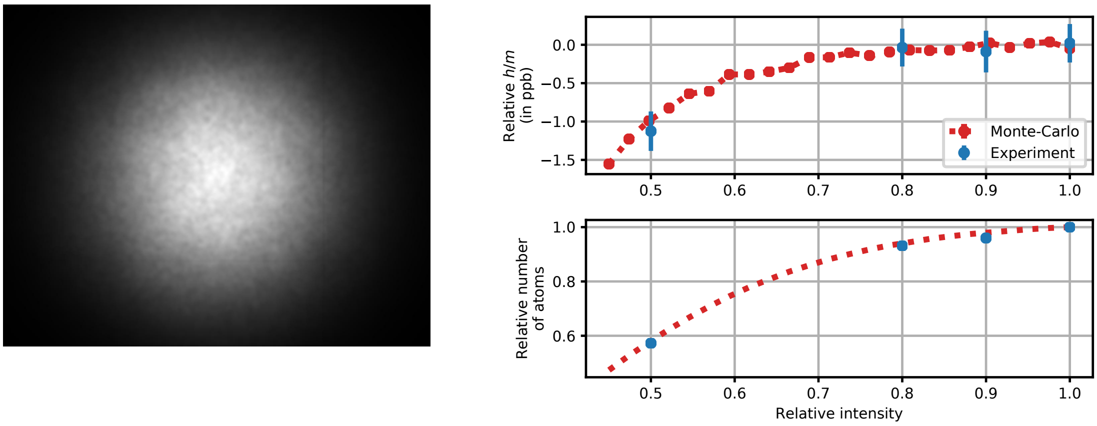

Figure 4.14: Left: Image of the beam profile obtained with a CCD camera. Right: Characterisation of the short scale noise on the beam intensity. The intensity of the laser used for Bloch oscillation is reduced, leading to losses of atoms in the experiment (bottom graph). This induces a systematic effects on the recoil measurement (upper graph).

4.2.3 Residual Raman phase shift

In the last part, we have discussed the systematic effect of the technique and beam profile. Now we will talk about the effect of the internal energy shift due to the interaction with the field, which we call it **light shift**.

In chapter 2, we know that the two-photon transition couples the two hyperfine structures $|1\rangle$ and $|2\rangle$. The off-diagonal part of evolution operator Equation 2.14 correspond the change of the state. After the transition, the atom will get the phase off-diagonal part is the phase of the laser. This gives us a way to get information about atoms by controlling the phase of the laser.

But what is interesting is that the diagonal part of Equation 2.14 is not a real number but a complex number. It depends on Ω and δ_{tot}. This means even non-diffracted atoms will get a phase due to the applied laser field. The phases are:

$$\delta\phi_{1\to1} = \arg\left(\langle 1|U(\tau)|1\rangle\right) = -\arctan\left(\frac{\delta_{\text{tot}}}{\Omega_{\text{eff}}}\tan\left(\frac{\Omega_{\text{eff}}\tau}{2}\right)\right) \tag{4.26}$$

$$\delta\phi_{2\to2} = \arg\left(\langle 2|U(\tau)|2\rangle\right) = \arctan\left(\frac{\delta_{\text{tot}}}{\Omega_{\text{eff}}}\tan\left(\frac{\Omega_{\text{eff}}\tau}{2}\right)\right) \tag{4.27}$$

where $\Omega_{\text{eff}} = \sqrt{\Omega^2+\delta^2}$. The $\delta = \delta_{\text{Doppler}} + \delta_{\text{LS}}$ is the detuning which contains the Doppler effect and light shift due to the light pulse that includes the one photon and two photon light shift. In our experiment, we sweep the laser frequency to follow the motion of the atom cloud so the $\delta_{Doppler} = 0$. And the two photon light shift $\delta_{2\gamma}$ is much smaller than the one photon light shift $\delta_{1\gamma}$, $\delta_{1\gamma} \gg \delta_{2\gamma}$. As these two-phase share the same formula but different signs, in the following we will take $\delta\phi_{2\to2}$ as example.

So we can simplify the formula Equation 4.27 into :

$$\delta\phi = \text{arcran}\left(\frac{\delta_{1\gamma}}{\sqrt{\Omega^2+\delta_{1\gamma}^2}}\tan\left(\frac{\Omega_{\text{eff}}\tau}{2}\right)\right) + \frac{\delta_{2\gamma}}{\Omega}\frac{\sqrt{\Omega^2+\delta_{1\gamma}^2}}{2\delta_{1\gamma}^2+\Omega^2} \tag{4.28}$$

The first constant part is the phase induced by the **one photon light shift**, and the second part is due to the **two photon light shift**.

The two photon light shift is well explained in the previous thesis of Léo Morel [54]. Here we will focus on the one photon light shift, which is noted as **Residual Raman phase shift** in the error budget.

One photon light shift

The one photon light shift comes from the energy shift between the ground states $|1\rangle$, $|2\rangle$ and excited state $|e\rangle$, if we write them in the expression with the laser intensity.

$$\Omega = \frac{\Gamma^2}{16\Delta}\frac{\sqrt{I_1 I_2}}{I_s} \tag{4.29}$$

$$\delta_i^{1\gamma} = \frac{\Gamma^2}{8\Delta}\frac{I_i}{I_s} \tag{4.30}$$

where I_s is the saturation intensity. If the two lasers are equilibrated, which is true in our experiment, then the one photon light shift is twice the Rabi frequency. Fortunately, the light shift applies on both hyperfine levels, so in the experiment, we really care about the differential light shift due to the lasers, where the difference is related to the hyperfine energy shift ν_{HFS}.

$$\delta_{\mathrm{dif,i}}^{1\gamma} = \frac{I_i}{I_s}\frac{\Gamma^2 \nu_{\mathrm{HFS}}}{8\Delta^2} \tag{4.31}$$

In the counter propagating configuration, three laser beams are applied to the atoms. One is the reflection of one laser, so the total one photon light shift is a sum of them.

During the whole atom interferometer, the total phase shift due to this one photon light shift can be written as:

$$\delta\phi_{\mathrm{tot}} = -\delta\phi_I - \delta\phi_{II} + \delta\phi_{III} + \delta\phi_{IV} \tag{4.32}$$

where the index refers different order pulses.

Combining Equation 4.28 we can write this formula in a more explicit way:

$$\begin{aligned}\delta\phi_{tot}^{1\gamma} = \; & -\mathrm{arctan}\left(\tfrac{\delta_{\mathrm{Doppler}}+\delta_{1\gamma}}{\Omega_{\mathrm{eff}}^2}\tan\left(\tfrac{\Omega_{\mathrm{eff}}\tau}{2}\right)\right) \\ & -\mathrm{arctan}\left(\tfrac{\delta_{\mathrm{Doppler}}+\delta_{1\gamma}}{\Omega_{\mathrm{eff}}^2}\tan\left(\tfrac{\Omega_{\mathrm{eff}}\tau}{2}\right)\right) \\ & +\mathrm{arctan}\left(\tfrac{\delta_{\mathrm{Doppler}}+\delta_{1\gamma}}{\Omega_{\mathrm{eff}}^2}\tan\left(\tfrac{\Omega_{\mathrm{eff}}\tau}{2}\right)\right) \\ & +\mathrm{arctan}\left(\tfrac{\delta_{\mathrm{Doppler}}+\delta_{1\gamma}}{\Omega_{\mathrm{eff}}^2}\tan\left(\tfrac{\Omega_{\mathrm{eff}}\tau}{2}\right)\right)\end{aligned} \tag{4.33}$$

As we know, if the atom interferometer is closed, then the output phase shift should not depend on the initial velocity of the atom cloud. But this formula shows that due to the diagonal part of Hamiltonian, we have a phase shift depending on the initial velocity of the atom cloud. Of course, this effect is canceled when the four laser intensity is kept constant along the interferometer. But as the cloud expands in the Gaussian beam during the interferometer, the mean intensity seen by the atom cloud will decrease. To see this effect in our experiment, we scanned the initial mean velocity of the atom cloud. This is performed by tuning the frequency of the preselection Raman pulse.

Moreover, when presenting the Ramsey-Bordé interferometer, we saw that the natural variable to scan was the frequency of the second Ramsey sequence. However, in these conditions, the Rabi spectra probed by the atomic velocity distribution may vary sharply

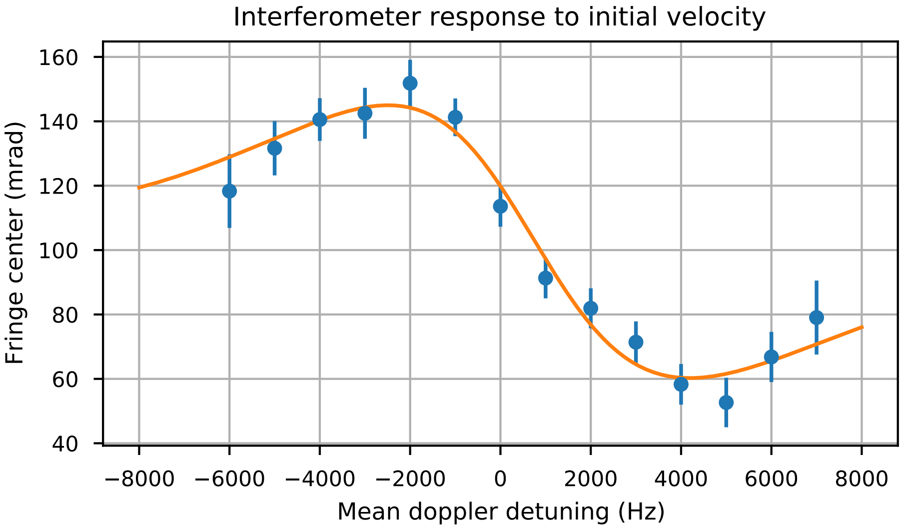

Figure 4.15: Dispersion behavior of the output phase of a Ramsey-Bordé interferometer by scanning the initial velocity of the atoms. The points are the experimental results and the orange line corresponds a fit with Equation 4.33. Extracted from [54]

with the pulse frequency. Hence, by scanning the frequency, the Rabi spectra shape may induce an additional shift of the central fringe. In order to prevent this effect, we scanned the phase of the last pulse. The experimental data and fit curves are plotted in Figure 4.15.

From the Figure 4.16 we can see a significant effect when we change the initial velocity of the atom when it enters the atom interferometer and the Equation 4.33 fits quite well with experimental data. To mitigate the effect, we linearly increase the intensity during the experiment to keep a constant mean intensity seen by the atoms. This measurement is performed under the same experimental condition as h/m but without Bloch oscillations. The experiment results is shown in Figure 4.16

We observed that when the intensity sent to the vacuum chamber is 10% higher for the last pulse than for the first pulse, the slope of the variation with the initial velocity is significantly reduced as well as the systematic effect induced by this phase shifts.

This effect is similar for each spectra and therefore should be canceled between the inversion of the direction of both the Raman beams and the Bloch acceleration. This compensation is not perfect for two reasons:

I. the temporal sequence being different when the Bloch acceleration is inverted, then the size of the cloud is slightly different.

II. the retro-reflected beam, which contributes twice, is different when the direction of the Raman beams is inverted.

A Monte Carlo simulation is used to precisely compute the light shift effect in these 8 different configurations, and the results are shown in Figure 4.17. These results are plotted as a function of the velocity of the cloud, detuning δ_D with respect to the resonance and run under three different light shift imbalance ϵ, which express the one photon light shift

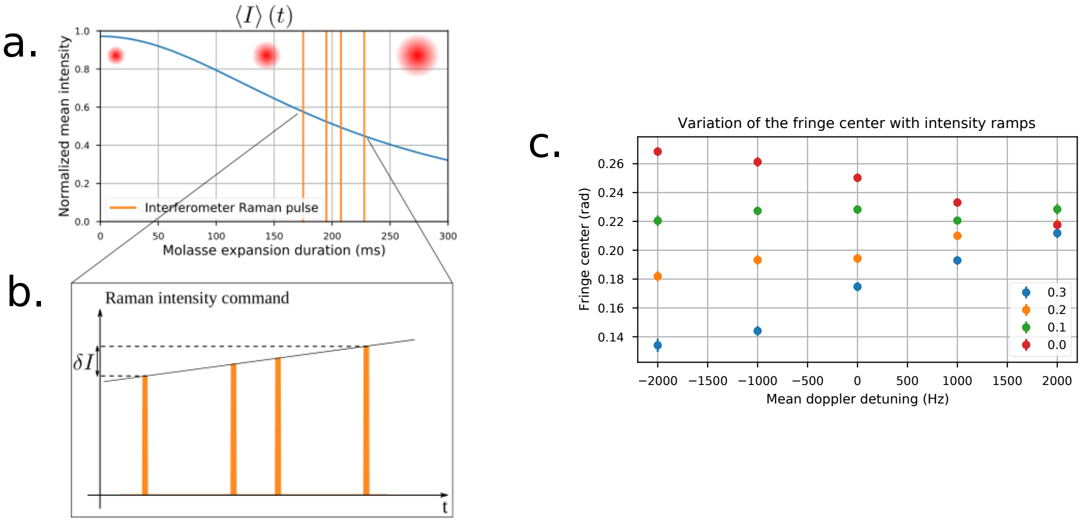

Figure 4.16: a: The decrease of the mean intensity seen by the atom cloud due to the cloud expansion. b: In order to keep a constant intensity we increase the intensity between the first and last pulse by δI. c: center phase measured with different intensity ramp, the label number tells the intensity increase between first and last pulse. For example, the green points means the last pulse intensity is 10% higher than the first pulse.

difference between two different Raman directions. We can see that different ϵ has quite different effect.

Using the results of the Monte Carlo simulation at zero Doppler detuning, we compute

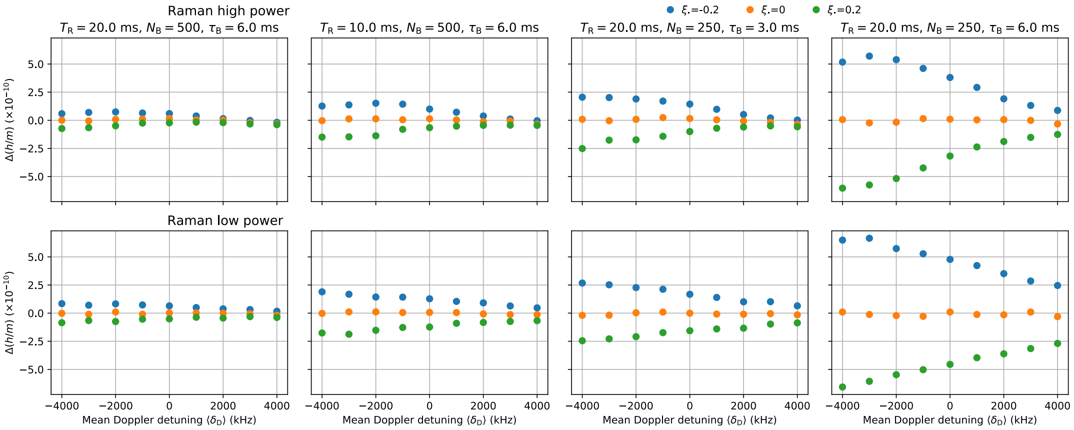

Figure 4.17: Results of the Monte Carlo simulation for the estimation of the effect of the one-photon light shift for different initial velocity and Raman inversion compensation (orange points: perfect compensation; blue and green points: one-photon light shift is 20% greater for one or the other Raman direction). The simulation was performed for all interferometer configurations.

the dependency of the systematic error with respect to the ϵ. The error then is

$$\frac{\Delta(h/m)}{h/m} = (\kappa_1 + \kappa_2 \langle \delta_{\mathrm{D}} \rangle)\epsilon \tag{4.34}$$

where δ_{D} is the average Doppler shift of the atomic distribution. We estimate the light shift imbalance ϵ to be 0.1 ± 0.1. The values of κ_1 and κ_2 are extracted from the Monte Carlo simulation for each of the eight configurations. In the end, we get the correction on the α

$$\frac{\Delta\alpha}{\alpha} = (2.3 \pm 2.3) \times 10^{-11} \tag{4.35}$$

4.3 Conclusion:

After finishing all the systematic effect measurement, calculate from the error budget we got $h/m(^{87}\mathrm{Rb}) = 4.591\,359\,258\,90(65) \times 10^{-9}\,\mathrm{m}^2/\mathrm{s}$. As in the international system of units adopted in 2019, the planck constant h is fixed so this also means we obtains the most accurate atomic mass measurement so far $m(^{87}\mathrm{Rb}) = 1.443\,160\,897\,76(21) \times 10^{-25}\mathrm{kg}$.

we have obtained the determination of α with relative uncertainty 8.1×10^{-11}.

$$\alpha^{-1} = 137.035\,999\,206(11)$$

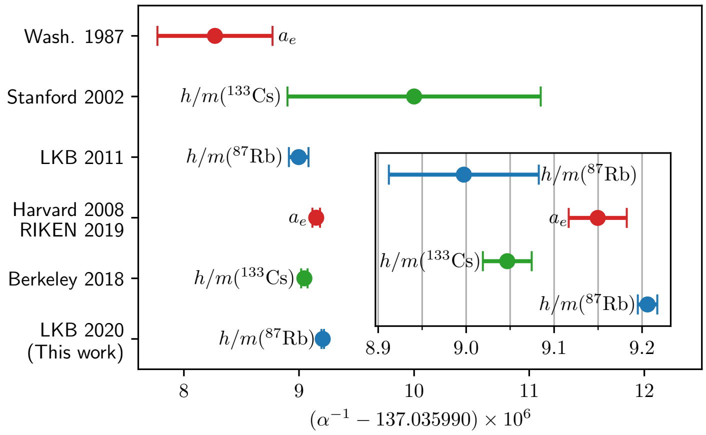

Figure 4.18: Comparison of most precise determinations of the fine-structure constant so far. The red points are from $g_e - 2$ measurements and QED calculations, and the green and blue points are obtained from measurements of caesium and rubidium atomic recoils, respectively.

Using our measurement of the fine-structure constant, the standard-model prediction of the anomalous magnetic moment of the electron becomes

$$a_{\mathrm{e}} = 1\,159\,652\,180.252(95) \times 10^{-12}$$

The relative uncertainty on g_{e} is below 0.1 ppt, which is the most accurate prediction

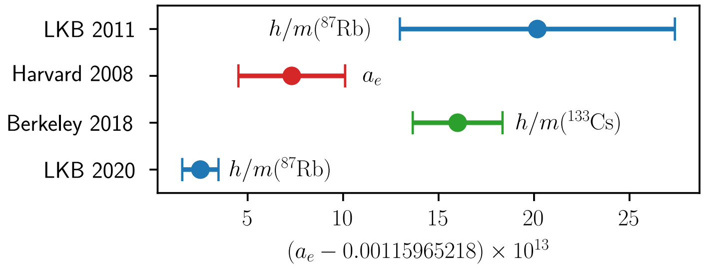

Figure 4.19: Comparison of most precise determinations of the a_e so far. The red points are from $g_e - 2$ measurements , and the green and blue points are obtained from measurements of caesium and rubidium atomic recoils, respectively.

of the standard model. Comparison with the direct experimental measurement of $a_{\mathrm{e,exp}}$ [**a_emeasure**].

$$\delta a_\mathrm{e} = a_{\mathrm{e,exp}} - a_\mathrm{e}(\alpha_{2020}) = (4.8 \pm 3.0) \times 10^{-13}$$

where we have a 1.6σ difference between these two values. We expect a better test on the Standard Model in next years as an improvement of one order of magnitude is expected for the accuracy of the measurement of a_e[2].

Here I want to mention the two discrepancies:

- First our recent value is quite different from what the group got in 2011. The reason is the three new systematic effect discussed in this this manuscript. Unfortunately in 2011 the experiment set up is different from what we used now and we didn't have the relative data about the beam profile and Raman phase lock.
- Our recent result has a 5.6σ difference from the previous caesium recoil measurement done in Berkeley. More studies should be made to understand this.

For our next step, as we see in our error budget this uncertainty contribution from the h/m measurement is 2.4×10^{-11} (statistical) and 6.8×10^{-11}. We are more limited by the systematic effects than the statistical. And the three biggest effects are related with the cloud size and expansion. So if we want to try a better measurement, doing the h/m with Bose Einstein condensate (BEC) will be a good option. In the next chapter, I will talk about the atom interferometer with Bose Einstein condensate, which is also my main contribution on this experiment during my PHD study.

Part II

Atom interferometer with Bose-Einstein Condensate

Chapter 5

Bose-Einstein Condensate and atomic interaction

In Chapter III, we have shown that the transverse expansion of the cloud in the beam is responsible for one of the biggest source of uncertainty: the residual one-photon light shift. In order to mitigate this effect, Bose-Einstein condensates (BEC) are ideal sources due to their low transverse velocity. In addition, using BEC also increases the efficiency of large momentum atomic beam splitters which is a promising tools for reaching very high sensitivities[25, 56, 23, 36]. Moreover, atomic interactions that are inherent in such dense cloud can generate spin squeezing, which seems a promising strategy to surpass the standard quantum limit [71, 60, 42, 53].

However atomic interaction will also induce a detrimental phase shift that can undermine the benefits of using BEC for precision measurements with atom interferometry. Understanding and controlling the effects of atomic interaction is thus crucial when we use BEC in light-pulse atom interferometers. Some work has already shown that this interaction can not only create a total phase shift at the output of the interferometer but also a non-uniform spatial phase profile.[42, 16, 74, 66]. This phase, which depends on the density of the BEC, impacts the accuracy of measurements performed with atom interferometers. In the next two chapters, I will first present the production of a BEC source and details of this interaction effect.

In this chapter, I first give a general information about the BEC and a general way to generate a BEC. Then some theoretical explanation on the atomic interaction in BEC and free fall expansion of the BEC in the Thomas-Fermi regime. At the end I will show how we produce a BEC in a short evaporation sequence.

5.1 General aspects of Bose-Einstein condensates

In this section, we briefly present the main concepts concerning atomic Bose-Einstein condensates, in particular, the regime (the so-called Thomas-Fermi regime) in which the Rubidium condensates are used in atomic interferometry experiments are found. We also present the experimental setup and the protocol we used to produce our ^{87}Rb condensate in the $F = 1, m_f = 0$ of the $5S_{1/2}$ electronic ground state.

Bose-Einstein statistics tells us that the mean atom number N_i in an individual state i of energy ϵ_i can be written as:

$$N_\mathrm{i} = \frac{1}{\exp(\beta(\epsilon_i - \mu)) - 1} \tag{5.1}$$

In this equation, $\beta = 1/k_B T$ where k_B is Boltzmann constant and T is the temperature, μ is the chemical potential. Let's define $z = \exp(\beta\mu)$ then the formula above can written as

$$N_i = \frac{z}{\exp(\beta\epsilon_i) - z} \tag{5.2}$$

As the ground state energy $\epsilon = 0$ and N_0 cannot be negative, we have $0 \leqslant z < 1$. The total atom number of this system is the sum over all the states.

$$N_\mathrm{tot} = \frac{z}{1-z} + \sum_{i \neq 0} g_i \frac{z}{\exp(\beta\epsilon_i) - z} \tag{5.3}$$

Where the first part is the atom number in the ground state N_0 and the second part is the atom number in the excited states N_ex and g_i is the degeneracy of the energy ϵ_i. From Equation 5.2, it's easy to see that the number of excited atoms increases with z. Since $0 \leqslant z < 1$, the excited atom numbers reach its maximum value when $z = 1$.

$$N_\mathrm{ex} \leqslant N_\mathrm{max} = \sum_{i \neq 0} \frac{g_i}{\exp(\beta\epsilon_i) - 1} \tag{5.4}$$

This shows us a fascinating condensation phenomenon: imagine that the volume of a box V and the temperature T can be fixed so that we have a defined N_max which is non-infinite. If we continually add atoms into this system, when $N_\mathrm{tot} > N_\mathrm{max}$ there is at least $N_\mathrm{tot} - N_\mathrm{max}$ atoms which fall into the ground states. So once the threshold $N = N_\mathrm{max}$ is reached, every new atom added into this system must be accommodated by the ground state and the population of the ground state $N_0 = z/(1-z)$ can never be saturated because z can be infinitely close to 1. If N_tot is sufficiently large then we can consider that nearly all the atoms are in the ground state. By this way, we get the Bose-Einstein Condensate (BEC).

Critical temperature

Instead of increasing the atom number with fixed volume **V** and temperature **T**, it is also possible to decrease **T** with fixed volume **V** and atom number **N**. Suppose **T** is progressively decreased from a high value. In that case, N_max also decreases from a large initial value until it becomes equal to the atom number **N** for a certain value of **T** called the BEC critical temperature T_c, which is defined for a given N as the temperature below which the BEC appears. Because if we continue decreasing the temperature **T**, then N_max will be smaller than **N** and then more and more atoms will fall into ground state.

Now we consider that the atoms are in an infinite big system where the energy difference is negligible compared to $\mathrm{k_B T}$. So the last part of Equation 5.3 can be written as an integral and assuming that the degeneracy g_i is one:

$$N = N_0 + \int\int\int \frac{ze^{-\beta\epsilon_{\mathrm{n_x.n_y,n_z}}}}{1 - ze^{-\beta\epsilon_{\mathrm{n_x.n_y,n_z}}}} dn_x dn_y dn_z \tag{5.5}$$

and the excited part can be written as below [26]:

$$N_{ex} = \frac{V}{\lambda_T^3} g_{3/2}(z) \tag{5.6}$$

where $g_n(z) = \sum_{l+1}^{\infty}(z^l/l^n)$ is maximal when z=1, $g_{3/2}(1) \sim 2.612$, and $\lambda_T = \sqrt{2\pi\hbar^2/mk_BT}$ is the de Broglie wavelength. So with a given atom number and volume when we decrease to the critical temperature we have

$$\rho\lambda_{\mathrm{Tc}}^3 \simeq 2.612 \tag{5.7}$$

The de Broglie wavelength can be understood as the width of the wave packet, and the density relates the distance between atoms. So here, a very interesting thing happens is that the atoms' wave-packets are overlapped where we cannot distinguish each atom. They are all identical.

Of course if we continue decreasing the temperature then more and more atoms will fall into the ground state. The proportion of atoms in the ground state is:

$$\frac{N_0}{N} = 1 - \left(\frac{T}{T_c}\right)^3 \tag{5.8}$$

5.2 Atomic interactions : Gross-Pitaevskii Equation

The description of a Boson assembly without interaction allows an intuitive understanding of the condensation phenomena. However, it does not allow for a description of the case of a degenerate gas where interactions are present. Even weak interactions significantly modify the wave function of the Bose-Einstein condensate.

Now there are N identical Bosons trapped in a potential $\mathbf{V}$, and as all of them are in the ground state, we can write the wave function of the system as

$$|\psi\rangle = |\varphi\rangle \otimes |\varphi\rangle \otimes |\varphi\rangle \cdots \otimes |\varphi\rangle \tag{5.9}$$

The Hamiltonian of the system can be expressed as below:

$$\hat{H} = \frac{1}{2m}\sum_{i=1}^{N} \mathbf{P_i^2} + \mathbf{V}(\mathbf{r}, \mathbf{t}) + \frac{1}{2}\sum_{j\neq i} \mathbf{V_{int}}(r_i - r_j)) \tag{5.10}$$

where the second term is the trapping potential, which is usually approximated by a harmonic trap:

$$V(r,t) = \frac{1}{2} \sum_{j=x,y,z} m\omega_j^2(t) r_j^2 \tag{5.11}$$

where ω_j are the trapping frequencies. The last term of equation 5.10 is the two-body interaction between the atoms. In our experiment, $na^3 \approx 10^{-5} \ll 1$ means that our cloud is a dilute gas and the distance between each atom is much bigger than the s-wave scattering length a. So we can replace the interaction potential with a Dirac function $\delta(r_i - r_j)$. It tells us that the interaction happens only if these two wave functions overlap. In other words, they have a collision. The pseudo-potential can be written as:

$$V_{\text{int}}(r_i - r_j) = g\delta(r_i - r_j) \quad \text{with} \quad g = \frac{4\pi\hbar^2 a}{m} \tag{5.12}$$

Then we can rewrite the Hamiltonian of the system:

$$\hat{H} = \frac{1}{2m} \sum_{i=1}^{N} \mathbf{P_i^2} + \mathbf{V(r,t)} + \frac{1}{2} \sum_{j \neq i} g\delta(r_i - r_j) \tag{5.13}$$

Because the bosons are all in the ground state, the system energy should be minimised, which means,

$$\frac{\partial(\langle\psi|\hat{H}|\psi\rangle - \langle\psi|\mu|\psi\rangle)}{\partial\varphi} = 0 \tag{5.14}$$

In this way we get the time-independent Gross-Pitaevskii Equation:

$$-\frac{\hbar^2}{2m}\vec{\nabla}^2\varphi + V(r,t)\varphi + g(N-1)|\varphi|^2\varphi = \mu\varphi \tag{5.15}$$

This equation looks like a non-linear Schrödinger equation. It gives us the evolution of each atom in the trapping potential and the mean-field potential created by the $N-1$ other atoms surrounding it, which is related to the atom density $\rho = N|\varphi|^2$ ($N \gg 1$).

5.3 Description of the BEC under the Thomas-Fermi regime

5.3.1 Thomas-Fermi regime

This interaction potential creates a repulsive force between each atom. Consequently, this repulsive force will make the cloud bigger, which means the more atomic interaction we have, or in other words, the more atoms we have in the condensate, the bigger cloud we will have, which means a smaller kinetic energy (because the wave function has a larger spatial width) but a larger interaction energy. Suppose we continually increase the atom numbers in the condensate with a given trapping potential **V** then there must be a situation where among the three energies involved in the Gross-Pitaevskii equation, only the interaction and potential energies contribute to the properties of the condensate and the kinetic energy becomes negligible. This regime is called the Thomas-Fermi regime.

For a condensate in an isotropic trap of spatial extension R, the kinetic energy term is of the order of $\hbar^2/2mR^2$, and the interaction term is of the order of $g\rho \sim (Ng)/(R^3)$. For the Thomas Fermi criteria is

$$Ng \gg \frac{\hbar^2 R}{2m}$$

The spatial extension of the ground state in an harmonic trap is $a_{\text{oh}} = \frac{\hbar}{\sqrt{m\bar{\omega}}}$, where $\bar{\omega} = (\omega_x\omega_y\omega_z)^{1/3}$. One can deduce a criteria for the Thomas Fermi regime:

$$N_0 a/a_{\text{oh}} \gg 1 \tag{5.16}$$

In the Thomas-Fermi regime, the density profile of the atomic cloud can be solved from the time-independent Gross-Pitaevskii rewritten below:

$$(\mathbf{V}(\mathbf{r},\mathbf{0}) + gN|\varphi|^2)\varphi = \mu_{\text{TF}}\varphi \tag{5.17}$$

Where the μ_{TF} is the chemical potential in the Thomas-Fermi approximation. Then it's easy to get the wave function

$$\begin{aligned} N|\varphi(r,0)|^2 &= \frac{\mu_{\text{TF}}}{g}\left[1 - \left(\frac{x}{X_{\text{TF}}}\right)^2 - \left(\frac{y}{Y_{\text{TF}}}\right)^2 - \left(\frac{z}{Z_{\text{TF}}}\right)^2\right] \\ &\times \Theta\left(1 - \left(\frac{x}{X_{\text{TF}}}\right)^2 - \left(\frac{y}{Y_{\text{TF}}}\right)^2 - \left(\frac{z}{Z_{\text{TF}}}\right)^2\right) \end{aligned} \tag{5.18}$$

where we have defined the Thomas-Fermi lengths of the condensate as $X_{\text{TF}} = \sqrt{2\mu_{\text{TF}}/m\omega_x}$ (resp. y, z) and $\Theta(s)$ is the Heaviside function where $\Theta(s) = 1$ when $s > 0$ otherwise it equals zero.

Finally the chemical potential μ_{TF} is determined by the normalisation of the $|\varphi|^2$ to the number of atoms N

$$\mu_{\text{TF}} = \frac{\hbar\bar{\omega}}{2}\left(15Na\sqrt{\frac{m\bar{\omega}}{\hbar}}\right)^{\frac{2}{5}} \tag{5.19}$$

5.3.2 Expansion of the Bose-Einstein condensate in Castin Dum model

If we want to know the expansion after removing the trapping potential, we need to solve out the time dependant Gross-Pitaevskii Equation

$$i\hbar\frac{\partial\varphi}{\partial t} = -\frac{\hbar^2}{2m}\vec{\nabla}^2\varphi + V(r,t)\varphi + gN|\varphi|^2\varphi \tag{5.20}$$

The model proposed by Castin and Dum [22] gives a relevant description of the wave-function of the BEC after release from the trap. In the trap each atom experiences a force which is the gradient of the potential:

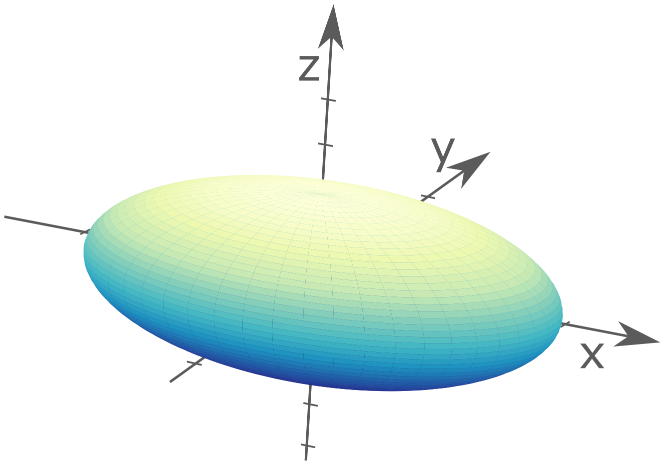

Figure 5.1: Surface plot of the shape of the wave function of the BEC trapped by an harmonic trap in Thomas-Fermi regime Equation 5.18.

$$\mathbf{F}(\mathbf{r},t) = \nabla V(\mathbf{r},t) + \frac{1}{2} g N \nabla \rho(\mathbf{r},t) \quad \text{with} \quad \rho(\mathbf{r},t) = N|\varphi(\mathbf{r},t)|^2 \tag{5.21}$$

Before the trapping potential is switched off the atoms are in an equilibrium condition $\vec{F} = 0$ so the solution of this classical model coincides with the wave function of the Thomas-Fermi regime. The Castin Dum model relies on the assumption that the condensate dilates like a balloon according to the following scaling laws

$$r_j(t) = \lambda_j(t) r_j(0) \quad (j = x, y, z) \tag{5.22}$$

where the $r_j(0)$ correspond to the initial position of the atom and the velocity of the atom is $v(t) = \dot{\lambda}(t) r_j(0)$. Using Newton's law, $m\ddot{\mathbf{r}}(t) = \mathbf{F}(\mathbf{r},t)$, we can deduce the differential equation of $\lambda(t)$ in an harmonic trap.

$$\ddot{\lambda}_j = \frac{\omega_j^2(0)}{\lambda_j \lambda_x \lambda_y \lambda_z} - \lambda_j \omega_j^2(t) \tag{5.23}$$

At $t \geqslant 0$, we turn off the harmonic trap so the $\omega_j(t) = 0$. Then we get the numerical result of $\lambda(t)$.

From Figure 5.2, we can see that at the beginning the atom doesn't move ($\lambda(t) \approx 1$). This is because in the Thomas-Fermi regime, the kinetic energy is zero. However $\dot{\lambda}(t)$ increases quickly which means that after we remove the trapping potential, the interaction potential begins to convert into kinetic energy immediately. At the end, all the interaction energy turns into kinetic energy and the velocity of the atoms stays constant.

We now consider a simple case: we have only one component BEC and the solution of Equation 5.20 is given below.

$$\varphi(r,t) = e^{-i\beta(t)} e^{im \sum_j r_j(t)^2 \dot{\lambda}_j(t)/2\hbar\lambda_j(t)} \frac{\varphi(r,0)}{\sqrt{\lambda_x(t)\lambda_y(t)\lambda_z(t)}} \tag{5.24}$$

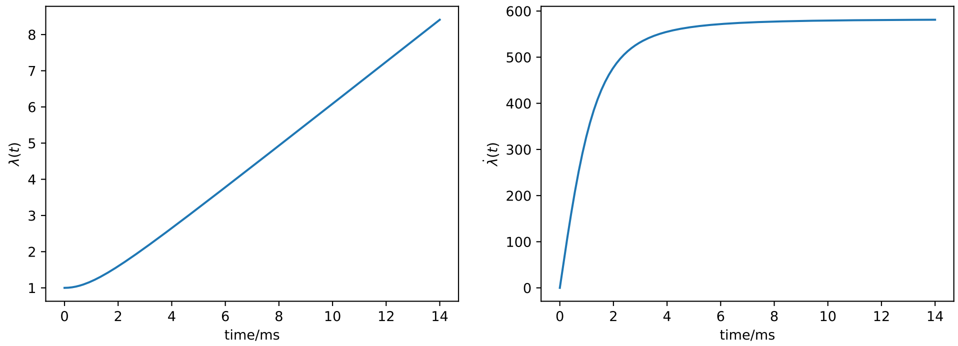

Figure 5.2: Time evolution of $\lambda_z(t)$ (left) and of $\dot{\lambda_z}(t)$ (right)

where $\hbar\dot{\beta}(t) = \mu/(\lambda_x(t)\lambda_y(t)\lambda_z(t))$ and $\varphi(r, 0)$, which can be derived from Equation 5.18, is the wave function at time $t = 0$ when the trap is switched off.

5.4 The BEC production in an all-optical trap

5.4.1 Evaporative cooling

Evaporative cooling is a very efficient and commonly used method to produce a BEC. The principle is to remove the most energetic atoms from the upper tail of the energy distribution and profit from the subsequent thermalization of the remaining atoms by elastic collisions. The process is illustrated in figure 5.3: atoms with an energy higher than the trap depth U_0 escape the trap and thermalization of the atom cloud to a lower temperature occurs via elastic collisions. By continuously decreasing the trap depth U_0, one can force the evaporation process until all atoms are in the ground state.

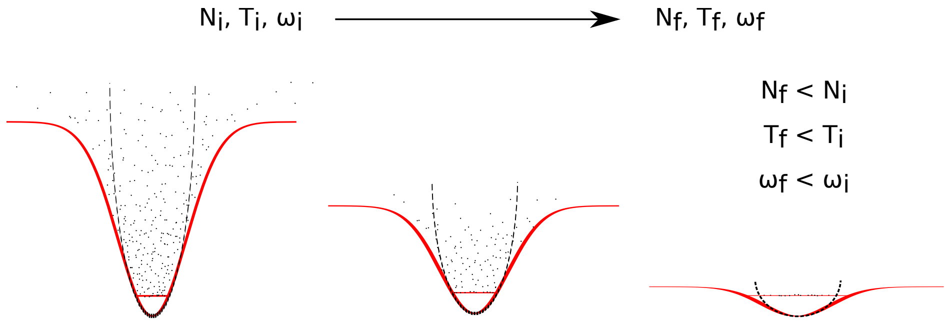

Figure 5.3: The evaporation process to get BEC. The atom number in the trapped gas and its temperature are reduced, as well as the potential height and confinement frequency. Extracted from [27]

In our experiment we use an optical trap to do the evaporative cooling, the details are well explained in [27, 46]. In order to avoid strong magnetic field in our experiment, we choose optical instead of magnetic trap.

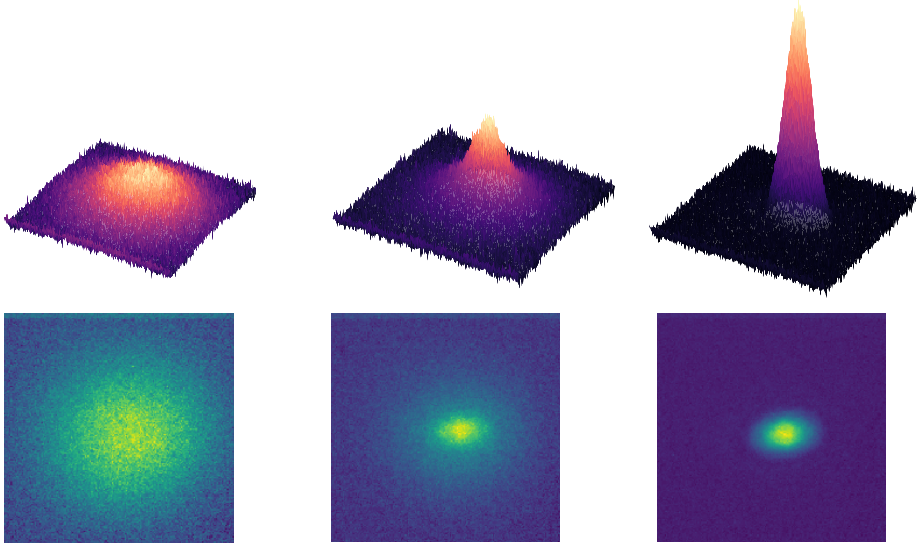

Figure 5.4: We use the absorption imaging system to detect atoms at the same detection time $t_{\text{det}} = 33ms$. The bottom pictures are extracted at different time of the experimental evaporation cooling process. The top pictures are the corresponding 3D plots. From left to right is thermal gas, the first appearance of BEC and the BEC.

During my thesis I improved the evaporative cooling so that we can generate 220 000 atoms in the BEC with 3.2 s (1.5 s loading of the MOT and 1.7 s evaporation) compared to the previous result with the production of 120 000 atoms in a BEC with a 3.5 s(1.5 s loading of the MOT and 2 s evaporation)[54]. Furthermore, the stability of the BEC is highly improved, before the BEC production system requires daily adjustment while now this system can be stable for almost two months with a relative atom fluctuation about 8%. .

5.4.2 The spin distillation technique

To run the interfeometer, we want to have a nonmagnetic state at the output of the evaporative cooling. Unfortunately, the dipole trap is nonsensitive to the hyperfine Zeeman sublevels. So if we only use the dipole beam to do evaporative cooling, we will have all the three $m_{\text{F}} = 0, \pm 1$ levels at the end, which means only 33% atoms can be used.

To solve this problem, we use the spin distillation technique [28]. During the evaporation process, we turn on the magnetic field slowly from 0 to maximum value in 0.5 s and turn it off just 160 ms before the end of the evaporation. The principle is that the collision between atoms will redistribute the spin of atoms. For example, collision of $m_{\text{F}} = 1$ and $m_{\text{F}} = -1$ can turns them into two atoms in $m_{\text{F}} = 0$. Moreover, due to the additionnal magnetic field, the potential of the magnetic sensitive $m_{\text{F}} = \pm 1$ is lowered at the edge of the trap (see Figure 5.5) which makes these two states easily fall out of the dipole trap ; all atoms in $m_{\text{F}} = \pm 1$ will evaporate from the dipole trap first and only $m_{\text{F}} = 0$ can remain. Now at the end of evaporation, we have a pure BEC in $m_F = 0$ state with 70% initial atom

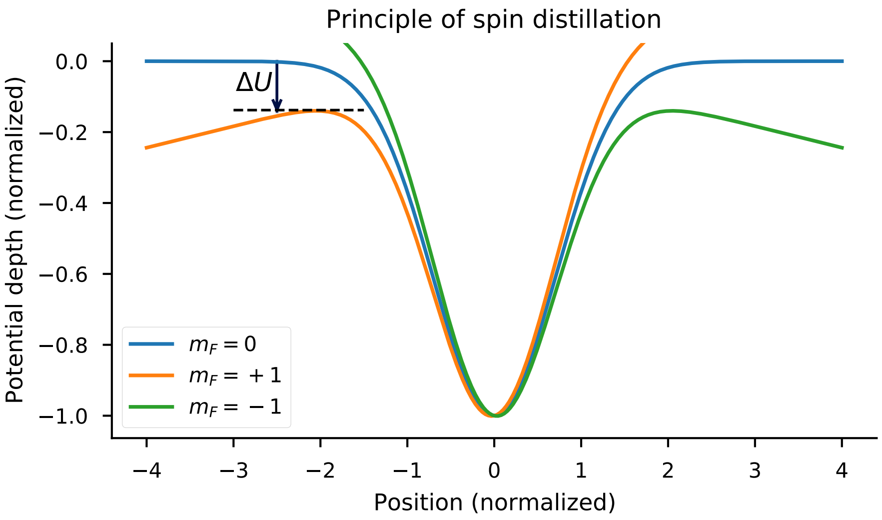

Figure 5.5: Potential felt by the atoms in different m_{F} states shown in different colors. The adding magnetic field doesn't affect the potential felt by the atom in $m_{\mathrm{F}} = 0$ but does affect the magnetically sensitive states $m_{\mathrm{F}} = \pm 1$ and lower the potential height.

left. This technique double the atoms in $m_{\mathrm{F}} = 0$.

5.4.3 Diplole potential created by a gaussian beam

5.4.4 Crossed Dipole trap

Two types of conservative trapping potentials. In our experiment we use a far-red detuned laser with a wavelength of $1064\,\mathrm{nm}$ to do a optical trap. and the total power of 50W is separated into three different beams to create a crossed dipole trap to improve the evaporation efficiency.

The dipole potential created by one gaussian laser

When an atom is placed in a laser field with angular frequency ω far away from atomic resonance ω_0, the dipole potential seen by the atom can be written as below:

$$U(r) = \frac{3\pi c^2}{2\omega_0^3}\frac{\Gamma}{\Delta}I(r) \tag{5.25}$$

where c is speed of light, Γ is the natural linewidth, $\Delta = \frac{1}{\omega-\omega_0} - \frac{1}{\omega+\omega_0}$, and $I(r)$ is the intensity of the laser field. If we consider a gaussian laser beam focused on the atom, which propagates along the z direction and with a waist w_0 and power P, $I(r)$ is given by:

$$I(r) = \frac{2P}{\pi w^2(z)}e^{-2\frac{r^2}{w^2(z)}} \tag{5.26}$$

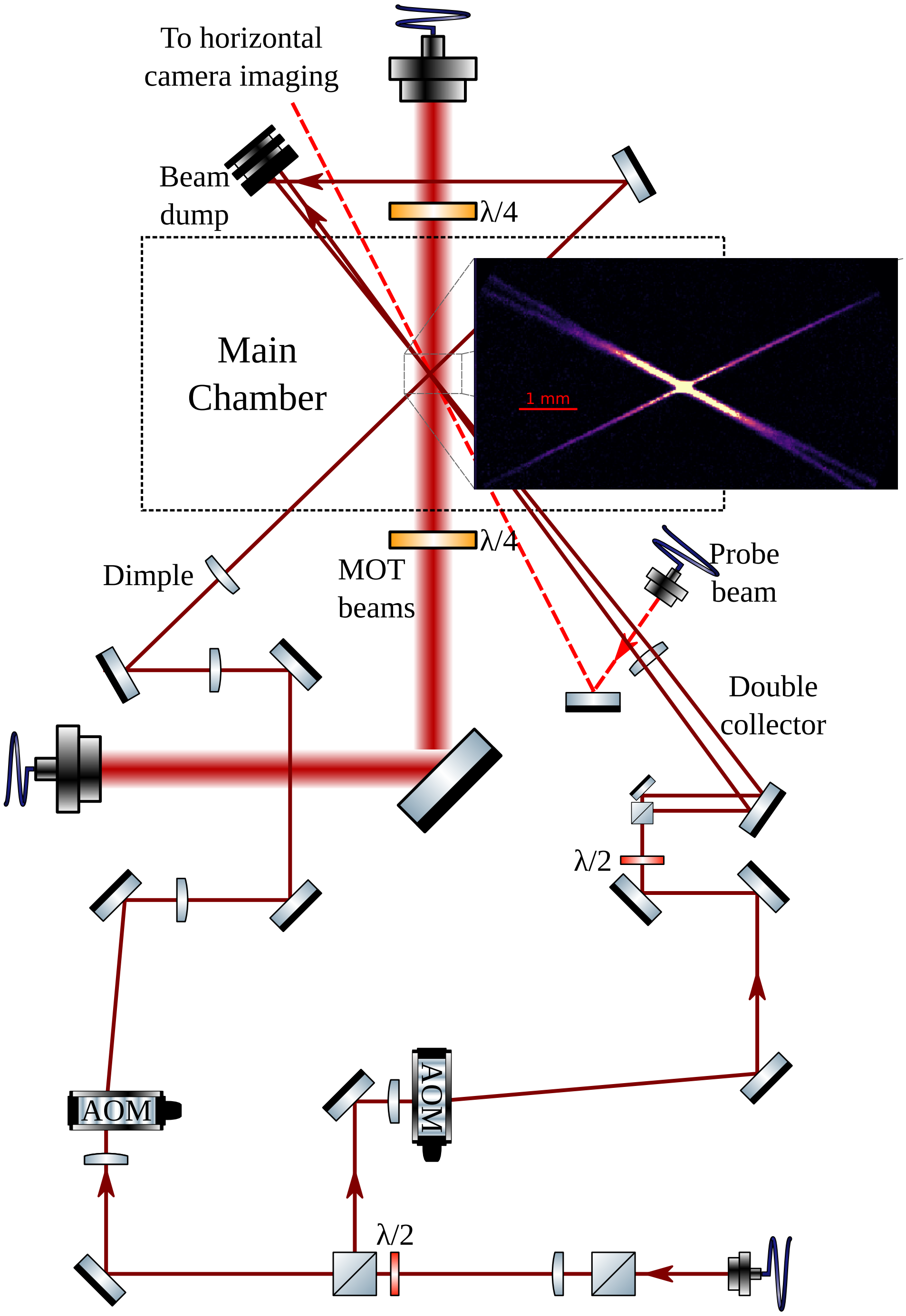

Figure 5.6: Schematic representation of the optical tables surrounding the main chamber (top view). inset:image of the three dipole beams through the observation of atoms that are trapped at 1ms time of flight. The image is saturated so that the tails of the trap are distinguishable.

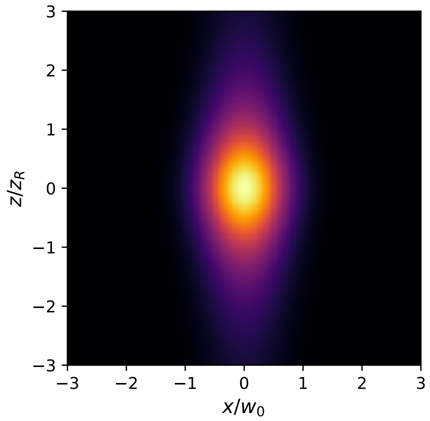

Figure 5.7: The potential created by one gaussian laser in plan XZ. Here the ratio $z_{\rm R}/w_0 \approx 315$

where $w^2(z) = w_0\sqrt{1+(z/z_{\rm R})^2}$, $z_{\rm R} = \pi w_0^2/\lambda$ is the rayleigh length of the laser and λ is the wavelength of the laser. From these expressions, we can rewrite the dipole potential as below:

$$U(r,z) = -\frac{U_0}{1+(\frac{z}{z_R})^2}e^{-2\frac{r^2}{w^2(z)}} \quad \text{with} \quad U_0 = \frac{3\pi c^2}{2\omega_0^3}\frac{\Gamma}{|\Delta|}\frac{2P}{\pi w_0^2} \tag{5.27}$$

Because the dipole laser is far-red detuned ($\Delta \ll 0$), we can neglect the spontaneous emission caused by the laser. All the atoms feel a dipole force towards the center of the beam. The focus of the laser beam can be adjusted to ensure that it coincide with the center of the the molasses. Under this condition, for $z \approx 0$ and $r \approx 0$, equation **Eq.** 5.27 can be simplified as below:

$$U(r,z) \approx -U_0 \times \left(1 - 2\left(\frac{r}{w_0}\right)^2 - \left(\frac{z}{z_R}\right)^2\right) \tag{5.28}$$

Under this approximation, the potential is harmonic and we can define two trapping frequencies along the longitutindal direction $\omega_z/2\pi$ and the transverse direction $\omega_\perp/2\pi$:

$$\omega_z = \sqrt{\frac{2U_0}{mz_R^2}} \quad \text{and} \quad \omega_\perp = \sqrt{\frac{4U_0}{mw_0^2}} \tag{5.29}$$

With our experimental parameters $\lambda = 1064\,\mathrm{nm}$ and $w_0 = 107\,\mu\mathrm{m}$ the ratio between these two trapping frequencies $\omega_z/\omega_\perp = \lambda/(\sqrt{2}\pi w_0) \approx 2\times10^{-3}$. This corresponds to a very anisotropic trap, which means that the atoms will be strongly confined in the transverse dimension but not along the beam direction as shown clearly in the Figure 5.7.

Dipole potential created by crossed laser beams

Theoretically, we can use only one laser to trap the atoms and do the evaporation cooling to generate the BEC. But the strong anisotropic trap will cause many problems. In order to

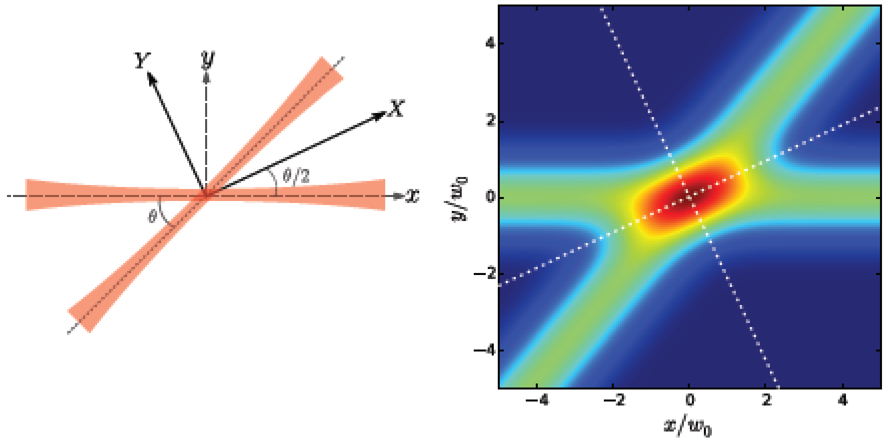

Figure 5.8: Left: configuration of two crossed dipole deams. Right: The potential created by two crossed gaussian lasers. Extracted from [46]

reduce this anisotropy, we use two laser beams crossing with an angle θ.

In this configuration, the trapping frequencies along x, y, z are given by the formulae below:

$$\begin{cases} \omega_x &= \sqrt{(1-\cos(\theta))\omega_\perp^2 + (1+\cos(\theta))\omega_z^2} \\ \omega_y &= \sqrt{(1+\cos(\theta))\omega_\perp^2 + (1-\cos(\theta))\omega_z^2} \\ \omega_z &= \sqrt{2}\omega_\perp \end{cases} \tag{5.30}$$

where $\omega_\perp$ and ω_z are given by Equation 5.29. From the Equation 5.30, we can see that by increasing the crossing angle between the two beams, the tapping frequencies in each direction get closer.

In our actual experiment, we cross a laser beam with a tight waist of $28\,\mu\mathrm{m}$ called dimple and two beams with large waists of $170\,\mu\mathrm{m}$ called reservoirs with $60°$ to reduce this anisotropic. The two reservoir beams cross with a small angle $\sim 5.6°$ to increase the trapping volume of our optical trap to trap more atoms. Moreover, with this configuration (shown in 5.6), we can generate a deep trapping potential and have a high-efficiency evaporative cooling.

The total potential generated by these three beams has a wine-glass shape shown in Figure 5.9, the small waist of the dimple beam creates a deep potential which can highly increase the collision rate between the atoms. At the same time, the relatively big waist of the reservoir beams can still trap the atoms that escape from the dimple beam. This way, we can have effective evaporation and decrease the atom loss rate. Typically at the end of our 1.7s evaporation cooling, we have trapping frequencies (50,115,115)Hz with around $220\,000$ condensed atoms.

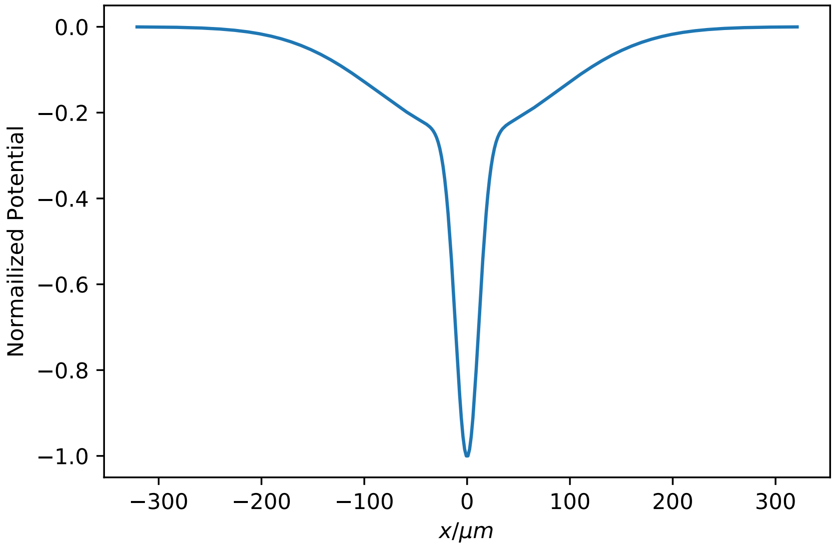

Figure 5.9: The total potential created by the dimple and reservoir beams.

5.4.5 Experimental implementation

Our dipole trap is turned on during the molasses phase. There are two ways to trap more atoms at the beginning: increasing the dipole beams' power to increase the depth of the potential or producing a colder and denser atom cloud. We use the process shown in Figure 5.10 to achieve this goal.

We always start with molasses in $|F = 2\rangle$, and then we increase the magnetic field to its maximum to compress the cloud to get a higher density in a phase called compressed MOT. The repumping light in the trapping beams amplified by the MOPA is then mechanically shut down, and after the compress MOT, our dipole beam is switched on with full power in the reservoir beams but without dimple. First, we want to use big reservoir beams to trap as many atoms as possible in the dipole trap. But we do not turn on the dimple beam because a small dimple beam will highly increase the density of atoms at the beginning of the dipole trap and consequently enhance the three-body losses.

The repump amplitude is controlled through the auxiliary channels shared with the absorption imaging system. This repump amplitude is immediately shut down at the end of the dipole loading stage. Ultimately, all the atoms fall into $|F = 1\rangle$ and are no longer sensitive to the cooling laser. Since there is no photon pressure this cloud gets colder and denser. We call this process a 'Dark molasse'. In this way, we increase the density of the cloud, and once the atoms fall into the 'Dark molasses', they will immediately be trapped by the dipole beams. As our dipole beam is far-red detuned from the resonance, we can neglect the spontaneous emissions caused by the dipole lasers.

And then we slowly sweep the power in the reservoirs and dimple to load atoms into the dimple beam, which can later give us quick and effective evaporation and then retrapped by the reservoir beams, shown in Figure 5.11. Simultaneously we switch on the Magnetic field

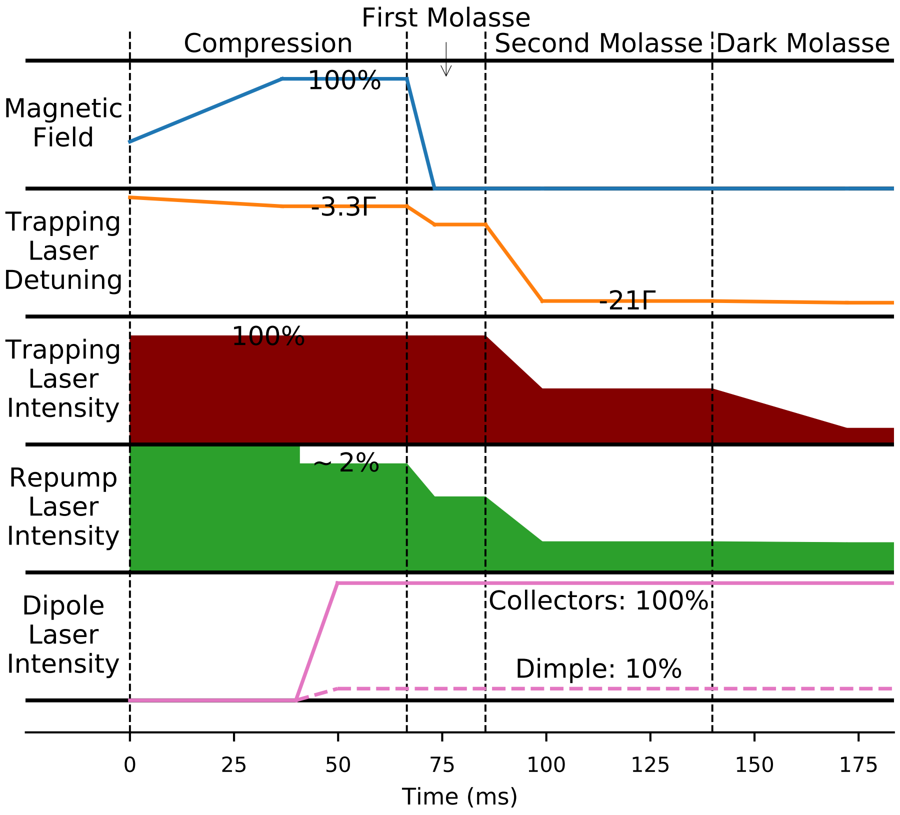

Figure 5.10: Steps sequence for the efficient loading of the dipole trap. At the end of the sequence, the trapping and repump laser are abruptly shut off while the dipole laser powers are then ramped for the evaporation sequence.

to implement the spin distillation. After around 1.7s evaporation, at the output, we have a BEC containing 220,000 atoms in an insensitive magnetic state with trapping frequencies [50, 115, 115]Hz.

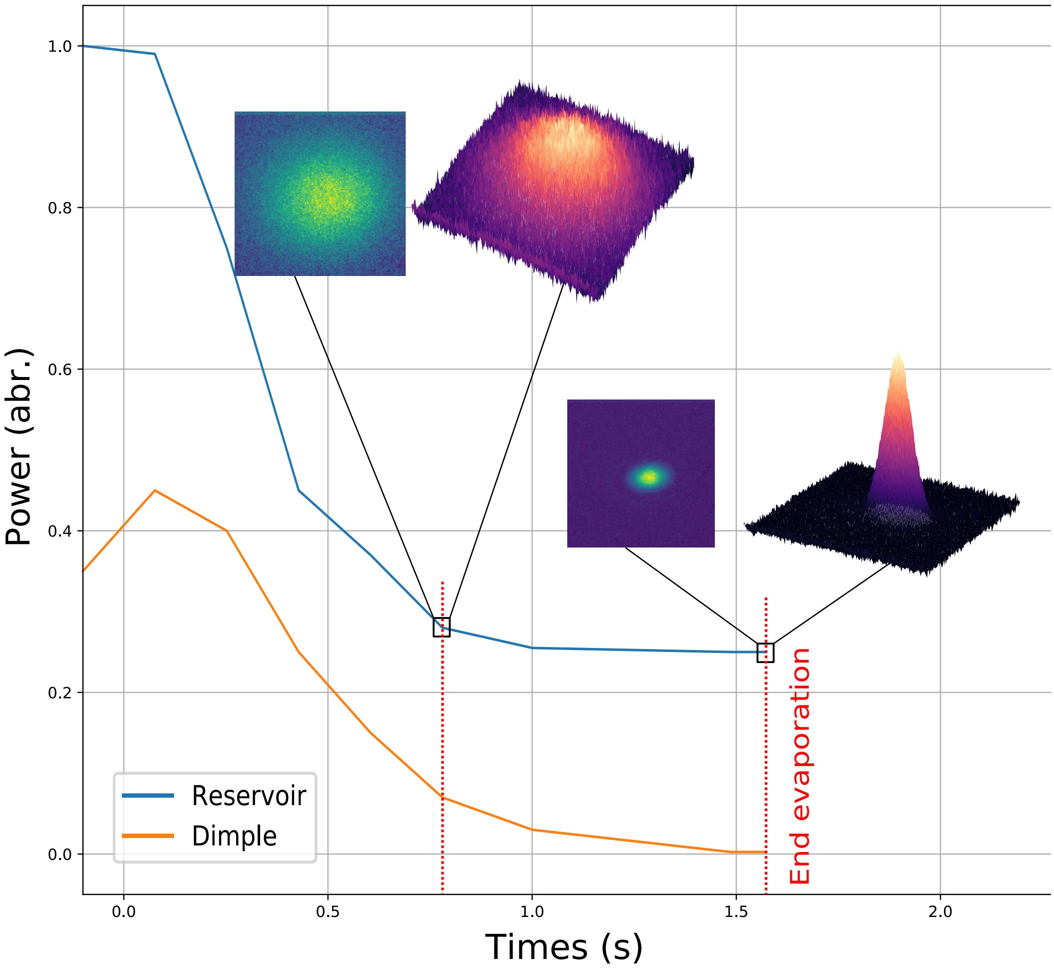

Figure 5.11: The power(normalized) sweep of the reservoir beams and dimple beam. We first trap the atoms in the reservoir beams and then slowly decrease the power in reservoirs simultaneously increase the power in the dimple beam to do efficient evaporative cooling. The pictures shows the phase transfer from a thermal cloud to an 'atom laser' BEC.

5.4.6 Absorption imaging

The principle of absorption imaging is to expose the atom cloud to a resonant beam, which we call a probe beam. In the low saturation regime, where the laser intensity is lower than saturation intensity of the the addressed transition, the ratio between the output and input optical intensity can be written below:

$$\frac{I_{\text{out}}(x,y)}{I_{\text{in}}(x,y)} = e^{-n(x,y)\sigma} \tag{5.31}$$

where σ is the absorption cross section of an atom, and $n(x,y)$ is the density integrated over the laser propagating direction z. So the absorption imaging provides us not only the spatial information of atom cloud but also the total atom number by doing the spatial integral

$$N_a = \frac{1}{\sigma}\int \frac{I_{\text{out}}(x,y)}{I_{\text{in}}(x,y)} dxdy \tag{5.32}$$

Pulse sequence of absorption imaging

A lens system and a CCD camera are combined for absorption imaging. We have three different beams to do this detection: a probe beam derived from the cooling beam, a repump beam and a blow away beam that removes atoms in $|F=2\rangle$. Usually, in our experiment, we have two component atoms in $|F=1\rangle$ and $|F=2\rangle$ at the end. The pulse sequence is shown in Figure 5.12

- For the first image, at a given time t_{det}, the first probe beam derived from the cooling laser is sent to detect atoms in $|F=2\rangle$, we have $I_{\text{F=2}}(x,y)$.
- We put the second pulse 500μs just after the first probe pulse to remove the atoms detected in the first step. Otherwise, these detected atoms will later affect the detection for atoms in $|F=1\rangle$.
- For the second image, time delay around $\text{T}_{\text{D}} \approx 3ms$ (This time delay depends on the size of picture transfer) after the first pulse. We first use a repump pulse to pump atoms from $|F=1\rangle$ to $|F=2\rangle$ then a probe pulse to detect atoms. This gives us $I_{\text{F=1}}(x,y)$.
- For the third image, there are no atoms in the detection area, and we send a probe pulse directly to the camera to have a background $I_{\text{probe}}(x,y)$
- For the fourth image, no light is sent to the camera. We have $I_{\text{background}}(x,y)$
- The density of the atom cloud is given by:

$$\rho_{\text{F=2}} = \frac{1}{\sigma}\int \frac{I_{\text{F=2}} - I_{\text{background}}}{I_{\text{probe}} - I_{\text{background}}} dxdy \tag{5.33}$$

$$\rho_{\text{F=1}} = \frac{1}{\sigma}\int \frac{I_{\text{F=1}} - I_{\text{background}}}{I_{\text{probe}} - I_{\text{background}}} dxdy \tag{5.34}$$

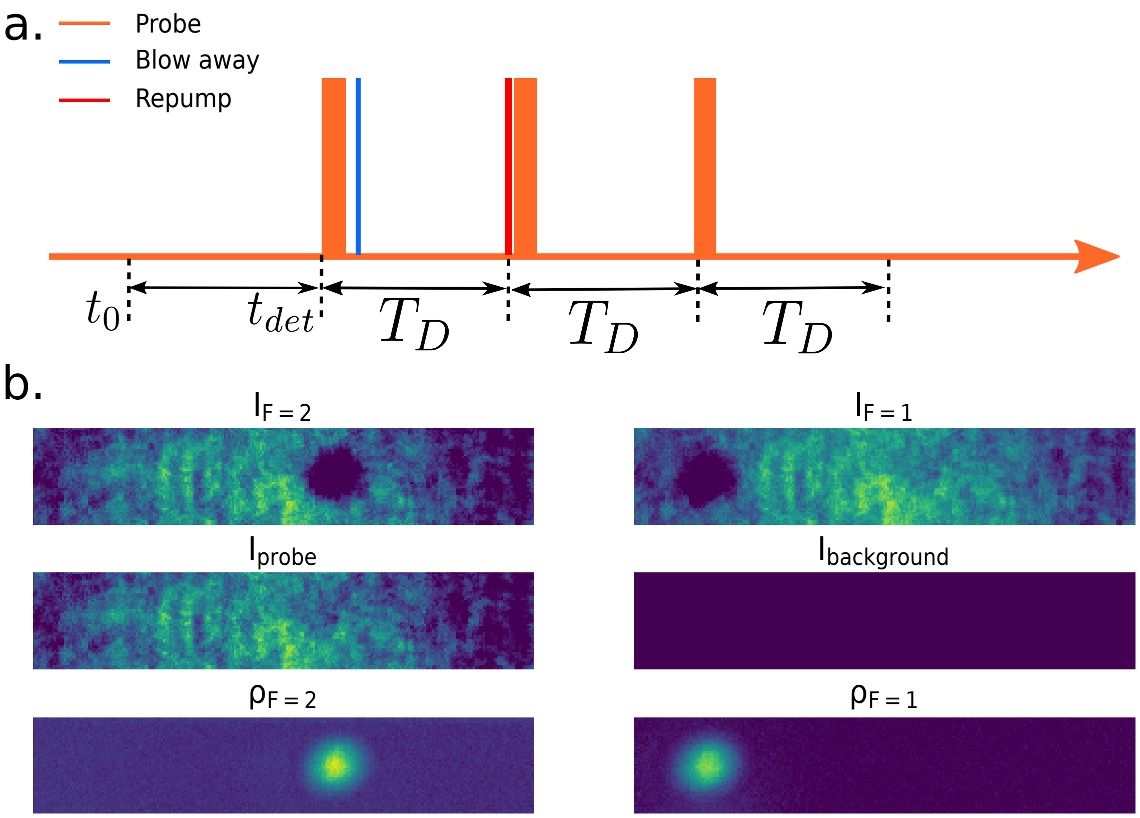

Figure 5.12: The top picture is the pulse sequence of the absorption imaging. The bottom pictures, from left top to right bottom, is the absorption image of atoms in $|F = 2\rangle$, $|F = 1\rangle$, the probe in and background. The last two picture is the density of the atom cloud in $|F = 2\rangle$ and $|F = 1\rangle$ based on Equation 5.33

By using Equation 5.31 we can know how many atoms are in $|F = 1\rangle$ and $|F = 2\rangle$ and get the probability in each state $|i\rangle$ by measuring the ratio $N_i/(N_1 + N_2)$.

5.5 Conclusion

After some efforts to improve the dipole evaporation cooling, we can now produce BECs of 220 000 atoms with an evaporation sequence of 1.7s only. In the end, we obtain an atom cloud with a trapping frequencies (50,100,100) Hz, which corresponds to a final cloud with a temperature around 70 nK.

Currently, our BEC's atom number, temperature, and cloud size are sufficient to perform a measurement of h/m with the BEC. But the atomic interactions in this dense cloud will affect our final result. So before we begin the new measurement, a study of atomic interaction is necessary. To do so, we decided to use the Mach-Zehnder interferometer and observed an interesting phenomena in our experiment (see figure 5.13).

From these pictures, we can see that the atomic interaction in the BEC causes a non-

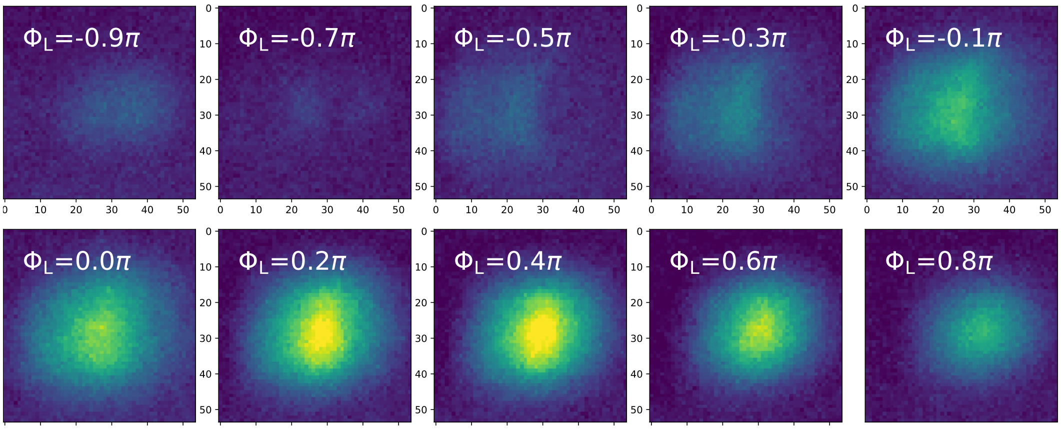

Figure 5.13: The absorption image of the cloud $|F = 1\rangle$ at the end of the atom interferometer when we scan different phase of the last pulse of Mach-Zehnder interferometer ϕ_L

negligible phase shift. Second, we see that the cloud center is moving when we scan the phase of the last pulse of the Mach-Zehnder interferometer. In fact the Equation 5.24 predicts this effect which shows a spatial dependant phase in the wave function. In the next chapter, we will prove that atomic interactions are responsible for both of these effects.

Chapter 6

Phase shift due to interactions in an atom interferometer

Although the BEC has a great potential for metrology, atomic interactions induce a detrimental phase shift that can undermine the benefits of using Bose-Einstein condensates for precision measurements with an atom interferometer. Several groups have studied the effects of interactions theoretically and experimentally to understand their impact on the phase of Bose-Einstein condensates during free evolution[42, 74, 16, 67, 41, 19]. W.D. Philips group showed that after the release from the trapping potential, the BEC expands due to repulsive interactions and develops a non-uniform phase profile [66]. A more recent work studied local modification of the condensate phase due to mutual interactions and showed that modifications occur only in the region where the wave packets overlap[19].

This chapter is devoted to the precise evaluation of the phase shift induced by the atomic interactions at the output of the interferometer. It consists of two parts: In the first part, I will present two models to evaluate the phase shift in the Thomas-Fermi regime: **Model A** is based on the evolution of the phase of the condensate wave function using the GP equation and **model B** uses a perturbation approach and the Feynman path integral method[61].

The second part presents the measurements of this phase shift made by varying some experimental parameters: imbalance of the two populations in the two arms of the interferometer, the trapping frequencies and the release time of the condensate.

6.1 Theoretical Models

Figure **Fig.6.1** shows the light pulse sequence of the atom interferometer used in our theoretical models and experiments. It consists of three counter propagating Raman pulses $\theta - \pi - \theta$. Each pulse induces Raman transition between internal states $|1\rangle$ and $|2\rangle$. We control the atom population imbalance between the two trajectories (A and B) by changing the duration τ_θ of the first pulse (the pulse area is given by $\theta = \Omega\tau_\theta$). Note that the duration of the last pulse is changed as well. Here we define the imbalance factor α:

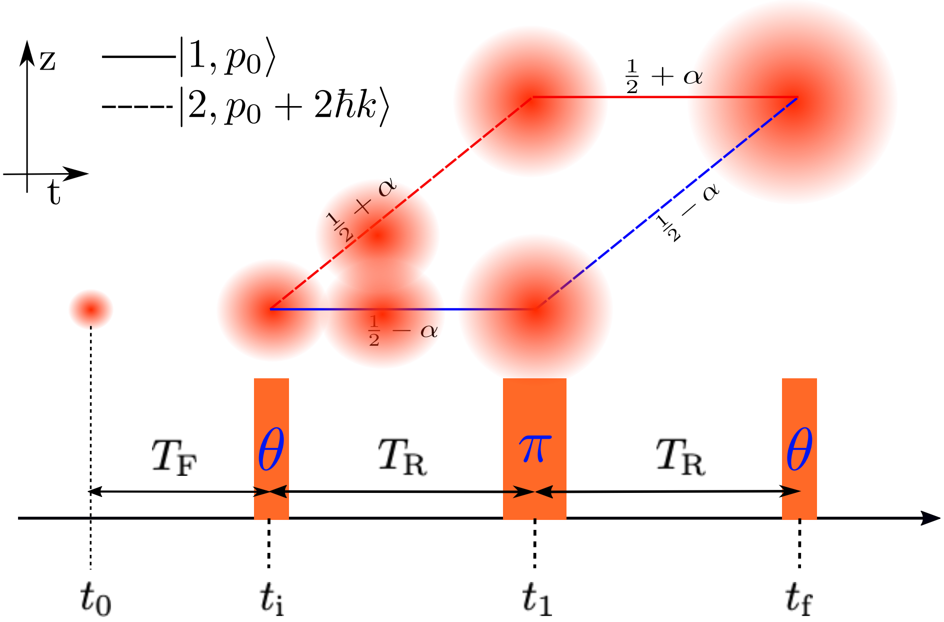

Figure 6.1: At time t_0 we remove the dipole trap, and the BEC begins to free fall. After a free time T_F we apply the pulse sequence $\theta - \pi - \theta$, by detecting the probability of atoms in $|1\rangle$ with different phase of the last pulse we extract the phase shift caused by the atomic interaction.

$$\frac{1}{2} + \alpha = \sin^2\left(\frac{\Omega\tau_\theta}{2}\right) \tag{6.1}$$

where Ω is the effective Rabi frequency.

In our experiment, the atoms are first prepared in $|1\rangle$, which corresponds to the hyperfine state $|F = 1, m_F = 0\rangle$ of the electronic ground state of the rubidium 87. After the first Raman light pulse θ, the BEC is in a coherent superposition of two different states $|1\rangle$ and $|2\rangle$ with amplitude probabilities C_1 and C_2 respectively

$$|\psi\rangle = C_1|1\rangle + C_2|2\rangle$$

Atoms that are transferred by the Raman transition get a recoil velocity $2v_r$, and the two clouds separate. We have two BECs in two different internal states that evolve along two trajectories during the interferometer sequence. Their wave functions φ_1 and φ_2 are governed by the following GP equations:

$$\begin{aligned} i\hbar\frac{\partial\varphi_1}{\partial t} &= \left[-\frac{\hbar^2}{2m}\vec{\nabla}^2 + |C_1|^2 g_{11} N|\varphi_1|^2 + |C_2|^2 g_{12} N|\varphi_2|^2\right]\varphi_1 \\ i\hbar\frac{\partial\varphi_2}{\partial t} &= \left[-\frac{\hbar^2}{2m}\vec{\nabla}^2 + |C_1|^2 g_{12} N|\varphi_1|^2 + |C_2|^2 g_{22} N|\varphi_2|^2\right]\varphi_2 \end{aligned} \tag{6.2}$$

The separation and recombination processes change the overlap of the two atom clouds, so that the interaction potential seen by the atoms also changes with time during the interferometer. All these affect the wave function. Here we make an assumption: Because when we

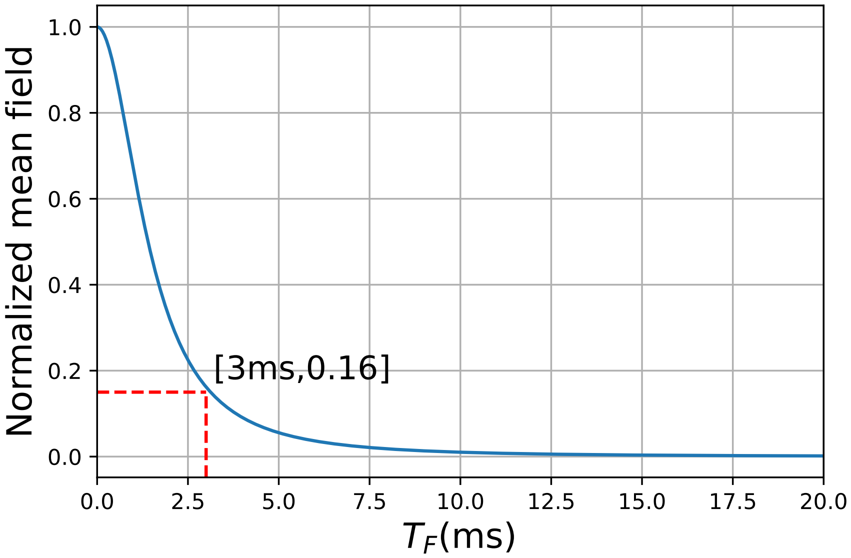

Figure 6.2: The mean field potential at cloud center normalized by the initial mean field. The mean-field vanishes quickly with the expansion of the cloud. When $T_{\mathrm{F}} = 3ms$ there is only 16% mean field left.

apply the atom interferometer, the mean-field decreases a lot and most interaction energy transfers into kinetic energy (almost 85% translate into kinetic energy, see in Figure 6.2), so we can assume that atomic interaction will not change the cloud shape, the way of expansion and center trajectory of each cloud but only introduce a small phase $\phi_k(r,t)$ on the wave function, where k corresponds the different path **A** or **B**. Using the wave function derived from Castin&Dum's model, we can write the wave function of the cloud traveling along path (k) is

$$\varphi_{\mathrm{k}}(r,t) = e^{i\phi_{\mathrm{k}}(r,t)} e^{-i\beta(t)} e^{im\sum_j r_j(t)^2 \dot{\lambda}_j(t)/2\hbar\lambda_j(t)} \frac{\varphi(r,0)}{\sqrt{\lambda_x(t)\lambda_y(t)\lambda_z(t)}} \tag{6.3}$$

Where $\hbar\dot{\beta}(t) = \mu/(\lambda_x(t)\lambda_y(t)\lambda_z(t))$ and $\varphi(r,0)$ is initial wave function when we remove the dipole trap potential that is same as the wave function with the dipole potential which is derived from Equation 5.18 is same for each path.

We want to calculate the phase shift between the two arms of the interferometer induced by the atomic interactions. In the next sections, I will describe two models for evaluating this phase shift.

6.1.1 Model A: Evolution of the phase of the BEC wave function using GP equation

We switch off the dipole trap at time t_0. To calculate the evolution of the phase of the BEC wavefunction we inject the wave function Equation 6.3 in GP equation and we make a coordinate transform $r_{i0} = r_i(t)/\lambda_i(t), i = x, y, z$, in fact here $r_{i0} = r_i(0)$ is the initial position of the particle in the cloud and the center of cloud is zero. We obtain

$$i\hbar\frac{\partial\varphi_k}{\partial t} = \left(-\frac{\hbar^2}{2m}\frac{1}{\lambda_i^2}\partial_{i0}^2 + |C_A|^2 g_{\epsilon_{\mathrm{k}}(t),\epsilon_{\mathrm{A}}(t)}N|\varphi_A|^2 + |C_B|^2 g_{\epsilon_{\mathrm{k}}(t),\epsilon_{\mathrm{B}}(t)}N|\varphi_B|^2\right)\varphi_k \tag{6.4}$$

where the $\epsilon_{\mathrm{A/B}}(t)$ represents the internal state of the atom ($|1\rangle$ or $|2\rangle$) along the respective trajectory at time t, $C_{\mathrm{A/B}}(t)$ is the proportion of atoms in each trajectory, the $g_{\epsilon_{\mathrm{k}}(t),\epsilon_{\mathrm{A}}(t)}$ is the coupling constant between different states and the $\varphi_{\mathrm{A/B}}$ is the wave function along different path.

We then put the wave function Equation 6.3 into Equation 6.4 and by using $\ddot{\lambda}_i = \omega_i^2/(\lambda_i\lambda_x\lambda_y\lambda_z)$ we can get the expression of the phase shift on path k :

$$\begin{aligned}
\hbar\dot{\phi}_k(r,t) = &-\frac{\hbar^2}{2m}\sum_{i=x,y,z}\frac{1}{\lambda_i^2}\left(\frac{\partial}{\partial_{r_{i0}}^2}\phi_k(r_{i0},t) - \frac{\partial}{\partial_{r_{i0}}^2}|\varphi(r_{i0},0)|^2\right)\\
&+\frac{1}{\lambda_x\lambda_y\lambda_z}\left(-\mu + \frac{\sum m\omega_i^2 r_i^2}{2} + g_{11}N|\varphi(r_{i0},0)|^2\right)\\
&-\frac{1}{\lambda_x\lambda_y\lambda_z}\left(g_{11}N|\varphi(r_{i0},0)|^2 - \sum_{l=A,B}|C_l|^2 N g_{\epsilon_k(t),\epsilon_l(t)}|\varphi(r_{i0},0)|^2\right)
\end{aligned}\tag{6.5}$$

The first part of the right hand of the equation is the spatial derivation of the additional phase ϕ_k, which is very small compared with the atomic interaction potential and will be proved later. So here we neglect it first. The last part of the right hand of the equation is the interaction between the two clouds. If we look at the second part, it recalls the time-independent Gross-Pitaevskii Equation (5.20). Then this complex formula can be simplified as below:

$$\begin{aligned}
\hbar\dot{\phi}_{\mathrm{k}}(r,t) = &-\frac{\hbar^2}{2m}\sum_{i=x,yz}\left(\frac{1}{\lambda_i^2} - \frac{1}{\lambda_x\lambda_y\lambda_z}\right)\frac{\partial}{\partial_{r_{i0}}^2}|\varphi(r_{i0},0)|^2\\
&-\frac{1}{\lambda_x\lambda_y\lambda_z}\left(g_{11}N|\varphi(r_{i0},0)|^2 + \sum_{l=A,B}|C_l|^2 N g_{\epsilon_k(t),\epsilon_l(t)}|\varphi(r_{i0},0)|^2\right)
\end{aligned}\tag{6.6}$$

Because in Tomas Fermi regime, the kinetic energy is negligible so that the first part is zero, and we got the final expression of the phase shift

$$\hbar\dot{\phi}_{\mathrm{k}}(r,t) = -\frac{1}{\lambda_x\lambda_y\lambda_z}\left(g_{11}N|\varphi(r_{i0},0)|^2 - \sum_{l=A,B}|C_l|^2 N g_{\epsilon_k(t),\epsilon_l(t)}|\varphi(r_{i0},0)|^2\right) \tag{6.7}$$

This equation shows that if we do not apply any Raman pulses to the atoms and all atoms rest in the initial state $|1\rangle$, it will have only one trajectory left, which is the trajectory B in

Figure 6.1. Then we have $C_B = 1$ for the whole atom interferometer sequence, leading to the result $\phi_k = 0$. We have no additional phase shift because we have no separation and combination in this situation. We will get the same wave function as Castin&Dum's paper [22]. Because in the atom interferometer, what is important is the phase difference between the two paths. Because the first part of the formula is the same for each path, it will be reasonable to remove it at the output of the atom interferometer. In the following calculations, we can neglect this part during the atom interferometer, which allows us to rewrite the phase shift:

$$\hbar\dot{\phi}_{\mathrm{k}}\left(r,t\right) = \frac{1}{\lambda_x(t)\lambda_y(t)\lambda_z(t)} \sum_{l=A,B} |C_l|^2 N g_{\epsilon_k(t),\epsilon_l(t)} |\varphi\left(r_{i0},0\right)|^2 \tag{6.8}$$

Equation 6.8 gives a way to express the phase shift due to the atomic interaction of an atom with a given position $\boldsymbol{r}$ at time $\boldsymbol{t}$. As in the experiment, we detect the total atoms in the atom cloud, so the phase shift measured is a phase shift average over the whole cloud.

The next step, we can apply spatial and time integral to get this average phase shift. The cloud is separated vertically into two when the first Raman pulse is applied, so the distance between the atom in the two clouds can be written as below:

$$\Delta Z(t) = r_{i0}^{\mathrm{A}} - r_{i0}^{\mathrm{B}} = \begin{cases} 2v_{\mathrm{r}}\left(t - t_i\right) & \text{when} \quad t_{\mathrm{i}} < t < t_1 \\ 2v_{\mathrm{r}}\left(t_f - t\right) & \text{when} \quad t_1 < t < t_{\mathrm{f}} \end{cases} \tag{6.9}$$

Based on the (6.8) and (6.9), after the spatial and time integral we have the final phase shift at the output of the interferometer on path k (A or B):

$$\phi_k\left(t\right) = \int dt \sum_l |C_l|^2 \frac{g_{\epsilon_k(t),\epsilon_l(t)}N}{\hbar} \int |\varphi_l\left(r_{i0}^l,0\right)|^2 |\varphi_k\left(r_{i0}^k,0\right)|^2 dr_{i0}^k \tag{6.10}$$

From the equation above (6.10) this phase shift can be understood as the interaction between the two clouds, so the overlap of the two clouds will affect this phase shift a lot. Let's define the normalized vertical distance is $\Delta z = \Delta Z(t)/\left(\lambda_z\left(t\right)Z_{\mathrm{TF}}\right)$ and normalize the three dimension by $r_{i0} = r_i\left(t\right)/\left(\lambda_i\left(t\right)R_{\mathrm{i,TF}}\right), \mathrm{i} = x,y,z$. Then we put the **Eq. 5.18** into the integral (6.10) then we get the final expression of the phase shift:

$$\phi_k = \sum_l |C_l|^2 \omega_{\epsilon_k(t),\epsilon_l(t)} \int dt G\left(t\right) \int_{\frac{\Delta z(t)}{2}}^{1} \Delta z\left(t\right)\left(1-z^2\right)\left(z - \frac{\Delta z\left(t\right)}{2}\right) + \frac{\left(1-z^2\right)^3}{3} dz \tag{6.11}$$

where C_l corresponds portion of atoms stay in each path so $|C_A|^2 = \frac{1}{2}+\alpha$ and $|C_B|^2 = \frac{1}{2}-\alpha$, and we define the atomic interaction frequency

$$\omega_{\epsilon_k(t),\epsilon_l(t)} = 2\pi \frac{g_{\epsilon_k(t),\epsilon_l(t)}\mu^2 X_{\mathrm{TF}} Y_{\mathrm{TF}} Z_{\mathrm{TF}}}{\hbar N g_{11}^2}$$

the function $G\left(t\right) = 1/\left(\lambda_x\left(t\right)\lambda_y\left(t\right)\lambda_z\left(t\right)\right)$ shows how the density dilutes with the expansion of the cloud and the last integral on z dimension, we discuss in two situation:

- When l=k, the cloud overlaps with itself then $\Delta z(t) = 0$, we call it self-interaction, and we define
$$f_{\text{self}}(t) = \int_0^1 \left(1 - z^2\right)^3 /3 = 16/105 \tag{6.12}$$
the phase shift due to the self-interaction can be written as follows:
$$\phi_{\text{k,self}} = |C_k|^2 \omega_{kk} \int f_{\text{self}}(t)\, G(t)\, dt \tag{6.13}$$

- When $l \neq k$, it's the interaction between different clouds then $\Delta z(t) \neq 0$, so we call it mutual-interaction then $\Delta z \neq 0$, and we define
$$f_{\text{mut}}(t) = \frac{\Delta z^7(t)}{1120} - \frac{\Delta z^5(t)}{60} + \frac{\Delta z^3(t)}{6} - \frac{4\Delta z^2(t)}{15} + \frac{16}{105} \tag{6.14}$$
likewise, we have the phase shift due to the mutual interaction :
$$\phi_{\text{k,mut}} = |C_k|^2 \omega_{12} \int f_{\text{mut}}(t)\, G(t)\, dt \tag{6.15}$$

The total phase shift due to the atomic interaction on each path is the sum of the self-interaction and mutual-interaction respectively:

$$\phi_{\text{k,tot}} = \phi_{\text{k,self}} + \phi_{\text{k,mut}} \tag{6.16}$$

The relevant quantity is the phase difference between two trajectories at the output of the interferometer, if we have pulse sequence $\theta - \pi - \theta$ shown in Figure 6.6, the phase difference caused by self and mutual interaction is calculated respectively below:

In the experiment the pulse duration $\tau \approx 40\mu s$ and $T_{\text{R}} \approx 5\text{ms}$, $\tau \ll T_{\text{R}}$ so we can neglect the phase acquisition during the Raman pulse [47].

- The phase difference caused by the self-interaction $(\Delta z = 0)$ is
$$\begin{aligned}\Delta\phi_{\text{self}} &= \phi_{\text{A,self}} - \phi_{\text{B,self}} \\ &= \frac{\omega_{22} - \omega_{11}}{2} \left(\int_{t_i}^{t_1} f_{\text{self}}(t)\, G(t) - \int_{t_1}^{t_{\text{f}}} f_{\text{self}}(t)\, G(t) \right) \\ &+ \alpha\left(\omega_{22} + \omega_{11}\right) \int_{t_i}^{t_{\text{f}}} f_{\text{self}}(t)\, G(t)\end{aligned} \tag{6.17}$$
where t_i and t_{f} is the start time and end time of the atom interferometer.

- The phase difference caused by the the mutual-interaction $(\Delta z \neq 0)$ is
$$\begin{aligned}\Delta\phi_{\text{mut}} &= \phi_{\text{A,self}} - \phi_{\text{B,self}} \\ &= -2\alpha\omega_{12} \left(\int_{t_i}^{t_{\text{s}}^{max}} G(t)\, f_{\text{mut}}(t) + \int_{t_{\text{c}}^{min}}^{t_{\text{f}}} G(t)\, f_{\text{mut}}(t) \right)\end{aligned} \tag{6.18}$$

The first and second part shows the separation and recombination of the clouds. The corresponding time t_s^{max} is when the two clouds are totally separated, and t_c^{min} is when the two clouds begin recombining. They are calculated from:

$$\begin{aligned} t_{\mathrm{s}}^{max} &: \quad 2Z_{\mathrm{TF}}\lambda_z\left(t_{\mathrm{s}}\right) = 2v_{\mathrm{r}}\left(t_{\mathrm{s}} - t_{\mathrm{i}}\right) \\ t_{\mathrm{c}}^{min} &: \quad 2Z_{\mathrm{TF}}\lambda_z\left(t_{\mathrm{c}}\right) = 2v_{\mathrm{r}}\left(t_{\mathrm{f}} - t_{\mathrm{c}}\right) \end{aligned} \tag{6.19}$$

The total phase difference at the output the interferometer is

$$\Delta\phi_{\mathrm{tot}} = \Delta\phi_{\mathrm{self}} + \Delta\phi_{\mathrm{mut}} \tag{6.20}$$

This result is same as what shown in the previous result of our group [47], the difference is that we assumed the atoms are in a Gaussian distribution before while in this calculation we assume the wave function of the BEC is given by Castin & Dum formula [22].

In this model, the effect due to the mutual interaction is overestimated because the separation and recombination times are also vertical position z-dependant, which means that the atoms at a different position in the cloud will have different separation and recombination times. This will be explained in the next model. But this little effect can be neglected between these two models under certain situations that are validated in our experiment. The comparison of the two models will prove this.

6.1.2 Model B: Feynman path integral approach

In the second model, instead of doing spatial integral of the cloud to get the average phase shift of the whole cloud, we calculate the phase acquisition of each atom at a given position $\mathbf{r} = (x, y, z)$ in the cloud by doing the Feynman path integral $S_{\mathrm{A/B}}$ along each arm of the atom interferometer. Then we can calculate not only the average phase shift of the whole cloud but also the local phase gradient of the cloud. More details of this model are shown in Appendix 6.5:

The Feynman path integral method states that: An initial wave packet with a phase $\phi\left(\mathbf{r}\left(t_0\right), t_0\right)$ at time t_0, the phase at time t can be calculated by integrating the Lagrangian $\mathcal{L}$ along the classical trajectory $r\left(t\right)$:

$$\phi\left(\mathbf{r}\left(t\right), t\right) - \phi\left(\mathbf{r}\left(t_0\right), t_0\right) = \frac{S\left(\mathcal{L}\right)}{\hbar} = \frac{1}{\hbar}\int_{t_0}^{t} \mathcal{L}\left(\dot{\mathbf{r}}\left(t\right), \mathbf{r}\left(t\right), t\right) \mathrm{d}t \tag{6.21}$$

with

$$\mathcal{L}\left(\dot{\mathbf{r}}\left(t\right), \mathbf{r}\left(t\right), t\right) = \frac{1}{2}m\dot{\mathbf{r}}^2\left(t\right) - V\left(\mathbf{r}, t\right) \tag{6.22}$$

V is the potential experienced by an atom of mass m. The trajectory should match the initial velocity of the cloud ($\dot{\mathbf{r}}\left(t_0\right) = -i\hbar\nabla\phi$).

The Lagrangian of our system is given by

$$\mathcal{L}\left(\dot{\mathbf{r}}\left(t\right), \mathbf{r}\left(t\right), t\right) = \frac{1}{2}m\dot{\mathbf{r}}^2\left(t\right) - W\left(\mathbf{r}\left(t\right), t\right) - V_{\mathrm{MF}}\left(\mathbf{r}\left(t\right), t\right) \tag{6.23}$$

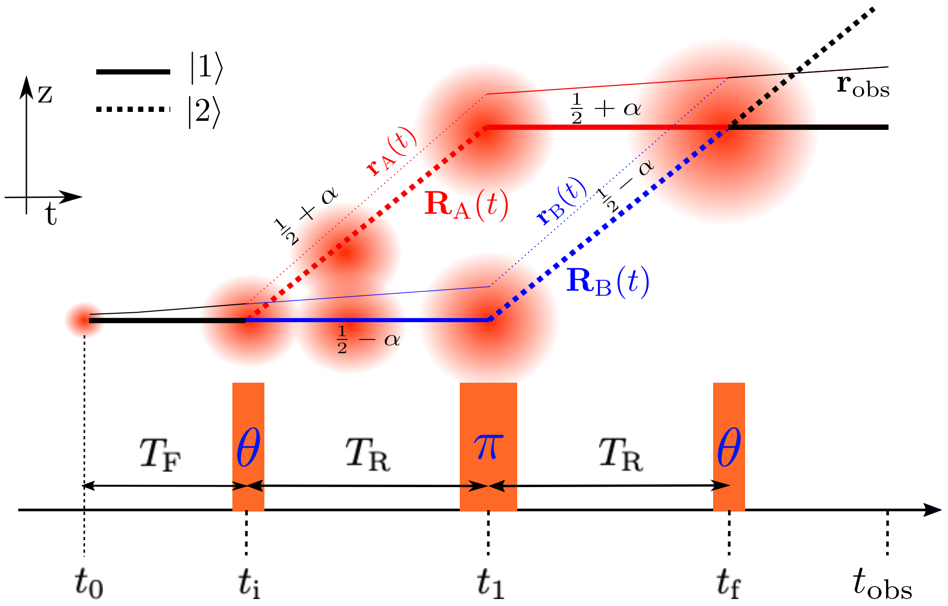

Figure 6.3: In red and blue represents trajectory $\boldsymbol{A}$ and trajectory $\boldsymbol{B}$ respectively. Solid line state $|1\rangle$, dashed line state $|2\rangle$. Thick line : trajectories $\boldsymbol{R}_{A/B}$ of the center of mass of the atomic wave packet. Thin line : trajectory $\boldsymbol{r}_{A/B}$ used to integrate the Lagrangian for a given position $\boldsymbol{r}_{\text{ref}}$ in the cloud.

Where the first term is the kinetic energy of atom of mass m, the motion of it is explained in Castin & Dum's model $\dot{\boldsymbol{r}}_{\text{A/B}} = \dot{R}_{\text{A/B}} + \boldsymbol{r}_{\text{ref}}(t_0)\dot{\lambda}_i$.

The second part $W(\mathbf{r}(t), t)$ is an an effective potential that presents the interaction with the Raman pulses. For the three pulses interferometer of figure 6.3, this potential is given for each path by:

$$W_A(\mathbf{r}, t) = \hbar\left((\mathbf{k}_{\text{eff}} \cdot \mathbf{r}_{\mathbf{A}}(t_i) - \omega t_i) - (\mathbf{k}_{\text{eff}} \cdot \mathbf{r}_{\mathbf{A}}(t_1) - \omega t_1)\right) \tag{6.24}$$

$$W_B(\mathbf{r}, t) = \hbar\left((\mathbf{k}_{\text{eff}} \cdot \mathbf{r}_{\mathbf{B}}(t_1) - \omega t_1) - (\mathbf{k}_{\text{eff}} \cdot \mathbf{r}_{\mathbf{B}}(t_f) - \omega t_f)\right) \tag{6.25}$$

Where $\mathbf{k}_{\text{eff}}$ is the wave vector of the Raman laser beam, When an atom performs a Raman transition from $|1\rangle$ to $|2\rangle$, the effective phase of the laser is added to the phase of its wave function. It is subtracted when the atom is transferred from state $|2\rangle$ to $|1\rangle$. With this effective potential, the trajectory that extremizes the action, accounts for the recoil induced by each Raman transition.

The last part is the atomic interaction potential. In the mean-field approximation, the interaction potential is proportional to the cloud density.

$$\rho_{\text{A/B}}\left(\mathbf{r}_{\text{A/B}}, t\right) = c_{\text{A/B}}(t)\, N \rho_{\text{ref}}\left(\mathbf{r}_{\text{ref}}, t\right) \tag{6.26}$$

where ρ_{ref} is derived from Equation 5.18 and $c_{\text{A/B}}$ is portion of atoms stays in the path. In the configuration depicted in figure 6.3, $c_A = 1/2 + \alpha$ and $c_B = 1/2 - \alpha$ where α is imbalance in population between the two arms of the interferometer.

In our experiment, the Raman transition couples two internal states, namely $|2\rangle$ and $|1\rangle$, and an atom after the first Raman pulse is in a superposition of two wave packets that propagate along the reference trajectories $\boldsymbol{r}_A$ and $\boldsymbol{r}_B$. To calculate the phase in our interferometer, we should consider that the total mean field experienced by an atom in path k is the sum of the mean field induced by the atoms in the same internal state from its atomic cloud (the so-called self-interaction) and the one induced by the atoms in the different internal state in another path l (the so-called mutual interaction) (see figure 6.3). It can be written as:

$$V_{\mathrm{MF,k}}\left(\mathbf{r}_k, t\right)=\sum_l N g_{\epsilon_k(t), \epsilon_l(t)} \rho_l\left(\mathbf{r}_l, t\right) \tag{6.27}$$

During the atom interferometer sequence shown in Figure 6.3, at different time the mean field potential felt by the atom in different path is expressed below:

$$\begin{aligned} &\text{For } t_{\mathrm{i}}<t<t_2 \\ V_{\mathrm{A}}\left(\boldsymbol{r}_{\mathrm{A}}, t\right) &= N c_A g_{22} \rho_{\mathrm{ref}}(\boldsymbol{r}, t)+N c_B g_{21} \rho_{\mathrm{ref}}(\boldsymbol{r}+\boldsymbol{\Delta} R(t), t) \\ V_{\mathrm{B}}\left(\boldsymbol{r}_{\mathrm{B}}, t\right) &= N c_B g_{11} \rho_{\mathrm{ref}}(\boldsymbol{r}, t)+N c_A g_{12} \rho_{\mathrm{ref}}(\boldsymbol{r}-\boldsymbol{\Delta} R(t), t) \end{aligned} \tag{6.28}$$

$$\begin{aligned} &\text{For } t_2<t<t_{\mathrm{f}} \\ V_{\mathrm{A}}\left(\boldsymbol{r}_{\mathrm{A}}, t\right) &= N c_A g_{11} \rho_{\mathrm{ref}}(\boldsymbol{r}, t)+N c_B g_{21} \rho_{\mathrm{ref}}(\boldsymbol{r}+\boldsymbol{\Delta} R(t), t) \\ V_{\mathrm{B}}\left(\boldsymbol{r}_{\mathrm{B}}, t\right) &= N c_B g_{22} \rho_{\mathrm{ref}}(\boldsymbol{r}, t)+N c_A g_{12} \rho_{\mathrm{ref}}(\boldsymbol{r}-\boldsymbol{\Delta} R(t), t) \end{aligned} \tag{6.29}$$

We want to calculate the phase difference at a given observation position $\mathbf{r}_{\mathrm{obs}}$ and time t_{obs} (see figure6.3), the spatially dependent phase difference between the two wave packets is given by :

$$\Delta \phi\left(\mathbf{r}_{\mathrm{obs}}, t_{\mathrm{obs}}\right)=\frac{1}{\hbar} \int_{t_0}^{t_{\mathrm{obs}}}\left(\mathcal{L}_{\mathcal{A}}\left(\dot{\mathbf{r}}_A, \mathbf{r}_A, t\right)-\mathcal{L}_{\mathcal{B}}\left(\dot{\mathbf{r}}_B, \mathbf{r}_B, t\right)\right) d t \tag{6.30}$$

Based on the assumption we made before: Because when we apply the atom interferometer, the mean field decreases a lot, and most interaction energy has already transferred into kinetic energy (almost 90% mean field energy is transferred into kinetic energy when free fall time $T_{\mathrm{F}}=3\,\mathrm{ms}$), so we can assume that the cloud expansion in two clouds is same, so does the two cloud shape $\boldsymbol{r}_{\mathrm{ref}}^{\mathrm{A}}=\boldsymbol{r}_{\mathrm{ref}}^{\mathrm{B}}$. we can write $\boldsymbol{r}_{A/B}(t)=\boldsymbol{R}_{A/B}(t)+\boldsymbol{r}_{\mathrm{ref}}(t)$. In the absence of any perturbation, the two trajectories are symmetric, and the total phase shift at the output of the atomic interferometer is zero. In the first order, the total phase shift could be calculated by integrating the perturbation along the unperturbed trajectories [61]. These trajectories overlap for $t<t_i$ and $t>t_f$ and the potential is the same t(atoms are in the same state), we can therefore restrict the integral to $t_i<t<t_f$ and

$$\Delta \phi\left(\mathbf{r}_{\mathrm{obs}}, t_{\mathrm{obs}}\right)=\frac{1}{\hbar} \int_{t_i}^{t_{\mathrm{f}}}\left(\mathcal{L}_{\mathcal{A}}\left(\dot{\mathbf{r}}_A, \mathbf{r}_A, t\right)-\mathcal{L}_{\mathcal{B}}\left(\dot{\mathbf{r}}_B, \mathbf{r}_B, t\right)\right) d t \tag{6.31}$$

By doing the integral above, we will find out that the kinetic and laser phase part is canceled out at the end of the interferomter. So the final phase difference is written as the integral of the mean field potential:

$$\Delta\phi\left(\boldsymbol{r}_{\text{obs}}\right)=\int_{t_i}^{t_f}\left(V_A^{\text{pert}}\left(\boldsymbol{R}_A\left(t\right)+\boldsymbol{r}_{\text{ref}}\left(t\right),t\right)-V_B^{\text{pert}}\left(\boldsymbol{R}_B\left(t\right)+\boldsymbol{r}_{\text{ref}}\left(t\right),t\right)\right)dt \tag{6.32}$$

By separating contributions from the mutual and the self-interaction, we obtain

$$\Delta\Phi^{\text{self}}\left(r_{\text{obs}}\right) = \frac{1}{\hbar}N\alpha\left(g_{11}+g_{22}\right)\int_{t_{\text{i}}}^{t_{\text{f}}}\rho_{\text{ref}}\left(\boldsymbol{r},t\right)\,\mathrm{d}t+\frac{1}{\hbar}\frac{N}{2}\delta g\left[\int_{t_{\text{i}}}^{t_1}\rho_{\text{ref}}\left(\boldsymbol{r},t\right)\,\mathrm{d}t-\int_{t_1}^{t_{\text{f}}}\rho_{\text{ref}}\left(\boldsymbol{r},t\right)\,\mathrm{d}t\right] \tag{6.33}$$

$$\begin{aligned}\Delta\Phi^{\text{mut}}\left(\boldsymbol{r}_{\text{obs}}\right) &= \frac{1}{\hbar}Ng_{21}\left(\frac{1}{2}-\alpha\right)\left[\int_{t_{\text{i}}}^{t_{\text{s}}^A}\rho_{\text{ref}}\left(\boldsymbol{r}+\boldsymbol{\Delta}R\left(t\right),t\right)\,\mathrm{d}t+\int_{t_{\text{c}}^A}^{t_{\text{f}}}\rho_{\text{ref}}\left(\boldsymbol{r}+\boldsymbol{\Delta}R\left(t\right),t\right)\,\mathrm{d}t\right]\\ &- \frac{1}{\hbar}Ng_{12}\left(\frac{1}{2}+\alpha\right)\left[\int_{t_{\text{i}}}^{t_{\text{s}}^B}\rho_{\text{ref}}\left(\boldsymbol{r}-\boldsymbol{\Delta}R\left(t\right),t\right)\,\mathrm{d}t+\int_{t_{\text{c}}^B}^{t_{\text{f}}}\rho_{\text{ref}}\left(\boldsymbol{r}-\boldsymbol{\Delta}R\left(t\right),t\right)\,\mathrm{d}t\right]\end{aligned} \tag{6.34}$$

where $\alpha=\left|c_A\left(t\right)-c_B\left(t\right)\right|/2$ is the population imbalance between the two arms of the interferometer and $\delta g=g_{22}-g_{11}$, for rubidium $\left|\left(a_{22}-a_{11}\right)/a_{11}\right|$ is around 6%, which is measured in our experiment and will be shown at the end of this chapter. The boundaries of the integrals (6.33) and (6.34) account for the finite extension and separation of the two interfering clouds: t_{s}^A (resp. t_{s}^B) is the separation time when atom on trajectory A (resp. B) leaves the overlap zone and t_{c}^A (resp. t_{c}^B) is the recombination time when atom on trajectory A (resp. B) enters the overlap zone(seen in Figure 6.4). They depend on the expansion and the separation velocities of the two interfering condensates.

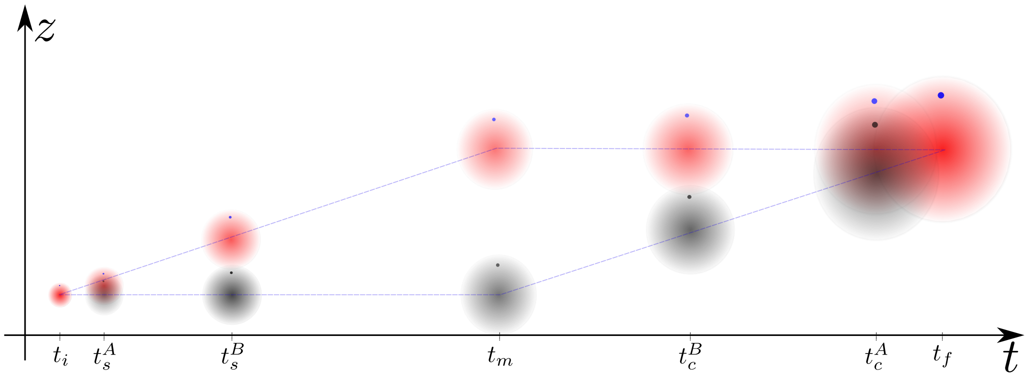

Figure 6.4: The trajectory of each cloud. The different separation and recombination times are shown for an atom with a given position z. In this picture, we show the z>0, but as the cloud is symmetric so the same situation can be used for the atom in z<0

And these times satisfy the equations below:

$$
\begin{aligned}
t_{\mathrm{s}}^{A} &: \left(z_{\mathrm{TF}}-z_0\right)\lambda_z\left(t_{\mathrm{s}}^{A}\right)=2v_{\mathrm{r}}\left(t_{\mathrm{s}}^{A}-t_{\mathrm{i}}\right)\\
t_{\mathrm{s}}^{B} &: \left(z_{\mathrm{TF}}+z_0\right)\lambda_z\left(t_{\mathrm{s}}^{B}\right)=2v_{\mathrm{r}}\left(t_{\mathrm{s}}^{B}-t_{\mathrm{i}}\right)\\
t_{\mathrm{c}}^{A} &: \left(z_{\mathrm{TF}}-z_0\right)\lambda_z\left(t_{\mathrm{c}}^{A}\right)=2v_{\mathrm{r}}\left(t_{\mathrm{f}}-t_{\mathrm{c}}^{A}\right)\\
t_{\mathrm{c}}^{B} &: \left(z_{\mathrm{TF}}+z_0\right)\lambda_z\left(t_{\mathrm{c}}^{B}\right)=2v_{\mathrm{r}}\left(t_{\mathrm{f}}-t_{\mathrm{c}}^{B}\right)
\end{aligned}
\tag{6.35}
$$

Two models comparison

Two simulations are written in python to simulate this effect using these two different models. We put the same initial parameters for each model and changed the free-fall time to see the phase difference at the output of the interferometer, the simulation results are shown below:

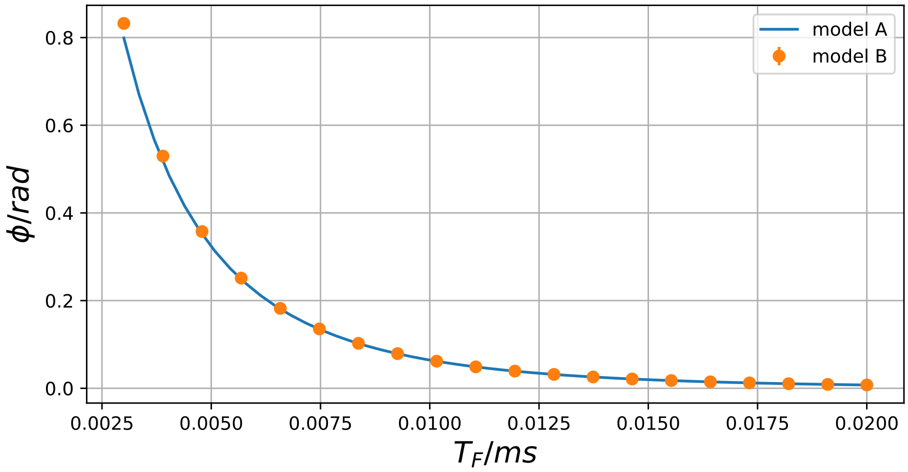

Figure 6.5: The initial parameters are $\theta = 0.3\,\pi$, $[50\,,105\,,105\,]$Hz, $N_a = 180,000$. The points and solid line are the simulation results from model A and model B respectively.

From Figure 6.5 we can see that when the free-fall time is short $T_f = 3\,\mathrm{ms}$ these two models have a small difference. Comparing Equation 6.19 and Equation 6.35, it's easy to find out $t_{\mathrm{s}}^{A} < t_{\mathrm{s}}^{max}$ and $t_{\mathrm{c}}^{A} > t_{\mathrm{c}}^{min}$, so the reason is that because in model A the time integral scale of mutual interaction is overestimate and the $\Delta\phi_{mut}$ and $\Delta\phi_{self}$ they have opposite sign. Hence, model B gives a slightly bigger value when the free fall is small where the atomic interaction magnitude is big. But when $T_F > 3ms$, these two modes give the same value as the atomic interaction extinguishes quickly with time. In our experiment, because of some limitations of the experimental setup, the minimum free-fall time is $3\,\mathrm{ms}$, so in our experiment, we can say these two models do not have any difference.

This result shows that the phase of the Castin & Dum's model (model $\boldsymbol{A}$) can be recovered from the method of Feynman path integral (model $\boldsymbol{B}$). Model B also gives us a way to study the local phase of the cloud, which is shown in next section section 6.3.

6.1.3 Principle of phase measurement

After switching off the trapping laser, the atom cloud will fall due to gravity. In the meantime, the repulsive force caused by the atomic interaction makes the cloud expand.

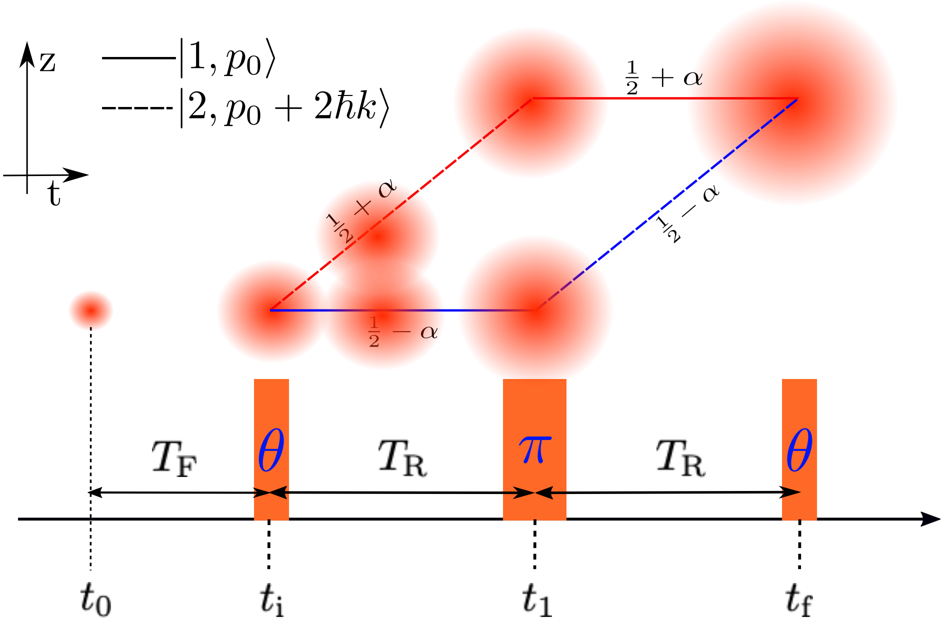

Figure 6.6: At time t_0 we remove the dipole trap, and the BEC begins to free fall. After a free time T_F we apply the first θ raman pulse to begin our atom interferometer.

We know that the atomic interaction potential will convert into kinetic energy as time goes by. So in the experiment, we can variate the atomic interaction magnitude when the cloud enters the atom interferometer by changing the free-fall time T_F. From the Equation 6.17 and Equation 6.18 we know that the final phase shift varies with unbalance factor α. So we use 5 different pulse duration τ_θ from $.3\pi$ to 0.7π to change the imbalance between the two arms to verify whether our theoretical models are correct or not.

We detect the atoms in $|F = 1\rangle$ and $|F = 2\rangle$ at fixed observation time $t_{\text{obs}} = 33\,\text{ms}$ by absorption imaging. We make this measurement by scanning the laser phase of the last pulse ϕ_L. Then we integrate image over yz axis (x axis being the direction of the probe laser beam). From the number of atom in each state $|1\rangle$ and $|2\rangle$, we deduce the fraction of atom in $F = 1$ and then the probability $P(F = 1)$ to detect atoms in $|1\rangle$.

Then we repeat the experiment with different Φ_L from $-\pi$ to π to get the atomic fringes signal. By fitting this signal by a sinusoidal function, we get the phase shift due to the atomic interaction (seen in the orange curve in Figure 6.7)

$$P(F = 1) = \frac{1-\alpha^2}{2}\left(1 + \cos(\Delta\phi - \Phi_L)\right) \tag{6.36}$$

Before running the experiment, the trapping frequency is measured as $[50\,,115\,,115\,]\text{Hz}$, and this critical parameter is set in our simulation codes. As we discussed before, there is

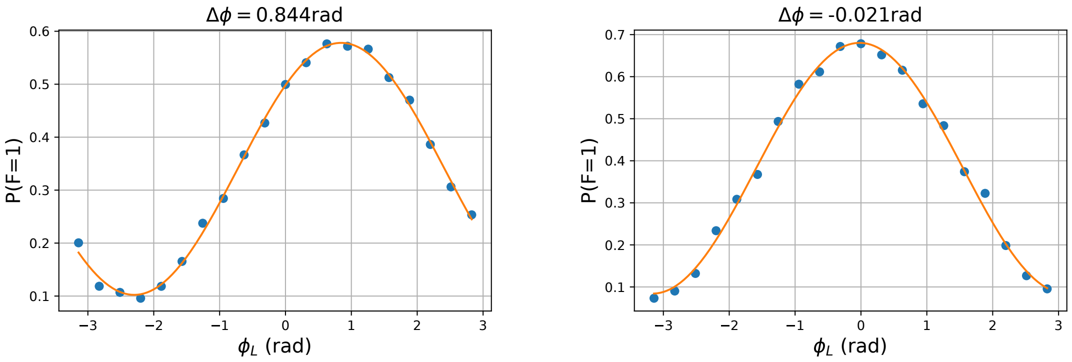

Figure 6.7: The points are the experimental data and the orange solid curves is the sinusoid fit curves. Both figures are manipulated with $\theta = 0.3\,\pi$ but with different free fall time(Left: $3\,\mathrm{ms}$, Right: $20\,\mathrm{ms}$). Their fringe centers are written on the top of each figure.

no difference between models A and B. So we use model A to do the simulation because it is much faster than model B.

Then experiment is run randomly with different $[\theta, T_{\mathrm{F}}]$. The whole experimental data and simulation results are shown in Figure 6.8.

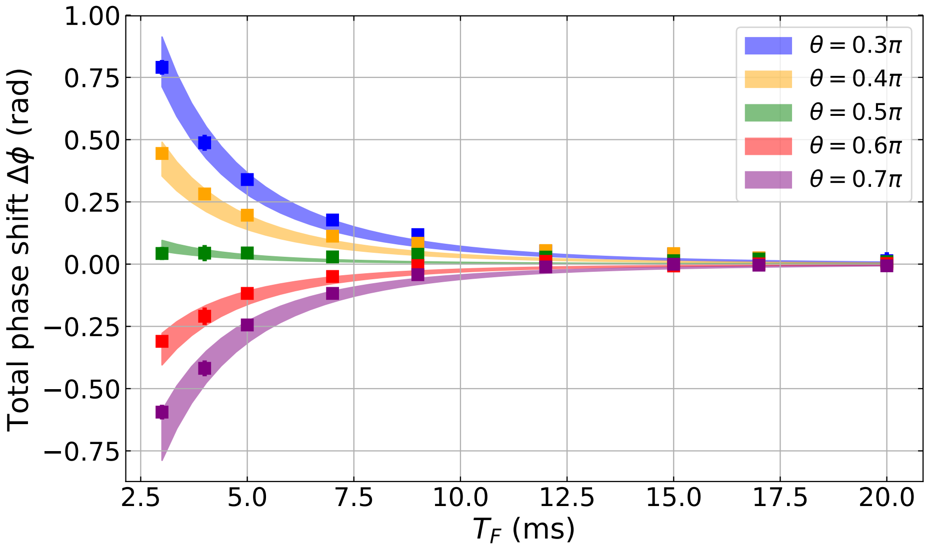

Figure 6.8: Total phase shift accounting for both mutual and self interactions as a function of the release time T_{F}, for different values of the Raman pulse area θ (from $0.3\,\pi$ to $0.7\,\pi$), with T_{R} = $6\,\mathrm{ms}$. The square points are the experimental data with each point is an average of 7 experimental points. The shaded curve is the range of calculated total interaction phase shift, accounting for uncertainty on the pulse area and the trapping frequencies.

Because our Raman lasers are phase-locked and the phase of the last laser pulse ϕ_L is scanned, so the effective phase felt by the atom is $\phi_{\mathrm{eff}} = \phi_{\mathrm{R1}} - \phi_{\mathrm{R2}} = -\phi_{\mathrm{L}}$. That is why in this picture, this phase shifts $\Delta\phi$ has the opposite sign of the theoretical values, where the phase shift should be negative (positive) when $\theta < 0.5\pi$ ($\theta > 0.5\pi$) in our model.

From **Fig.** 6.8, it shows us that the theoretical model works very well with experiment. We can conclude:

First, the mean-field effect vanishes quickly with the fall time increases. After 20ms, the interaction effect is weak (20 mrad left) and can be neglected. So in the experiment, we can leave the cloud to expand for a longer time to reduce the effect.

Second even $\alpha = 0$, we still can see a clear phase shift due to the mean-field. This is because of the difference between scattering length a_{11} and a_{22} and because the free-fall time is small, so the atomic potential is powerful ($T_\mathrm{F} = 3\,\mathrm{ms}$)that makes the part $\omega_{22} - \omega_{11} \neq 0$ in $\Delta\phi_{self}$ is no longer negligible.

6.2 Effect of the trapping frequency

We always think that the higher atomic interaction, the more phase shift generated at the end, which seems right in Fig.6.8 where this effect decreases with the free-fall time. But is that always true?

Instead of changing the free-fall time to variate the magnitude of the atomic interaction, this time, we keep the atom number constant and change the trapping frequency of the dipole trap to change the atomic interaction magnitude in the cloud. The way is shown in Figure 6.9.

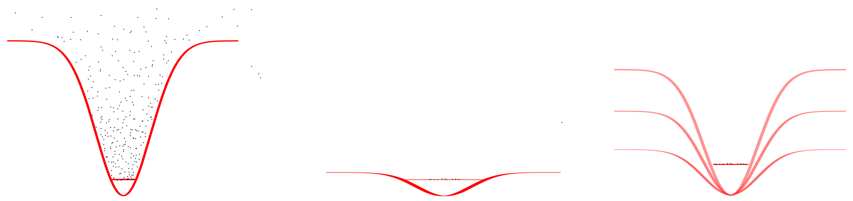

Figure 6.9: In the experiment, we first do evaporation cooling to a fixed potential depth (mid picture) and let it stabilize for a while, then change the dimple dipole laser power to variate the trapping frequency (the last picture) without changing the atom number.

This way, we can change vertical trapping frequency from $80\,\mathrm{Hz}$ to $200\,\mathrm{Hz}$ with atom number fluctuates between 120,000 and 150,000. Then we do the same pulse sequence $\theta - \pi - \theta$ shown in Figure 6.6 with fixed $\theta = 0.35\pi$ and measure the phase shift due to the atomic interaction using the same way mentioned in before.

From theFigure 6.10, the result is contra intuitive. The phase shift does not simply increase with the trapping frequency but first increases with the trapping frequency and then decreases with the trapping frequency.

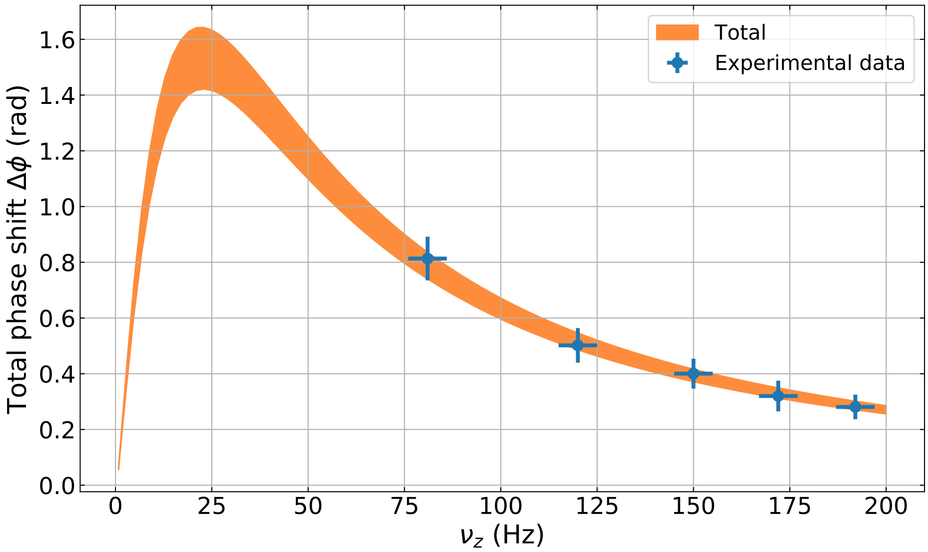

Figure 6.10: Variation of interaction phase shift with the vertical trapping frequency ν_z. The blue points are the experimental data, each points is average of 50 repetitions. The shaded orange curve is the range of calculated total interaction phase shift, accounting for uncertainty on the number of atoms and the trapping frequencies. Parameters are $T_\mathrm{F} = 3\,\mathrm{ms}$, $T_\mathrm{R} = 6\,\mathrm{ms}$ and $\theta = 0.35\,\pi$.

In order to understand this, the Figure 6.11 plots the self-interaction and mutual interaction variation with trapping frequency in model A.

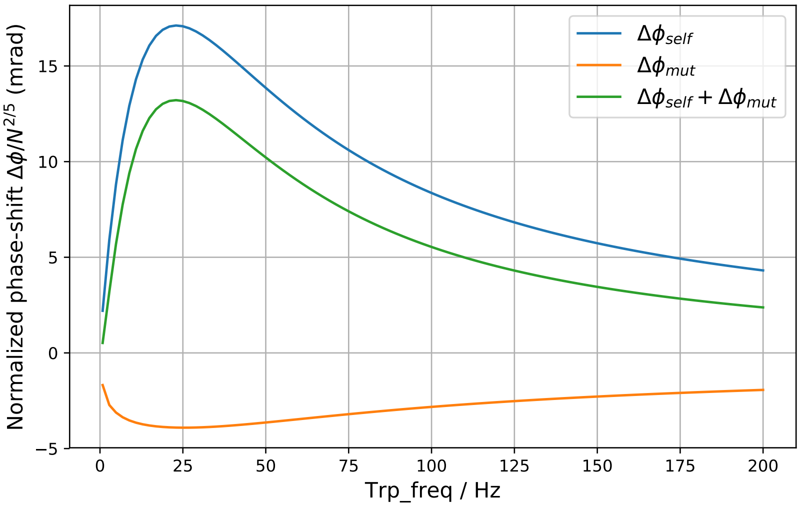

Figure 6.11: The self interaction and mutual interaction changes with the trapping frequency.

When the trapping frequency is infinitely small $\omega_i \approx 0$, the mean-field potential is also infinitely small, which means $\mu \approx 0$. That is why at the beginning, we do not see any atomic effect at the end of the atom interferometer. With the increase of the trapping frequency, the mean-field $\mu \propto \bar{\omega}^{(7/5)}, \bar{\omega} = (\omega_x \omega_y \omega_z)^{(1/3)}$ will increases immediately. Although the expansion of the cloud will increase with the trapping frequency (seen in Figure 5.2) the $\lambda_i(t)$ can be approximated as $\sqrt{1+(\omega_i t)^2}$, this vanishing time of the atomic interaction $t \propto 1/\omega_i$ is big when the trapping frequency is very small, so we can approximate during the interferometer the cloud size doesn't change. This results in both the self interaction and mutual interaction increase.

But when the trapping frequency is minor, the expansion of the cloud is slow while the split speed between the two clouds is always the same $2v_r$, so these two clouds will separate very quickly. Hence, in the self interaction, the time integral range is bigger than in mutual interaction, then the magnitude of self interaction increases quicker than in mutual interaction giving rise to the $\Delta\phi_{tot}$ increasing at the very beginning of this picture.

After then, the trapping frequency increases more and more, and the expansion of the cloud gets quicker and quicker, so the mean-field decreases very quickly. This effect decreases with the trapping frequency after one point and infinitely goes to zero.

6.3 Phase gradient in the cloud

We discussed the average phase on the whole cloud, but as we discussed in the model **B** when the cloud is separating or combining the atom at the different positions will see different atomic interactions, which means that this phase should be spatial dependent. The motion of the cloud when we scan the phase of the last pulse (seen in Fig.5.13) is proof of the phase gradient of the cloud.

Because model A cannot simulate this phenomenon, we use model B to study it.

The simulation result shown in Fig.6.12 gives us the same cloud motion in the experiment: the cloud center moves when we scan the phase of the last pulse, which means the phase of the cloud is not homogeneous. Then we extract the phase gradient of the experiment data and simulation result and show them below:

From this picture the simulation result fits not bad with the experimental data, the small disagreement (for the area z<0 in $\theta = 0.3\pi$) is due to the second π pulse can't transfer all the atoms into another state. So after this π pulse there is still some atoms rest in the previous state.

From the experimental and simulation results, they have a not bad agreement and we can find out that the phase gradient is a parabola function which is related with the imbalance factor α. The simulation results shows that the ratio when

$$\mu \approx 10^7 \times \frac{\hbar^2}{2m}\frac{\partial^2\phi(r,t)}{\partial^2 r} \gg \frac{\hbar^2}{2m}\frac{\partial^2\phi(r,t)}{\partial^2 r} \quad \text{when} \quad \alpha = 0.5$$

$$\mu \approx 3\times 10^5 \times \frac{\hbar^2}{2m}\frac{\partial^2\phi(r,t)}{\partial^2 r} \gg \frac{\hbar^2}{2m}\frac{\partial^2\phi(r,t)}{\partial^2 r} \quad \text{when} \quad \alpha = 0.3$$

so that the assumption in the model A: $\frac{\partial}{\partial_r^2}\phi(r,t)$ can be negligible with respect to the

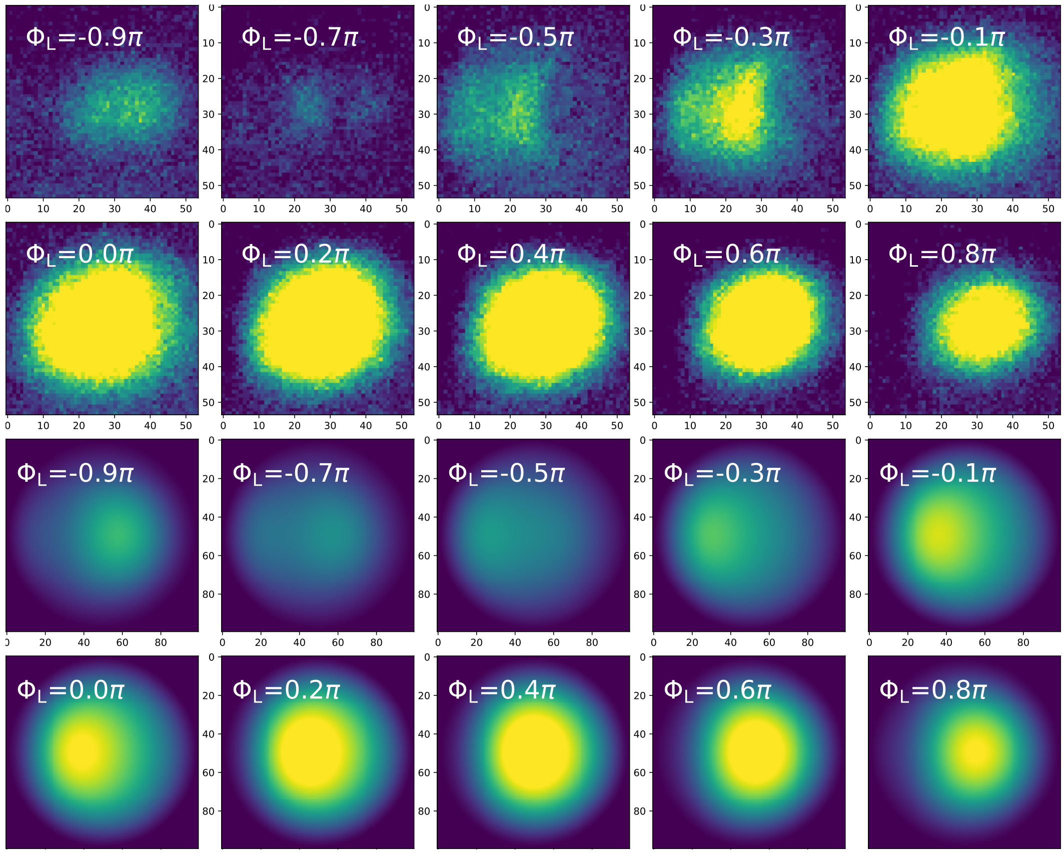

Figure 6.12: Scan the phase of the last pulse from $-\pi$ to π. We put the experiment parameters into simulation model B without any adjusting. The trapping frequency is [50, 102,102]Hz, $N_a = 220,000$, $T_R = 6ms$, $\theta = 0.3\pi$ and free fall time $T_F = 5ms$. The first two rows are the experimental results and the last two rows are the simulation results.

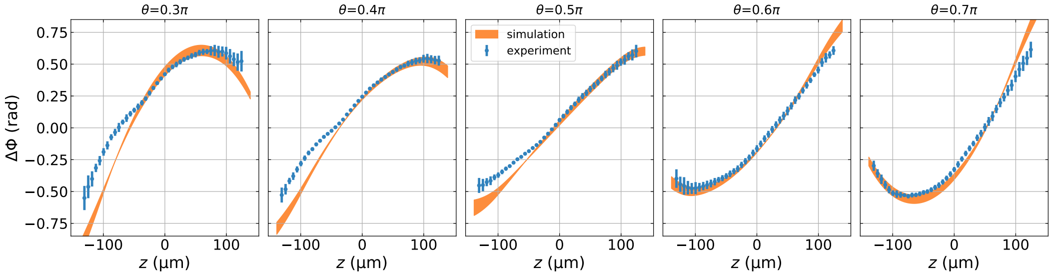

Figure 6.13: Variation of the phase shift at the output of the interferometer along the vertical z-axis, for different Raman pulse area θ. The points are the experimental data and each points are an averange of 7 points. The shaded area accounts for the fluctuation of the pulse area and trapping frequency.

chemical potential is correct.

Because in the usual atom interferometer, the imbalance factor $\alpha = 0$, so after then we try to understand more about this phase gradient when $\theta = 0.5\pi$.

Because this phase gradient comes from the separation of the two clouds and this means that this effect is only due to the mutual interaction. Here we will only care about the mutual interaction.

In model **B**, we know that the average potential felt by atoms with a given vertical position $\boldsymbol{z}$ is integral of Equation 6.27 over xy coordinate.

$$\bar{V}_k(z,t) = \frac{\iint g_{12} N \rho_l |\varphi_k(x,y,z)|^2 \,\mathrm{d}x\mathrm{d}y}{\iint |\varphi_k(x,y,z)|^2 \,\mathrm{d}x\mathrm{d}y} \tag{6.37}$$

The potential $\bar{V}_k(z,t)$ present the mutual potential felt by atom in path k (A or B). With the time integral $\bar{V}(z) = \int \bar{V}(z,t)\,\mathrm{d}t$ and do the phase difference between the two paths then we can get the local phase of atom at vertical position $\boldsymbol{z}$.

Now we consider an atom with initial position (x_0, y_0, z_0), where $r_{i,0} = \frac{r_i(t)}{\lambda_i(t)}$. Due to the symmetry of the cloud, we can first consider the situation $z_0 > 0$ then the same calculation can be used for $z_0 < 0$.

The trajectory and mutual interaction potential of the atom at position $\boldsymbol{z}$ in each path is shown in Figure 6.14:

We can see that the difference is only the blue part shown in Figure 6.14. It is easy to conclude that this phase difference is position z-dependant. The further the atom is away from the cloud center, the more significant phase difference it has at the end of the atom interferometer.

From Figure 6.14, it is clear that the phase difference between the two paths (the blue part in the picture) is highly related to when the atom can not feel (separation) and fell again (recombination) the mutual potential from another cloud. The different separation and combination times of the with position $\boldsymbol{z}_0$ they satisfy:

$$\begin{aligned}
t_{\mathrm{s}}^{A} &: \left(z_{\mathrm{TF}} - z_0\right)\lambda_z\left(t_{\mathrm{s}}^{A}\right) = 2v_{\mathrm{r}}\left(t_{\mathrm{s}}^{A} - t_{\mathrm{i}}\right) \\
t_{\mathrm{s}}^{B'} &: 2z_0\lambda_z\left(t_{\mathrm{s}}^{B'}\right) = 2v_{\mathrm{r}}\left(t_{\mathrm{s}}^{B'} - t_{\mathrm{i}}\right) \\
t_{\mathrm{s}}^{B} &: \left(z_{\mathrm{TF}} + z_0\right)\lambda_z\left(t_{\mathrm{s}}^{B}\right) = 2v_{\mathrm{r}}\left(t_{\mathrm{s}}^{B} - t_{\mathrm{i}}\right) \\
t_{\mathrm{c}}^{A} &: \left(z_{\mathrm{TF}} - z_0\right)\lambda_z\left(t_{\mathrm{c}}^{A}\right) = 2v_{\mathrm{r}}\left(t_{\mathrm{f}} - t_{\mathrm{c}}^{A}\right) \\
t_{\mathrm{c}}^{B} &: \left(z_{\mathrm{TF}} + z_0\right)\lambda_z\left(t_{\mathrm{c}}^{B}\right) = 2v_{\mathrm{r}}\left(t_{\mathrm{f}} - t_{\mathrm{c}}^{B}\right) \\
t_{\mathrm{c}}^{B'} &: 2z_0\lambda_z\left(t_{\mathrm{c}}^{B'}\right) = 2v_{\mathrm{r}}\left(t_{\mathrm{f}} - t_{\mathrm{c}}^{B'}\right)
\end{aligned} \tag{6.38}$$

And each separation time should be shorter than the mid-time of interferometer $t_1 = t_i + T_R$. Otherwise, it will be equal to t_1, which means the atoms at the center always see the mutual interaction from another cloud during the whole atom interferometer.

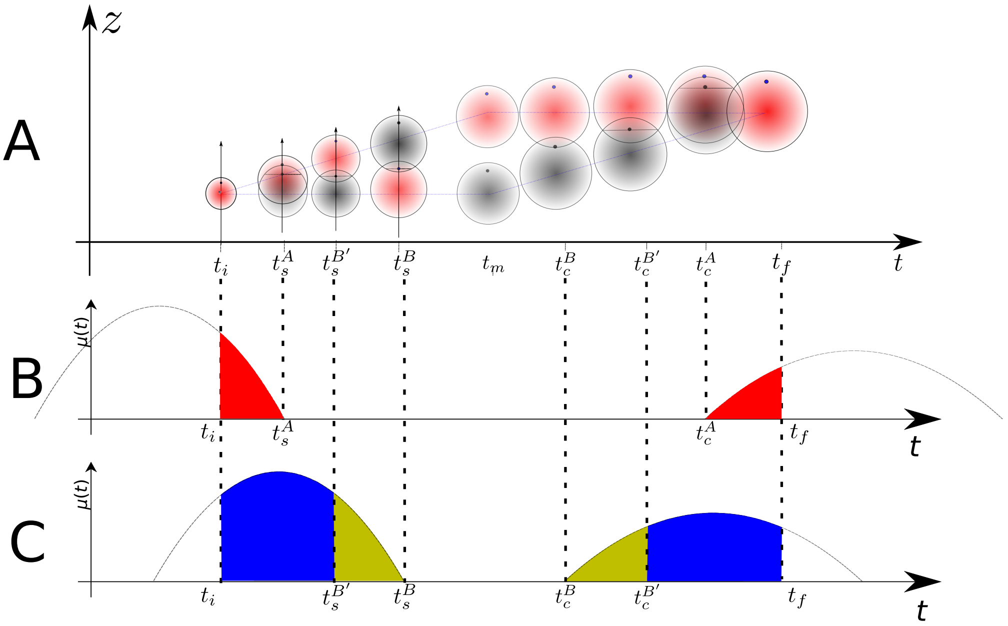

Figure 6.14: Figure A shows the trajectory of the two different cloud on z direction. The red part in figure B shows shows the atomic interaction potential integral for the atom at position z in the up cloud (Path A). The sum of blue and yellow part in figure C shows the atomic interaction integral for the atom at position z in the bottom cloud (Path B). The blue part shows the difference potential integral for up and bottom cloud.

The phase difference can be written as:

$$\Delta\phi = \left(\int_{t_i}^{t_\mathrm{s}^B} \left(\bar{V}_\mathrm{s}^A(z,t) - \bar{V}_\mathrm{s}^B(z,t)\right) \mathrm{d}t - \int_{t_i}^{t_\mathrm{s}^{B'}} \left(\bar{V}_\mathrm{s}^{B'}(z,t) - \bar{V}_\mathrm{s}^B(z,t)\right) \mathrm{d}t - \int_{t_\mathrm{s}^A}^{t_\mathrm{s}^B} \bar{V}_\mathrm{s}^A(z,t)\, \mathrm{d}t \right) + \\ \left(\int_{t_\mathrm{c}^A}^{t_f} \left(\bar{V}_\mathrm{s}^A(z,t) - \bar{V}_\mathrm{s}^B(z,t)\right) \mathrm{d}t - \int_{t_\mathrm{c}^{B'}}^{t_f} \left(\bar{V}_\mathrm{s}^{B'}(z,t) - \bar{V}_\mathrm{s}^B(z,t)\right) \mathrm{d}t - \int_{t_\mathrm{c}^B}^{t_\mathrm{c}^A} \bar{V}_\mathrm{c}^A(z,t)\, \mathrm{d}t \right) \tag{6.39}$$

Now we make our reasonable assumption to simplify this calculation: **The atom is close to the center of the cloud $z_0 \approx 0$.**

Then we found out that $t_\mathrm{s}^{B'} \approx t_i$, $t_\mathrm{c}^{B'} \approx t_f$ and $t_\mathrm{s}^A \approx t_\mathrm{s}^B$, $t_\mathrm{c}^A \approx t_\mathrm{c}^B$ which highly simplify the expression of phase difference:

$$\Delta\phi = \int_{t_i}^{t_\mathrm{s}^B} \left(\bar{V}_\mathrm{s}^A(z,t) - \bar{V}_\mathrm{s}^B(z,t)\right) \mathrm{d}t + \int_{t_\mathrm{c}^A}^{t_f} \left(\bar{V}_\mathrm{s}^A(z,t) - \bar{V}_\mathrm{s}^B(z,t)\right) \mathrm{d}t \tag{6.40}$$

This formula is easy to understand as the phase difference is the time integral of the average mutual potential difference on paths A and B. So if $z_0 \approx 0$, then $\Delta\phi \approx 0$ which is validated

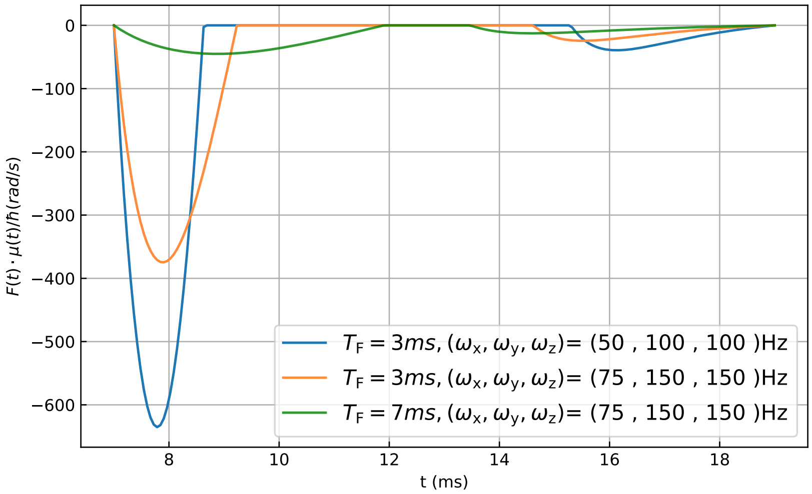

Figure 6.15: Evolution of the quantity $F(\Delta Z_R(t))\mu(t)$ during the interferometer sequence for different values of the trapping frequencies and release time T_F

in both experimental and simulation results. But what we care about is the phase gradient of the cloud, which is non-zero, shown in **Fig.**6.12. So it is enough to only consider the first order of z_0

Subsequent, we put average potential Equation 6.37 into Equation 6.40 then this expression can be written as :

$$\Delta\phi^{\mathrm{mut}} = \frac{2}{\hbar}\frac{a_{12}}{a_{11}} z_0 \mu \int_{t_i}^{t_f} G(t)F(\Delta Z_R)dt \tag{6.41}$$

$$\mathrm{with} F(x) = \begin{cases} x(x^4-1) & \text{if} \quad x<1 \\ 0 & \text{otherwise} \end{cases} \tag{6.42}$$

where the $\mu(t) = \mu/G(t)$ shows the dilution of the mean field with the cloud expansion, $\Delta Z_R = \Delta Z(t)/(Z_{TF}\lambda_z(t))$ expresses the separation and combination during the atom interfereometer where the cloud distance is shown in Equation 6.9.

The form of Equation 6.41 is interesting as it dissociates the effects of the chemical potential with the expansion $G(t)$ and of the separation of the two condensates $F(\Delta Z_R(t))$. The temporal evolution of these two terms depends on the expansion dynamics of the condensate, which is set by the trap frequencies. In Figure 6.15 we plot $F(\Delta Z_R(t))\mu(t)$ for two sets of trapping frequencies and two different release times T_F. We observe that the mutual interaction is significant at the beginning of the interferometer and that it declines as the condensates dilute. So we also expect a rapid decrease of the phase gradient with the T_F increasing.

At the end, for each free fall time from $3\,\mathrm{ms}$ to $20\,\mathrm{ms}$, we use a linear curve fit to extract the centre phase gradient $\nabla(\phi)$ with pulse area $\theta = 0.5\pi$. We have it shown in Figure 6.16.

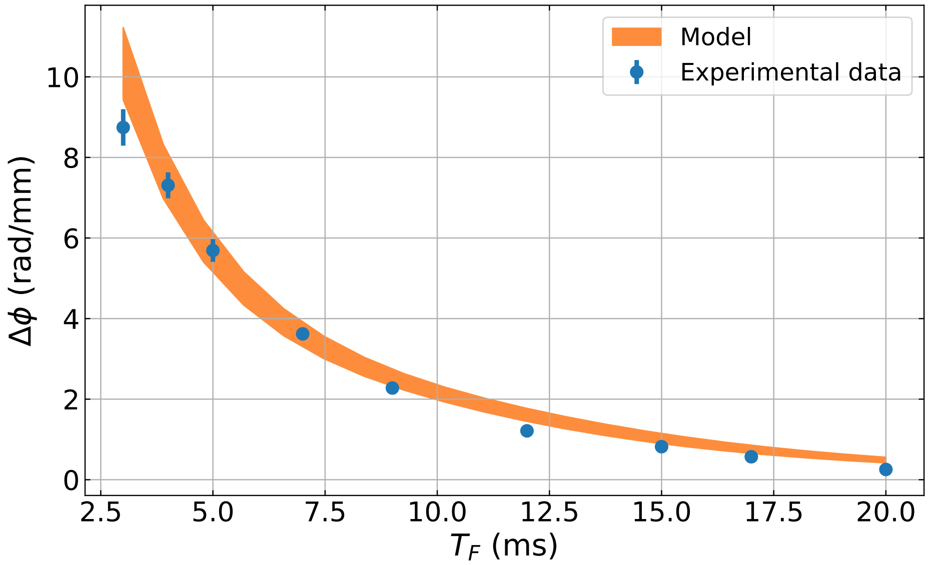

Figure 6.16: Phase gradient as function of release time $T_{\rm F}$. The orange shaded curve is the range of calculated phase gradient accounting for the uncertainty on the trapping frequencies.

6.4 Measurement of the scattering lenghts

In the previous sections we have discussed how the mean-field affects during the $\theta - \pi - \theta$ atom interferometer and the phase gradient due to the atomic interaction. In Figure 6.8 we see the phenomena due to the scattering length difference $\delta a = a_{11} - a_{22} \neq 0$. In this

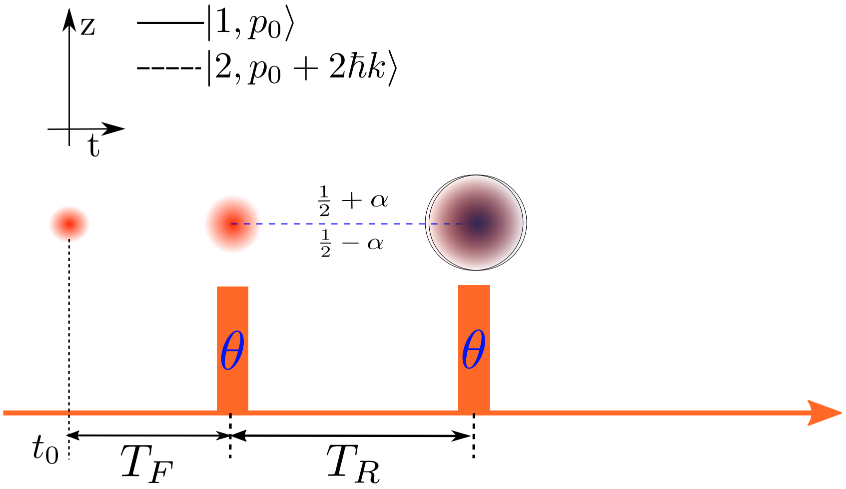

Figure 6.17: Schema presentation of $\theta - \theta$ Ramsey sequence. At the time t_0, we remove the dipole trap, and the BEC is released and begins to free fall. After a free time T_F we apply the pulse sequence $\theta \to \theta$ with time delay $T_{\rm R}$. We measured the total atoms in $|1\rangle$ and $|2\rangle$ by absorption imaging.

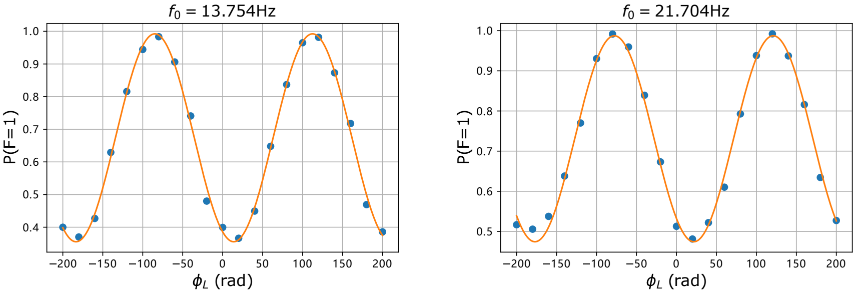

Figure 6.18: The points are the experimental data and the orange solid curves is the sinusoid fit curves. Both figures are manipulated with $\theta = 0.3\,\pi$ but with different free fall time(Left: 3 ms, Right: 21 ms). Their fringe centers are written on the top of each figure. The phase shift is calculated from $\Delta\phi = f_0 T_R$

section, we are going to use the $\theta - \theta$ atom interferometer (seen in Figure 6.17) to measure relatively the scattering length.

In this experiment, we use the microwave transition instead of two photon transition, so the clouds do not have separation during the atom interferometer. Unlike the previous experiment with two photon transition who scans the laser pahse, now we scan the frequency of the microwave to find the phse shift caused by the interaction. For each scanning frequency f, we can measure the probability of an atom in $|1\rangle$ by absorption imaging. Then we repeat the experiment with different scanning frequencies and extract the center fringe f_0 (seen in Figure 6.18) later, then deduce the phase shift $\Delta\phi = f_0 T_R$ due to atomic interaction.

Without separation between the two clouds, we can deduce that in model **A** we have $t_s = t_c = t_0 + T_R$ and $f_{\text{mut}}(t) = f_{\text{self}}(t) = 16/105$ in Equation 6.18. The phase difference at the output of the interferometer is:

$$\Delta\phi_{tot}(\alpha) = \frac{16}{105}\left[\frac{\omega_{22} - \omega_{11}}{2} + \alpha\left(\omega_{22} + \omega_{11} - 2\omega_{12}\right)\right]\int_{t_i}^{t_i+T_R} g(t) \qquad (6.43)$$

From Equation 6.43, the phase difference at the interferometer's output varies with the imbalance factor α, which can be done by varying the θ pulse. The offset and slope of this curve will give us information about the scattering length a_{11}, a_{12} and a_{22}. But one issue is the second-order Zeeman effect in our experiment will also introduce a phase shift $\Delta\phi_{zeeman}$.

In order to know the second-order Zeeman effect, we let the atom cloud-free fall for a long time so that the mean-field will be negligible. From the **Fig.**6.8 we know that the mean-field has already vanished when $T_F = 21ms$, so we experiment with two different free-fall times.

- $T_F = 0.1ms$ the dephasse is caused by the 2nd order zeeman effect and the mean-field effect $\Delta\phi_1(\alpha) = \Delta\phi_{MF}(\alpha) + \Delta\phi_{zeeman}$

- $T_F = 21ms$ is only caused by the 2nd order zeeman effect $\Delta\phi_2 = \Delta\phi_{zeeman}$.

These two results are shown in Figure 6.19:

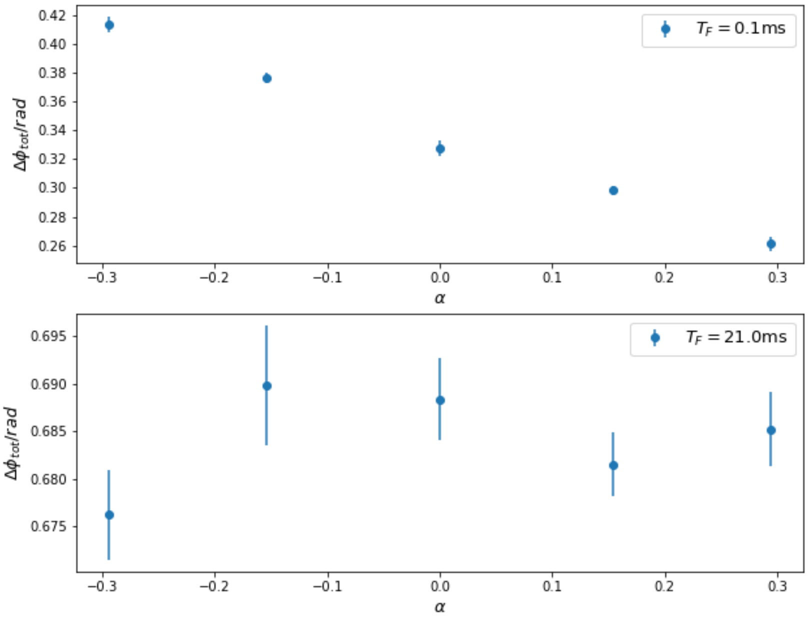

Figure 6.19: The phase shift due to the atomic interaction by changing different imbalance factor α and two different free fall times. ***a***: The free fall time $T_F = 0.1\,\text{ms}$, ***b***: The free fall time $T_F = 21\,\text{ms}$

To get $\Delta\phi_{MF}(\alpha)$, we just do $\Delta\phi_1(\alpha) - \Delta\bar{\phi}_2$ and then compare the slope and offset of this curve we can deduce the ratio $(a_{11} - a_{22})/(a_{11} + a_{22} - 2a_{12})$.

At the end we determine the ratio $\frac{a_{11}-a_{22}}{a_{11}+a_{22}-2a_{12}} = 1.351 \pm 0.063$, and in my numerical calculation I used the scattering length $a_{11} = 100.9a_0$, $a_{12} = 96.9a_0$, $a_{22} = 94.9a_0$ [5], which gives the theoretical value of this ratio is 1.5. And the recent measurement of J.Dalibard's is 1.16(9)[79]. Our result agrees with these two results.

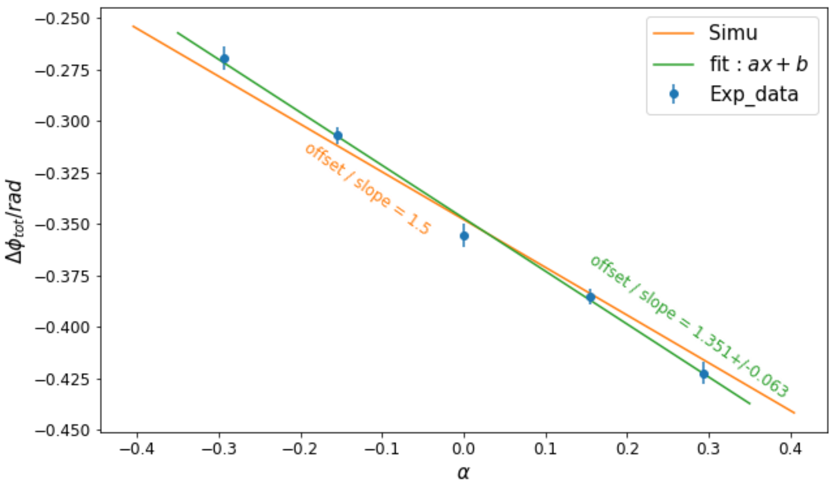

Figure 6.20: $\Delta\phi_{\mathrm{MF}}$ varies with the imbalance factor α. The points are the experimental data, the green curve is a linear curve fit function based on the experimental results. The orange curve is the simulation result of model $\boldsymbol{A}$ with setting scattering length $a_{11} = 100.9a_0$, $a_{12} = 96.9a_0$, $a_{22} = 94.9a_0$

6.5 Conclusion

In this chapter, we have investigated in detail both theoretically and experimentally the phase shift due to atomic interactions in an atom interferometer.

First, by comparing the two different models, we prove that Feynman integral approach can give the same result as the approach based on the evolution of the BEC phase given by Gross-Pitaevskii equation and Castin & Dum's model. Our theoretical models can be used to derive general formulas for phase shifts related to self-interaction and mutual interaction. Our models are general and accounts for the effect of a population imbalance between the two arms of the interferometer as well as of the difference in scattering lengths of the hyperfine states. It allows to evaluate precisely the interaction phase shifts knowing the time evolution of the spatial density of the Bose-Einstein condensate. Relying on the Castin-Dum model, which describes the temporal evolution of the BEC spatial density in the Thomas-Fermi regime, we calculated the phase shift induced by the atomic interactions and in particular, the phase gradient (model $\boldsymbol{B}$) resulting from the mutual interaction. We measured experimentally the phase gradient and the total phase shift (accounting for mutual and self interactions) by varying the experimental parameters (BEC release time, trapping frequencies and Raman coupling). The theoretical curves reproduce the experimental data well without adjusting the parameters.

In particular, the work presented in this paper has enabled us to evaluate the phase gradient due to the mutual interactions between the two interfering condensates. It also provides theoretical tools, validated by the experiment, to evaluate the phase shifts induced by atomic interactions. The treatment of the interaction effect by the Feynman path integral approach can be generalized to other atom interferometer configurations and offers a the simple way to accurately evaluate the related systematic effect that could affect high-precision measurements with atom interferometry.

Conclusion and outlooks

The first part of this manuscript presents our last measurement of the ratio h/m by atom interferometry. This measurement relies on the combination of an atom interferometer with Bloch oscillations in an accelerated optical lattice. After presenting these concepts we described our experimental setup.

This measurement allowed to determine the fine-structure constant α with a relative accuracy of 81 ppt. Notably, this unprecedented accuracy also improves the theoretical value of the electron magnetic moment anomaly $a_{\mathrm{e}}(\mathrm{theo})$. For the first time, the theoretical value of $a_{\mathrm{e}}(\mathrm{theo})$ has better accuracy than the experimental value $a_{\mathrm{e}}(\exp)$. However, our new value of the fine-structure constant ddiffers by 5.4σ from from the value of α obtained from the caesium recoil measurement. This discrepancy needs to be clarified and this motivates the further investigations by the team using a Bose-Einstein condensate and also the rubidium isotope 85

We demonstrated that our experimental setup is robust with unprecedented statistical uncertainty. It is limited by different systematic effects.

Three new systematic effects were discovered, and two of them: the **gouy phase** and **residual Raman light shift**, are supposed to be mitigated by using a colder and smaller atom source. This motivates us to experiment with Bose-Einstein Condensates.

During my PhD, I improved both the efficiency and the stability of our optical evaporative cooling to generate BEC with $220\,000$ atoms within $3.2\,\mathrm{s}$. However, in such a dense cloud, the atomic interactions are significant and could induce a detrimental phase shift that can undermine the benefits of using Bose-Einstein condensates for precision measurements with atom interferometry.

To understand how the atomic interaction affects the atom interferometer, we proposed two different models that can reproduce our experimental data well without adjusting any parameters. Moreover, we can use it to study the phase gradient due to the mutual interaction.

Our model predicts that the impact of the atomic interactions is negligible for our h/m measurement if we apply the atom interferometer long after the BEC is released from the trap. The BEC production is stable enough to run the h/m measurement over one day. We checked that the h/m measurement's uncertainty for one sequence using the BEC is similar to the one obtained using a molasses (apart from the difference in the total experiment cycle time due to the longer preparation sequence to produce a BEC). However, the statistical

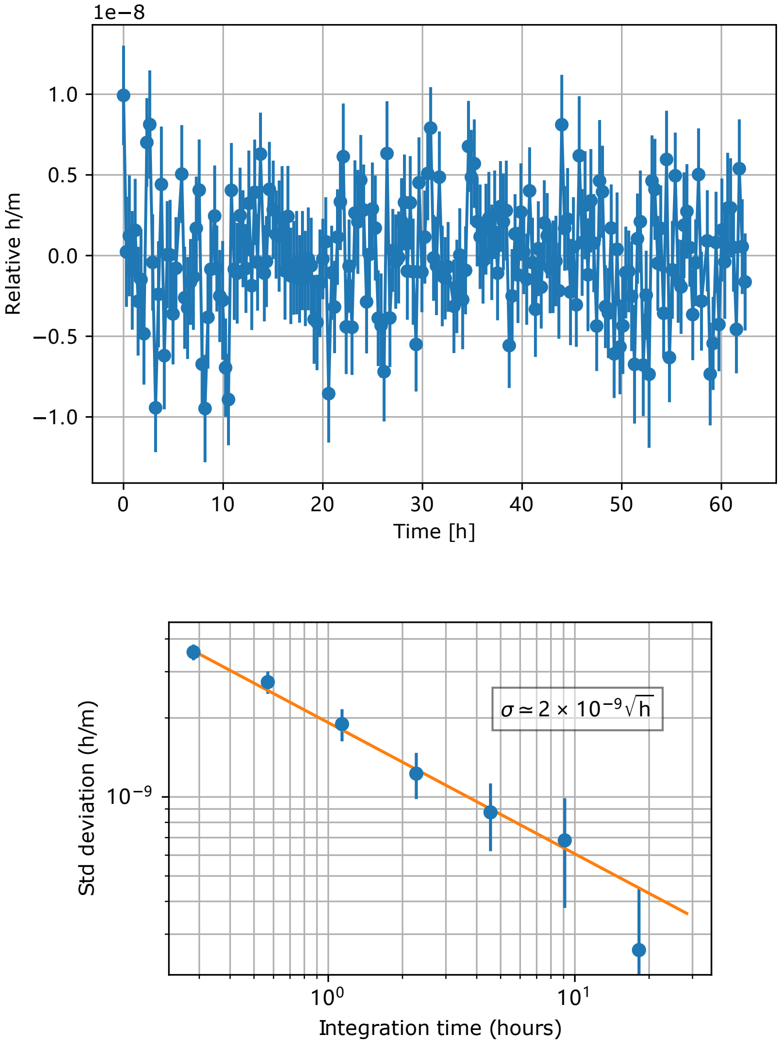

Figure 6.21: Top: Set of h/m determinations taken over 60 hours. Each point correspond to ~ 13 minutes of integration. Bottom: Comparison between the data Allan deviation and the expected behavior in the case of a white noise induced data distribution.

uncertainty is slightly lower than the one of our last measurement with molasses. But as this is just a preliminary result, some improvements could be made in the future

In the meantime we also developed a more powerful laser system that will help us to reduce some of the main systematic effects by using larger beams. As a perspective after completing the h/m measurement with the BEC, we plan to redo the measurement with the other isotope ^{85}Rb.

Annexe

.1 Model B

- For a given atom number N_a in $|F = 1\rangle$ and trapping frequencies $\omega_{x,y,z}$, using the Thomas-Fermi regime $|\varphi|^2 = \sqrt{\frac{\mu-\frac{1}{2}\sum m\omega_j(t)^2 r_j^2}{g_{11}N}}$, we get the initial 3D probability distribution (matrix 100× 100 × 100). we have the probability distribution of the atom cloud
.

- After then based on the Castin-Dum formula

$$\ddot{\lambda_j} = \frac{\omega_j^2(0)}{\lambda_j \lambda_x \lambda_y \lambda_z} - \lambda_j \omega_j^2(t)$$

we can calculate the cloud expansion when we remove the trapping potential which means $\omega_j^2(t) = 0$

- At time t_0 we put our first Raman pulse to transfer the atoms into a superposition state $C_1|F = 1\rangle + C_2|F = 2\rangle$, and the atoms in $|F = 2\rangle$ will get a additional split velocity, which is double recoil velocity $2\vec{v_r}$. So after the first pulse the cloud is separated into two path, the up path and bottom path, and they recombine at the last raman pulse.

- For an atom with its initial position r_{j0}, we calculate the phase due to the atomic interaction by doing the Lagrange integral along each arm of the atom interferometer:

$$\phi_{atom} = \frac{1}{\hbar} \int \frac{mv^2}{2} - V dt$$

For the kinetic part the expansion velocity is $\dot{\lambda} r_{j0}$. During the atom interferometer only when the atoms are in the state $|F = 2\rangle$ the velocity is $\dot{\lambda} r_{j0} + 2v_r$ otherwise the velocity is $\dot{\lambda} r_{j0}$. And the **V** can be splitted into two part: one is self interaction (between the same internal state) and another is mutual interaction (between the two different internal state). Then we calculate ϕ_{atom}^{up} and ϕ_{atom}^{bottom}

- During the atom interferometer, we have three raman lasers at time $t_1 = t_0$, $t_2 = t_0 + T_R$, $t_3 = t_0 + 2T_R$. The laser phase is translated to the atoms when the atom changes its internal state. So the final dephase due to the laser is

$$\Delta\phi_{laser}^{up} = k_R(t1) \cdot r_j(t1) - k_R(t2) \cdot r_j(t2) + k_R(t3) \cdot r_j(t3) + \phi_{scan}$$

$$\Delta\phi_{laser}^{bottom} = k_R(t2) \cdot r_j(t2)$$

• At the end the two cloud is overlapped, and based on what we did before we know the wave function ψ. The probability to detect $|F = 1\rangle$ is

$$|\langle\psi|F = 1\rangle|^2 = \frac{\mu - \frac{1}{2}\sum m\omega_j(t)^2 r_j^2}{g_{11}N}|((\frac{1}{2} - \alpha)e^{j(\phi_{atom}^{up} + \phi_{laser}^{up})} + (\frac{1}{2} - \alpha)e^{j(\phi_{atom}^{bottom} + \phi_{laser}^{bottom})})|^2$$

And in the simulation we scan the phase of the last laser pulse from $-\pi$ to π.

• For each scan phase at the end we have a 3D probability distribution, we integral along XY dimensions and for each position Z we can calculate phase shift due to the meanfield. By this way we get the phase gradient of the atom cloud.

Bibliography

[1] B. Abi et al. “Measurement of the Positive Muon Anomalous Magnetic Moment to 0.46 ppm”. In: *Phys. Rev. Lett.* 126 (14 2021), p. 141801. DOI: 10.1103/PhysRevLett.126.141801. URL: https://link.aps.org/doi/10.1103/PhysRevLett.126.141801.

[2] ACME Collaboration. “Improved Limit on the Electric Dipole Moment of the Electron”. In: *Nature* 562.7727 (Oct. 2018), pp. 355–360. ISSN: 0028-0836, 1476-4687. DOI: 10.1038/s41586-018-0599-8. URL: http://www.nature.com/articles/s41586-018-0599-8 (visited on 07/08/2019).

[3] Phil Adamson et al. *PROPOSAL: P-1101. Matter-wave Atomic Gradiometer Interferometric Sensor (MAGIS-100).* Dec. 2018. DOI: 10.2172/1605586. URL: https://www.osti.gov/biblio/1605586.

[4] D. N. Aguilera et al. “STE-QUEST - Test of the universality of free fall using cold atom interferometry”. In: *Classical and Quantum Gravity* 31.11 (June 2014). ISSN: 0264-9381. DOI: 10.1088/0264-9381/31/11/115010.

[5] P A Altin et al. “Optically trapped atom interferometry using the clock transition of large RB-87 Bose–Einstein condensates”. In: *New Journal of Physics* 13.6 (2011), p. 065020. DOI: 10.1088/1367-2630/13/6/065020.

[6] Manuel Andia. “Oscillations de Bloch d’atomes ultra-froids: application aux mesures de haute précision.” In: *PhD Thesis* (2015), p. 213.

[7] T. Aoyama et al. “The anomalous magnetic moment of the muon in the Standard Model”. In: *Phys. Rept.* 887 (2020), pp. 1–166. DOI: 10.1016/j.physrep.2020.07.006. arXiv: 2006.04822 [hep-ph].

[8] Tatsumi Aoyama, Toichiro Kinoshita, and Makiko Nio. “Theory of the Anomalous Magnetic Moment of the Electron”. In: *Atoms* 7.1 (2019). ISSN: 2218-2004. DOI: 10.3390/atoms7010028. URL: https://www.mdpi.com/2218-2004/7/1/28.

[9] Asimina Arvanitaki, Junwu Huang, and Ken Van Tilburg. “Searching for dilaton dark matter with atomic clocks”. In: *Phys. Rev. D* 91 (1 2015), p. 015015. DOI: 10.1103/PhysRevD.91.015015. URL: https://link.aps.org/doi/10.1103/PhysRevD.91.015015.

[10] Asimina Arvanitaki et al. “Search for light scalar dark matter with atomic gravitational wave detectors”. In: *Phys. Rev. D* 97 (7 2018), p. 075020. DOI: 10.1103/PhysRevD.97.075020. URL: https://link.aps.org/doi/10.1103/PhysRevD.97.075020.

[11] Peter Asenbaum et al. “Atom-Interferometric Test of the Equivalence Principle at the 10^{-12} Level”. In: *Phys. Rev. Lett.* 125 (19 2020), p. 191101. DOI: 10.1103/PhysRevLett.125.191101. URL: https://link.aps.org/doi/10.1103/PhysRevLett.125.191101.

[12] G. Audi et al. “The 2012 Atomic Mass Evaluation and the Mass Tables”. In: *Nuclear Data Sheets* 120 (2014), pp. 1–5. ISSN: 0090-3752. DOI: https://doi.org/10.1016/j.nds.2014.06.126. URL: https://www.sciencedirect.com/science/article/pii/S0090375214004438.

[13] Satyanarayana Bade et al. “Observation of Extra Photon Recoil in a Distorted Optical Field”. In: *Physical Review Letters* 121.7 (Aug. 16, 2018). ISSN: 0031-9007, 1079-7114. DOI: 10.1103/PhysRevLett.121.073603. URL: https://link.aps.org/doi/10.1103/PhysRevLett.121.073603 (visited on 07/08/2019).

[14] X. Baillard et al. “Interference-Filter-Stabilized External-Cavity Diode Lasers”. In: *Optics Communications* 266.2 (Oct. 2006), pp. 609–613. ISSN: 00304018. DOI: 10.1016/j.optcom.2006.05.011. URL: https://linkinghub.elsevier.com/retrieve/pii/S0030401806004561 (visited on 07/11/2019).

[15] Dennis Becker et al. “Space-borne Bose–Einstein condensation for precision interferometry”. In: *Nature* 562.7727 (2018), pp. 391–395. DOI: 10.1038/s41586-018-0605-1. URL: https://doi.org/10.1038/s41586-018-0605-1.

[16] I. Bloch, T. W. Hänsch, and T. Esslinger. “Measurement of the spatial coherence of a trapped Bose gas at the phase transition”. In: *Nature* 403.6766 (2000), pp. 166–170. DOI: 10.1038/35003132.

[17] Rym Bouchendira. “Mesure de l’effet de Recul de l’atome de Rubidium Par Interférométrie Atomique : Nouvelle Détermination de La Constante de Structure Fine Pour Tester l’électrodynamique Quantique”. In: *PhD Thesis* (2012).

[18] Rym Bouchendira et al. “New Determination of the Fine Structure Constant and Test of the Quantum Electrodynamics”. In: *Physical Review Letters* 106.8 (Feb. 24, 2011). ISSN: 0031-9007. DOI: 10.1103/physrevlett.106.080801.

[19] A. Burchianti et al. “Effect of interactions in the interference pattern of Bose-Einstein condensates”. In: *Physical Review A* 102.4 (2020), p. 043314. DOI: 10.1103/physreva.102.043314.

[20] Malo Cadoret. “Application Des Oscillations de Bloch d’atomes Ultra-Froids et de l’interférométrie Atomique à La Mesure de h/m et à La Détermination de La Constante de Structure Fine”. In: *PhD Thesis* (2008).

[21] B. Canuel et al. “Exploring gravity with the MIGA large scale atom interferometer”. In: *Scientific Reports* 8.1 (2018), p. 14064. doi: 10.1038/s41598-018-32165-z. url: https://doi.org/10.1038/s41598-018-32165-z.

[22] Y. Castin and R. Dum. “Bose-Einstein Condensates in Time Dependent Traps”. In: *Physical Review Letters* 77.27 (1996), pp. 5315–5319. doi: 10.1103/physrevlett.77.5315.

[23] Sheng-wey Chiow et al. “102 hbar k Large Area Atom Interferometers”. In: *Physical Review Letters* 107.13 (Sept. 19, 2011). issn: 0031-9007, 1079-7114. doi: 10.1103/PhysRevLett.107.130403. url: https://link.aps.org/doi/10.1103/PhysRevLett.107.130403 (visited on 07/24/2019).

[24] Pierre Cladé. “Oscillations de Bloch d’atomes ultrafroids et mesure de la constante de structure fine”. In: *PhD Thesis* (2005), p. 233.

[25] Pierre Cladé et al. “Large Momentum Beam Splitter Using Bloch Oscillations”. In: *Physical Review Letters* 102.24 (June 18, 2009). issn: 0031-9007. doi: 10.1103/physrevlett.102.240402.

[26] Claude Cohen-Tannoudji and David Guéry-Odelin. *Advances in Atomic Physics*. WORLD SCIENTIFIC, 2011. doi: 10.1142/6631.

[27] Clément Courvoisier. “Condensat de Bose-Einstein par refroidissement évaporatif dans un piège dipolaire pour la métrologie par interférométrie atomique”. PhD thesis. 2016, p. 181.

[28] A. Couvert et al. “A Quasi-Monomode Guided Atom Laser from an All-Optical Bose-Einstein Condensate”. In: *EPL (Europhysics Letters)* 83.5 (Sept. 2008), p. 50001. issn: 0295-5075, 1286-4854. doi: 10.1209/0295-5075/83/50001. url: http://stacks.iop.org/0295-5075/83/i=5/a=50001?key=crossref.ba44f177a7c4911c4a0a408a93c2ef2e (visited on 07/02/2019).

[29] Andrzej Czarnecki, Bernd Krause, and William J. Marciano. “Electroweak Corrections to the Muon Anomalous Magnetic Moment”. In: *Phys. Rev. Lett.* 76 (18 1996), pp. 3267–3270. doi: 10.1103/PhysRevLett.76.3267. url: https://link.aps.org/doi/10.1103/PhysRevLett.76.3267.

[30] Andrzej Czarnecki, William J. Marciano, and Arkady Vainshtein. “Refinements in electroweak contributions to the muon anomalous magnetic moment”. In: *Phys. Rev. D* 67 (7 2003), p. 073006. doi: 10.1103/PhysRevD.67.073006. url: https://link.aps.org/doi/10.1103/PhysRevD.67.073006.

[31] J. Dalibard and C. Cohen-Tannoudji. “Laser Cooling below the Doppler Limit by Polarization Gradients: Simple Theoretical Models”. In: *Journal of the Optical Society of America B* 6.11 (Nov. 1, 1989), p. 2023. issn: 0740-3224, 1520-8540. doi: 10.1364/JOSAB.6.002023. url: https://www.osapublishing.org/abstract.cfm?URI=josab-6-11-2023 (visited on 07/08/2019).

[32] J. Dalibard, S. Reynaud, and C. Cohen-Tannoudji. “Proposals of Stable Optical Traps for Neutral Atoms”. In: *Optics Communications* 47.6 (Oct. 1983), pp. 395–399. ISSN: 00304018. DOI: 10.1016/0030-4018(83)90314-0. URL: https://linkinghub.elsevier.com/retrieve/pii/0030401883903140 (visited on 07/02/2019).

[33] X. Fan and G. Gabrielse. “Driven one-particle quantum cyclotron”. In: *Phys. Rev. A* 103 (2 2021), p. 022824. DOI: 10.1103/PhysRevA.103.022824. URL: https://link.aps.org/doi/10.1103/PhysRevA.103.022824.

[34] Kai Frye et al. “The Bose-Einstein Condensate and Cold Atom Laboratory”. In: *EPJ Quantum Technology* 8.1 (2021), p. 1. DOI: 10.1140/epjqt/s40507-020-00090-8. URL: https://doi.org/10.1140/epjqt/s40507-020-00090-8.

[35] Kazuo Fujikawa, Benjamin W. Lee, and A. I. Sanda. “Generalized Renormalizable Gauge Formulation of Spontaneously Broken Gauge Theories”. In: *Phys. Rev. D* 6 (10 1972), pp. 2923–2943. DOI: 10.1103/PhysRevD.6.2923. URL: https://link.aps.org/doi/10.1103/PhysRevD.6.2923.

[36] Martina Gebbe et al. “Twin-lattice atom interferometry”. In: *Nature Communications* 12.1 (2021). DOI: 10.1038/s41467-021-22823-8.

[37] G. F. Giudice, P. Paradisi, and M. Passera. “Testing new physics with the electron g -2”. In: *Journal of High Energy Physics* 2012.11 (2012), p. 113. DOI: 10.1007/JHEP11(2012)113. URL: https://doi.org/10.1007/JHEP11(2012)113.

[38] Peter W. Graham et al. “Dark matter direct detection with accelerometers”. In: *Phys. Rev. D* 93 (7 2016), p. 075029. DOI: 10.1103/PhysRevD.93.075029. URL: https://link.aps.org/doi/10.1103/PhysRevD.93.075029.

[39] Peter W. Graham et al. “Spin precession experiments for light axionic dark matter”. In: *Phys. Rev. D* 97 (5 2018), p. 055006. DOI: 10.1103/PhysRevD.97.055006. URL: https://link.aps.org/doi/10.1103/PhysRevD.97.055006.

[40] Rudolf Grimm, Matthias Weidemüller, and Yurii B. Ovchinnikov. “Optical Dipole Traps for Neutral Atoms”. In: ed. by Benjamin Bederson and Herbert Walther. Vol. 42. Advances In Atomic, Molecular, and Optical Physics. Academic Press, 2000, pp. 95–170. DOI: https://doi.org/10.1016/S1049-250X(08)60186-X. URL: http://www.sciencedirect.com/science/article/pii/S1049250X0860186X.

[41] Q. Guan et al. “Rabi oscillations and Ramsey-type pulses in ultracold bosons: Role of interactions”. In: *Phys. Rev. A* 101 (6 2020), p. 063620. DOI: 10.1103/PhysRevA.101.063620. URL: https://link.aps.org/doi/10.1103/PhysRevA.101.063620.

[42] E. W. Hagley et al. “Measurement of the Coherence of a Bose-Einstein Condensate”. In: *Physical Review Letters* 83.16 (1999), pp. 3112–3115. doi: `10.1103/physrevlett.83.3112`.

[43] D. Hanneke, S. Fogwell, and G. Gabrielse. “New Measurement of the Electron Magnetic Moment and the Fine Structure Constant”. In: *Phys. Rev. Lett.* 100 (12 2008), p. 120801. doi: `10.1103/PhysRevLett.100.120801`. url: `https://link.aps.org/doi/10.1103/PhysRevLett.100.120801`.

[44] Philipp Haslinger et al. “Attractive force on atoms due to blackbody radiation”. In: *Nature Physics* 14.3 (2018), pp. 257–260. doi: `10.1038/s41567-017-0004-9`. url: `https://doi.org/10.1038/s41567-017-0004-9`.

[45] David W. Hertzog and William M. Morse. “THE BROOKHAVEN MUON ANOMALOUS MAGNETIC MOMENT EXPERIMENT”. In: *Annual Review of Nuclear and Particle Science* 54.1 (2004), pp. 141–174. doi: `10.1146/annurev.nucl.53.041002.110618`. eprint: `https://doi.org/10.1146/annurev.nucl.53.041002.110618`. url: `https://doi.org/10.1146/annurev.nucl.53.041002.110618`.

[46] Raphaël Jannin. “Interférométrie atomique avec un condensat de Bose-Einstein : effet des interactions internes”. PhD thesis. 2015, p. 183.

[47] Raphaël Jannin, Pierre Cladé, and Saïda Guellati-Khélifa. “Phase Shift Due to Atom-Atom Interactions in a Light-Pulse Atom Interferometer”. In: *Physical Review A* 92.1 (July 13, 2015). issn: 1050-2947. doi: `10.1103/physreva.92.013616`.

[48] M. Kasevich and S. Chu. “Measurement of the gravitational acceleration of an atom with a light-pulse atom interferometer”. In: *Applied Physics B Photophysics and Laser Chemistry* 54.5 (1992), pp. 321–332. doi: `10.1007/bf00325375`.

[49] Alexander Kurz et al. “Hadronic contribution to the muon anomalous magnetic moment to next-to-next-to-leading order”. In: *Physics Letters B* 734 (2014), pp. 144–147. issn: 0370-2693. doi: `https://doi.org/10.1016/j.physletb.2014.05.043`. url: `https://www.sciencedirect.com/science/article/pii/S0370269314003529`.

[50] P. Kusch and H. M. Foley. “Precision Measurement of the Ratio of the Atomic ‘g Values’ in the $^{2}P_{32}$ and $^{2}P_{12}$ States of Gallium”. In: *Physical Review* 72.12 (Dec. 1947), pp. 1256–1257. doi: `10.1103/PhysRev.72.1256.2`.

[51] Willis E. Lamb and Robert C. Retherford. “Fine Structure of the Hydrogen Atom by a Microwave Method”. In: *Phys. Rev.* 72 (3 1947), pp. 241–243. doi: `10.1103/PhysRev.72.241`. url: `https://link.aps.org/doi/10.1103/PhysRev.72.241`.

[52] K B MacAdam, A Steinbach, and C Wieman. “A Narrow-band Tunable Diode Laser System with Grating Feedback, and a Saturated Absorption Spectrometer for Cs and Rb”. In: *American Journal of Physics* 60.1098 (1992), p. 15.

[53] Benjamin K. Malia et al. "Free Space Ramsey Spectroscopy in Rubidium with Noise below the Quantum Projection Limit". In: *Physical Review Letters* 125.4 (2020), p. 043202. DOI: `10.1103/physrevlett.125.043202`.

[54] Léo Morel. "High sensitivity matter-wave interferometry : towards a determination of the fine structure constant below 10-10". Thèse de doctorat dirigée par Guellati-Khelifa, Saïda et Cladé, Pierre Physique Sorbonne université 2019. PhD thesis. 2019. URL: `http://www.theses.fr/2019SORUS264`.

[55] Léo Morel et al. "Determination of the fine-structure constant with an accuracy of 81 parts per trillion". In: *Nature* 588.7836 (2020), pp. 61–65. DOI: `10.1038/s41586-020-2964-7`.

[56] Holger Müller et al. "Atom Interferometers with Scalable Enclosed Area". In: *Physical Review Letters* 102.24 (2009), p. 240403. DOI: `10.1103/physrevlett.102.240403`.

[57] A W Naji et al. "Review of Erbium-Doped Fiber Amplifier". In: *Int. J. Phys. Sci.* 6.20 (2011), pp. 4674–4689.

[58] Daisuke Nomura and Thomas Teubner. "Hadronic contributions to the anomalous magnetic moment of the electron and the hyperfine splitting of muonium". In: *Nuclear Physics* 867 (2013), pp. 236–243.

[59] Richard H. Parker et al. "Measurement of the fine-structure constant as a test of the Standard Model". In: *Science* 360 (2018), p. 191. DOI: `10.1126/science.aap7706`. arXiv: `1812.04130 [physics.atom-ph]`.

[60] Michael A. Perlin, Chunlei Qu, and Ana Maria Rey. "Spin Squeezing with Short-Range Spin-Exchange Interactions". In: *Physical Review Letters* 125.22 (2020), p. 223401. DOI: `10.1103/physrevlett.125.223401`.

[61] Pippa Storey and Claude Cohen-Tannoudji. "The Feynman path integral approach to atomic interferometry. A tutorial". In: *J. Phys. II France* 4.11 (1994), pp. 1999–2027. DOI: `10.1051/jp2:1994103`. URL: `https://doi.org/10.1051/jp2:1994103`.

[62] E. L. Raab et al. "Trapping of Neutral Sodium Atoms with Radiation Pressure". In: *Physical Review Letters* 59.23 (Dec. 7, 1987), pp. 2631–2634. ISSN: 0031-9007. DOI: `10.1103/PhysRevLett.59.2631`. URL: `https://link.aps.org/doi/10.1103/PhysRevLett.59.2631` (visited on 07/02/2019).

[63] Erling Riis et al. "Atom Funnel for the Production of a Slow, High-Density Atomic Beam". In: *Physical Review Letters* 64.14 (Apr. 2, 1990), pp. 1658–1661. ISSN: 0031-9007. DOI: `10.1103/PhysRevLett.64.1658`. URL: `https://link.aps.org/doi/10.1103/PhysRevLett.64.1658` (visited on 07/02/2019).

[64] G. Rosi et al. "Precision measurement of the Newtonian gravitational constant using cold atoms". In: *Nature* 510.7506 (2014), pp. 518–521. DOI: `10.1038/nature13433`. URL: `https://doi.org/10.1038/nature13433`.

[65] Julian Schwinger. “On Quantum-Electrodynamics and the Magnetic Moment of the Electron”. In: *Phys. Rev.* 73 (4 1948), pp. 416–417. doi: 10.1103/PhysRev.73.416. url: https://link.aps.org/doi/10.1103/PhysRev.73.416.

[66] Simsarian et al. “Imaging the phase of an evolving bose-einstein condensate wave function”. In: *Physical review letters* 85 (10 Sept. 2000), pp. 2040–2043. issn: 1079-7114. doi: 10.1103/PhysRevLett.85.2040. ppublish.

[67] J. E. Simsarian et al. “Imaging the Phase of an Evolving Bose-Einstein Condensate Wave Function”. In: *Phys. Rev. Lett.* 85 (10 2000), pp. 2040–2043. doi: 10.1103/PhysRevLett.85.2040. url: https://link.aps.org/doi/10.1103/PhysRevLett.85.2040.

[68] A. Sommerfeld. “Zur Quantentheorie der Spektrallinien”. In: *Annalen der Physik* 356.17 (1916), pp. 1–94. doi: https://doi.org/10.1002/andp.19163561702. eprint: https://onlinelibrary.wiley.com/doi/pdf/10.1002/andp.19163561702. url: https://onlinelibrary.wiley.com/doi/abs/10.1002/andp.19163561702.

[69] Daniel Steck A. “Rubidium 87 D Line Data”. In: (2001). url: https://steck.us/alkalidata/rubidium87numbers.1.6.pdf.

[70] S. Sturm et al. “High-Precision Measurement of the Atomic Mass of the Electron”. In: *Nature* 506.7489 (Feb. 2014), pp. 467–470. issn: 0028-0836, 1476-4687. doi: 10.1038/nature13026. url: http://www.nature.com/articles/nature13026 (visited on 07/08/2019).

[71] Stuart S. Szigeti et al. “High-Precision Quantum-Enhanced Gravimetry with a Bose-Einstein Condensate”. In: *Physical Review Letters* 125.10 (2020), p. 100402. doi: 10.1103/physrevlett.125.100402.

[72] F. Terranova and G. M. Tino. “Testing the a_μ anomaly in the electron sector through a precise measurement of h/M”. In: *Phys. Rev. A* 89 (5 2014), p. 052118. doi: 10.1103/PhysRevA.89.052118. url: https://link.aps.org/doi/10.1103/PhysRevA.89.052118.

[73] Eite Tiesinga et al. “CODATA recommended values of the fundamental physical constants: 2018”. In: *Rev. Mod. Phys.* 93 (2 2021), p. 025010. doi: 10.1103/RevModPhys.93.025010. url: https://link.aps.org/doi/10.1103/RevModPhys.93.025010.

[74] Marek Trippenbach et al. “Coherence properties of an atom laser”. In: *Journal of Physics B: Atomic, Molecular and Optical Physics* 33.1 (1999), pp. 47–54. doi: 10.1088/0953-4075/33/1/305.

[75] P. J. Ungar et al. “Optical Molasses and Multilevel Atoms: Theory”. In: *Journal of the Optical Society of America B* 6.11 (Nov. 1, 1989), p. 2058. issn: 0740-3224, 1520-8540. doi: 10.1364/JOSAB.6.002058. url: https://www.osapublishing.org/abstract.cfm?URI=josab-6-11-2058 (visited on 07/08/2019).

[76] Robert S. Van Dyck, Paul B. Schwinberg, and Hans G. Dehmelt. “Electron magnetic moment from geonium spectra: Early experiments and background concepts”. In: *Phys. Rev. D* 34 (3 1986), pp. 722–736. DOI: `10.1103/PhysRevD.34.722`. URL: `https://link.aps.org/doi/10.1103/PhysRevD.34.722`.

[77] Robert S. Van Dyck, Paul B. Schwinberg, and Hans G. Dehmelt. “New high-precision comparison of electron and positron g factors”. In: *Phys. Rev. Lett.* 59 (1 1987), pp. 26–29. DOI: `10.1103/PhysRevLett.59.26`. URL: `https://link.aps.org/doi/10.1103/PhysRevLett.59.26`.

[78] Ming-Sheng Zhan et al. “ZAIGA: Zhaoshan long-baseline atom interferometer gravitation antenna”. In: *International Journal of Modern Physics D* 29.04 (2020), p. 1940005. DOI: `10.1142/S0218271819400054`. eprint: `https://doi.org/10.1142/S0218271819400054`. URL: `https://doi.org/10.1142/S0218271819400054`.

[79] Y.-Q. Zou et al. “Magnetic Dipolar Interaction between Hyperfine Clock States in a Planar Alkali Bose Gas”. In: *Physical Review Letters* 125.23 (2020), p. 233604. DOI: `10.1103/physrevlett.125.233604`.